Aggregation of alpha-synuclein using single-molecule spectroscopy

A dissertation by

Marija Iljina

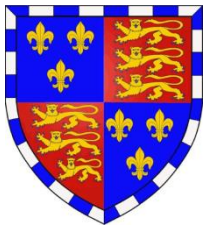

Submitted to the University of Cambridge for the degree of Doctor of Philosophy

Major-Subject: Chemistry

Christ's College

September 2016

Declaration

This dissertation summarises research carried out in the laboratory of Professor David Klenerman at the Department of Chemistry, University of Cambridge, between October 2012 and September 2016. This dissertation is the result of my own work. When work was performed in collaboration with others, it has been explicitly stated in the text. Any reagents, analysis tools developed by others, and results are specified in the relevant chapters and methods sections. This thesis is not substantially the same as any that I have submitted for a degree or diploma, or any other qualification at any other University. I further state that no substantial part of my dissertation is being concurrently submitted for any such degree, diploma or other qualification at the University of Cambridge or any other University of similar institution. The length of this dissertation does not exceed the prescribed word limit of the Physics and Chemistry Degree Committee (60,000 words).

Marija Iljina

September 2016

.

Acknowledgements

My time at the University of Cambridge has been an exciting and enjoyable experience, and I am grateful to my supervisor Prof. D. Klenerman for his valuable advice and support throughout my work. I wish to thank Dr. M. Horrocks and Dr. L. Tosatto for their preceding work on the single-molecule aggregation of alpha-synuclein, and their dedication and patience when introducing me to this research. I am grateful to the collaborators at University College London for their enthusiasm and their work on cell assays using alpha-synuclein, particularly Dr. M. Choi and Dr. S. Gandhi. I am also grateful to the members of Prof. T. Knowles group, especially to Dr. G. Garcia for the analysis of alpha-synuclein aggregation datasets, and to A. Dear for the analysis of co-oligomer results. I would like to acknowledge Christ's College for providing me with Dr. Tayyeb Hussain Studentship. Finally, I would like to thank all past and present members of our research group for creating a friendly working environment.

Summary

The aggregation of alpha-synuclein (αS) protein from soluble monomer into solid amyloid fibrils in the brain is associated with a range of devastating neurodegenerative disorders such as Parkinson's disease. Soluble oligomers formed during the aggregation process are highly neurotoxic and are thought to play a key role in the onset and spreading of disease. Despite their importance, these species are difficult to study by conventional experimental approaches owing to their transient nature, heterogeneity, low abundance and a remarkable sensitivity of the oligomerisation process to the chosen experimental conditions. In this thesis, well-established single-molecule techniques have been utilised to study the aggregation and oligomerisation of αS in solution, at a broad range of starting conditions.

Initially, the aggregation of αS has been studied by single-molecule techniques over a two orders of magnitude concentration range to develop an explicit kinetic model of its aggregation. The proposed kinetic model could fit the experimental data of the full concentration range and revealed that the aggregation mechanism was governed by two major unimolecular structural conversion steps, from disordered to ordered oligomers and then to fibrils, which could elongate by further monomer addition. The complete set of the rate constants of these key microscopic steps enabled making quantitative predictions of the number of αS aggregates that would be formed at varying pre-defined conditions such as low concentrations and small volumes mimicking the size of cells, conditions that are very difficult to access experimentally. This analysis showed that templated seeding of monomeric αS required a remarkably large number of aggregates in the order of 10^4 species, suggesting that spreading of αS is unlikely to occur solely by the process of templated seeding, and may be driven by aggregate-induced cellular stress.

Subsequently, the effect of two antibodies (nanobodies) that target C-terminal region of αS on its aggregation pathway was investigated. One common approach to therapeutic intervention in protein misfolding diseases such as Parkinson's disease is focused on suppressing its aggregation by antibodies that bind to αS and slow down or prevent its fibril formation. Despite the therapeutic potential of αS-specific antibodies, a detailed molecular-level understanding of their action during the aggregation process is lacking, especially on its earliest steps that are difficult to monitor by more conventional techniques. To investigate these effects in more detail, using single-molecule measurements, the aggregation of αS was studied in the presence of two nanobodies. The results revealed that both nanobodies exerted a highly specific effect during the earliest steps of the aggregation process, and invoked a conformational conversion from more ordered to less ordered

oligomers of αS formed prior to fibril formation, setting a stage for further assessment of potential therapeutic effect of these nanobodies.

While αS self-assembles into toxic oligomers and fibrils in Parkinson's disease, it is also proposed that αS forms soluble alpha-helical multimers in healthy neurons. Therefore, alpha-helical multimers of αS in the presence of a fatty acid (arachidonic acid) were prepared *in vitro*. Using a series of single-molecule assays, their clear differences were demonstrated in comparison to the oligomers formed in the absence of the fatty acid. The data suggested that arachidonic acid-induced oligomers were alpha-helical, resistant to fibril formation, more prone to disaggregation, enzymatic digestion and degradation by proteasome compared to the oligomers formed in the absence of arachidonic acid. These multimers could be formed at physiologically-relevant concentrations, and pathological mutants of αS formed less multimers than wild-type αS. These species were hypothesised to have a protective role with respect to the generation of beta-sheet toxic structures during αS fibril formation.

Finally, apart from being associated with Parkinson's disease, αS forms solid intraneuronal inclusions in brains of about half of Alzheimer's disease patients, pointing towards its implication in this common neurodegenerative condition, along with the key players in its aetiology, amyloid-beta peptide and tau protein. Single molecule methods were used to study the oligomerisation of αS at physiologically-relevant sub-micromolar concentrations and to investigate its cross-interactions with these other proteins. The results revealed the formation of stable co-oligomeric species between αS and amyloid-beta or tau. The ease of their formation under varying starting concentrations implied that the co-oligomers could be a common type of aggregate under conditions where multiple proteins co-exist, highlighting the need for further investigation of the properties of these species and their role in the mechanism of protein aggregation.

Abbreviations

αS	Alpha-synuclein
AD	Alzheimer's disease
NAC	Non-amyloid component
β-sheet	Beta-sheet
IDP	Intrinsically disordered protein
PD	Parkinson's disease
LBs	Lewy bodies
LNs	Lewy neurites
PK	Proteinase-K
wt αS	Wild-type alpha-synuclein
sm-FRET	Single-molecule Förster resonance energy transfer
AF488 (594)	Alexa Fluor 488 (or 594)
DMSO	Dimethyl sulfoxide
TCCD	Two-colour coincidence detection
A90C	Alanine to cysteine mutation at residue 90
DTT	Dithiothreitol
APD	Avalanche photodiode
FPGA	Field programmable gate array
-mer	Monomer unit
TEM	Transmission electron microscopy
ThT	Thioflavin T
DLB	Dementia with Lewy bodies
MSA	Multiple system atrophy
Nbs	Nanobodies
TIRFM	Total internal reflection fluorescence microscopy

FA	Fatty acid
ARA	Arachidonic acid
CMC	Critical micellar concentration
CD	Circular dichroism
CSF	Cerebrospinal fluid
CAC	Critical aggregation concentration
Aβ	Amyloid-beta
APP	Amyloid precursor protein
PHFs	Paired helical filaments
std	Standard deviation
sem	Standard error of the mean

Contents

Chapter 1
Introduction

1.1 Alpha-synuclein protein

In this chapter, an overview of the properties of alpha-synuclein is presented, and the details of its structure, aggregation behaviour and its relation to Parkinson's disease.

1.1.1 Brief history of αS

Alpha-synuclein (αS) is a member of the family of synucleins, soluble proteins found in vertebrates, which also includes beta- and gamma-synucleins, and synoretin[1]. First synuclein was isolated 28 years ago from the electric fish *Torpedo californica* as a protein found in the nuclear envelope and presynaptic nerve terminals, and the name "synuclein" arose because of its localisation[2]. Human αS was identified several years later as a non-Aβ constituent of amyloid plaques in brains of patients with Alzheimer's disease (AD)[3]. Further research revealed that this protein was 95.3% identical in terms of its structure to αS found in rodents, similar to αS from *Serinus canaria* bird, and homologous to the *Torpedo* protein, which is currently classed as gamma-synuclein[4].

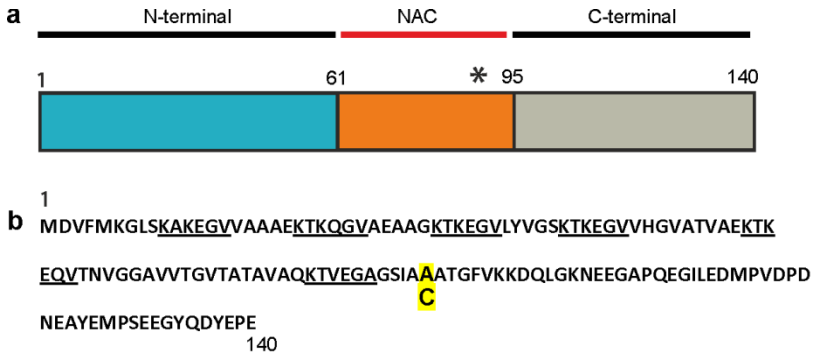

Figure 1.1. a. Cartoon representation of the primary sequence of full-length αS. Three domains can be distinguished: N-terminal domain comprising first 60 residues, non-amyloid component (NAC) region consisting of residues 61-95, and C-terminal region comprising the rest of the molecule. NAC region forms the core of fibrillar structures. Residue 90 (black star) at the periphery of NAC region has been used for the covalent attachment of fluorescent probes in this study. **b.** Primary sequence of aminoacids of αS. The hexameric repeating motif is underlined, and the position 90 with a substitution from alanine to cysteine is highlighted in yellow. (Figure adapted from Deleersnijder, 2013)[5].

1.1.2 Three regions of the primary sequence of αS

αS is a relatively small protein with a molecular weight of 14.5 kDa and 140 amino acids (Fig. 1.1)[6]. Its primary sequence consists of three distinct regions[7]:

- a positively charged N-terminal segment (residues 1-60)
- a central region known as the non-amyloid component (NAC) (residues 61-95)
- and a negatively charged acidic C-terminal region (residues 96-140).

Specific properties of each of these regions determine the behaviour of the protein, its secondary and tertiary structure and aggregation propensity, as well as its interactions with possible partners, as discussed below.

1.1.2.1 N-terminal

The N-terminal segment contains four full 11-residue imperfect repeats with a conserved hexameric motif (KTKEGV), which resemble the alpha-helical lipid-binding domains of exchangeable apolipoproteins[8]. The alpha-helixes formed by these repeats precisely match the class A2 helix motif of apolipoproteins[9]. Since apolipoproteins are known to reversibly bind to surfaces of lipid membranes, this similarity suggests that αS might also have this capability, and that the N-terminal region might be specifically responsible for this binding[10]. Indeed, multiple studies confirm this, showing that αS binds to lipid membranes[11-14], and this can happen via its N-terminal region which adopts an alpha-helical structure upon binding[10,15]. Interestingly, pathological αS mutations, A30P, E46K, A53T,[16] H50Q[17] and G51D[18] are all found in the N-terminal segment, which emphasises the importance of its modifications to αS behaviour. It was shown that truncation of this region promoted αS fibril formation, presumably by increasing the overall hydrophobicity of the protein, and addition of extra 11-residue repeats suppressed it[19]. Also, increasing the number of negative charges in this region was shown to slow down αS fibrillation, whereas increasing the positive charge resulted in acceleration of the process, demonstrating the importance of the net charge in this region[20].

1.1.2.2 NAC region

The central hydrophobic NAC region is responsible for the aggregation of αS and the formation of beta (β)-sheet structures[21]. Multiple structural studies of αS fibrils show that they are comprised of separate entangled protofilaments, which in turn consist of multiply-stranded ordered cross-β-sheets, involving the central NAC region of αS and leaving residues 1-30 and 110-140 mobile and unstructured[22-26]. Therefore, the NAC region is the key constituent of αS fibrils, and alterations to its

structure influence fibril formation. For example, deletion of a 12-residue fragment of aminoacids 71-82 in the middle of this region stops αS fibrillation[27], which is consistent with the fact that incapable of fibrillation β-synuclein naturally lacks residues 71-82. Deletion of a shorter sequence, residues 66-74, leads to the same result[28]. Even more convincing in demonstrating the role of the NAC region in αS fibrillation are alterations to single residues. Koo *et. al*. showed that more than 20 single amino acid substitutions block fibril formation, even during prolonged incubation[20]. In the same study, the overall hydrophobicity of the NAC region was also demonstrated to be important for fibril formation. From the substitution studies, particularly efficient were mutants with substitutions at positions 66-75 of NAC, and were even found to exhibit inhibitory effect on non-mutated αS[29].

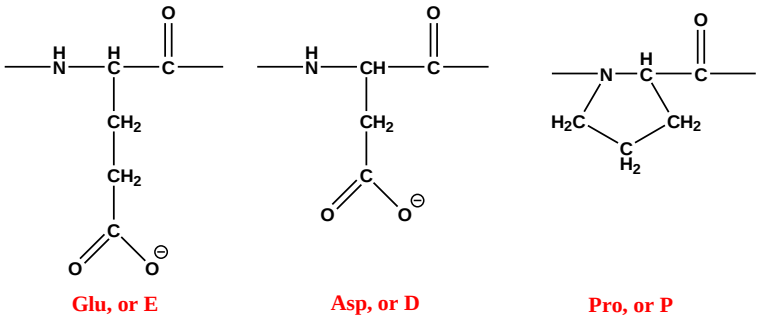

Figure 1.2. C-terminal of αS is acidic and negatively charged due to the presence of 10 glutamic acid (Glu, or E) residues and 5 aspartic acid (Asp, or D) residues. It is the only region in αS molecule containing prolines (Pro, or P), which are known to disrupt secondary structure due to their conformational rigidity.

1.1.2.3 C-terminal

The C-terminal of αS contains 10 Glu and 5 Asp residues (Fig. 1.2), which are negatively charged and acidic. Due to the high charge density, this region is responsible for the relatively high thermal stability of αS[30]. Although not a constituent of fibrils, it regulates αS aggregation by shielding the hydrophobic and non-polar NAC region from water-based solvent[31], and is important in stabilising the formed fibrils[32]. The region is the only segment containing proline residues, which are well-known secondary structure breakers, and thus help to disrupt an aggregation-prone conformation[33]. Therefore, the deletion of this region enhances fibril formation[34]. Due to its high charge and hydrophobicity, C-terminal of αS is responsible for the intrinsic disorder of the entire protein molecule, meaning the absence of an organised secondary structure under physiological conditions[35,36], which makes it a member of a class of intrinsically disordered (or unstructured) proteins (IDPs)[37]. Table 1.1 summarises the properties of αS and its structural domains. The presented data, cited from Uversky, 2000[38], was originally collected from the Swiss Institute of Bioinformatics.

The hydrophobicity was obtained by them from the Kyte and Doolittle approximation[38], and the mean hydrophobicity was defined as the sum of normalised hydrophobicities of all residues divided by the total number of residues. The charge here is the net charge at pH 7.0, divided by the total number of residues.

Table 1.1. A summary of the characteristics of αS and its structural domains.

Protein part	No residues	MW (Da)	Net Charge (Q)	Total hydrophobicity	Mean hydrophobicity
αS full chain	140	14,460	-10	61.761	0.4541
αS N-terminal	96	9,519.9	+4	46.893	0.5097
αS C-terminal	44	4,958.3	-13	13.471	0.3368

1.1.3 αS tissue expression and function

αS is highly expressed in brain and constitutes up to 1% of proteins in neuronal cytosol[39]. Although the first studies of synuclein in *Torpedo fish* reported its localisation to the nuclear envelope[2], research in rat and human brain suggests its location mainly in cytosolic fraction of neurons[40] and in mitochondria[41]. In human brain, αS is abundant in the substantia nigra, thalamus, amygdala, caudate nucleus, hippocampus, neocortex and other brain regions[4,42]. It is known to be specifically localised to presynaptic nerve terminals, in close proximity to synaptic vesicles, and for this reason is frequently referred to as 'presynaptic protein'[43,44]. Interestingly, structural aspects of αS behaviour under physiological conditions remain elusive[5]. For example, it is uncertain whether monomeric αS exists in an IDP form[35], or as a helically folded tetramer[45]; or which portion of it exists in a helical form within cells due to lipid binding[5]. Moreover, the exact physiological role of this protein is still poorly understood[46]. It has been proposed to be involved in storage, transmission and biosynthesis of vesicular dopamine[47], trafficking[39] and stabilisation of synaptic vesicles[48], to act as a cellular ferrireductase[49], to play a role in mitochondrial function[41] and neuronal protection[50]. This, clearly, is a small part of a comprehensive list of possible physiological functions of αS, especially considering the fact that it was identified as an interaction partner with over 50 other proteins[51]. Despite this lack of clarity of αS physiological structure and precise function, it was reported that mice lacking the protein displayed altered neurotransmission[52] and decreased overall levels of dopamine[53]; and mice lacking all synucleins died prematurely[54]. This, therefore, suggests the importance of the presence of this protein in a healthy brain.

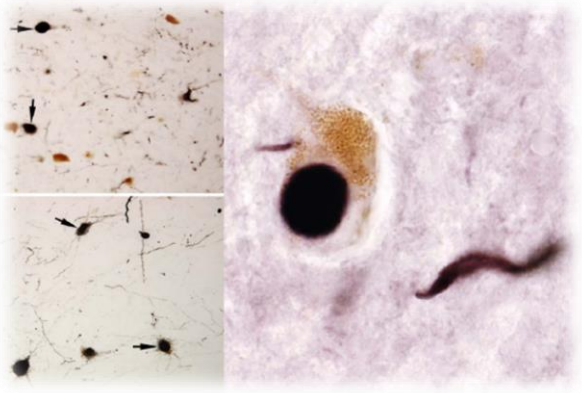

Figure 1.3. Pathological αS inclusions, Lewy bodies and neurites, in dopamine neurons in substantia nigra (top-left), striatum (bottom-left) and mesenchephalic nucleus of trigeminal nerve (right). Although stained for αS in the images, these inclusions are known to contain various other proteins such as tau, ubiquitin and alpha-crystallin. (From Olanow, 2013)[55].

1.1.4 αS relation to Parkinson's disease

Parkinson's disease (PD) was first described by an English doctor James Parkinson in 1817, in his *Essay on the Shaking Palsy*[56]. It currently affects more than 1% of the population over 60 years of age, around 4% over 80[57], and the age group of 20-50 years (in 5-10% of all cases)[58]. According to approximate estimations, around 1.2 million people in Europe suffer from PD, and over 7 million worldwide[57], which makes it the second most common human neurodegenerative disorder after AD[59].

PD symptoms include resting tremor in limbs, bradykinesia or slowness of movement, muscular rigidity, postular instability and festination, as well as disturbances of mood, speech, memory and cognition[60]. These arise from a progressive loss of dopaminergic neurons in the substantia nigra and other brain regions, and are accompanied by the deposition of Lewy bodies (LBs) and Lewy neurites (LNs), solid intracellular inclusions in surviving neurons[61,62] (Fig. 1.3). These inclusions are named after Friederich Heinrich Lewy, who first identified them in the brain tissue from PD patients[63]. The lesions are termed either 'bodies' or 'neurites' depending on whether they are located in the neuronal cell bodies, or in axons or dendrites, and also tend to differ in shape, but in all cases contain aggregated αS as the main consituent[64], along with various other molecules such as molecular chaperones, lipids and components of protein degradation systems[65,66]. Interestingly, more than 90% of αS present in these inclusions is phosphorylated at serine-129, which accelerates fibril formation of αS[67], and bears numerous other modifications, among which are truncations, nitrosylation and ubiquitination[68].

The fact that LBs are composed predominantly of αS filaments was shown in 1997 by Spillantini *et. al*.[64], providing strong evidence for the importance of this protein to the disease etiology. Other supporting arguments are the notion that point mutations in SNCA gene coding for αS were found in the families with hereditary PD, and locus duplications and triplications of this gene led to early onset PD[69]. In addition, artificially overexpressing αS in mice[70], flies[71], and primates[72] resulted in animals exhibiting age-dependent motor disfunction and formation of αS deposits resembling LBs, which demonstrated that an increase in αS concentration in brain can be sufficient to cause PD symptoms. It was proposed that neurons containing LBs had a shorter life span compared to healthy neurons[73]. Following the notion that αS is harmful to neuronal cells and causes neurodegeneration, attempts to treat PD patients by reducing αS *in vivo* were made, leading to unexpected results. PD was shown to develop more rapidly, with worse motor and cognitive symptoms, in individuals with lowered production of αS, highlighting the complexity and general lack of understanding of αS role in the disease progression[74].

1.1.5 Oligomers are believed to be the most toxic forms of αS

Even though LBs consisting of αS fibrils are the pathological hallmarks of PD, increasing evidence suggests that oligomers and pre-fibrillar protofilaments, rather than fibrils, are the most cytotoxic and damaging species[75,76-79]. The A30P mutation, linked to early-onset PD, was shown to accelerate oligomerisation and inhibit the conversion of protofibrils to fibrils[76]. *In vitro* studies demonstrated that dopamine-αS complex formation caused the accumulation of pre-fibrillar species[80]. It was noticed that in PD transgenic mice models, disease-related symptoms often appeared prior to detection of fibrillar αS[70]. Moreover, αS oligomer toxicity was compared with αS fibril toxicity *in vivo*, in substantia nigra of rats, and the most severe loss of neurons was observed due to αS oligomers[81]. To confirm oligomer cytotoxicity, oligomer pathology has been directly visualized in PD human brain tissue. Using a proximity ligation assay, oligomers of αS were observed in the absence of LBs, displaying intermediate proteinase-K (PK) resistance between monomers and fibrils[82].

Owing to the established high cytotoxicity of αS oligomers, there have been numerous *in vitro* studies aiming to isolate and characterise these species. Multiple protocols for the generation of oligomeric species have been reported, including spontaneous self-assembly in aqueous buffer during fibril formation[79,83], using lyophilisation[84] (Fig. 1.4.), preparation via fibril disaggregation[79] and cold-induced fibril dissociation[85] or oligomer formation induced by the addition of small molecules such as dopamine and gluteraldehyde[86], that yield different types of oligomeric species. A variety of αS oligomer morphologies have been reported such as, for example, spherical and elongated[87], tubular

and ring-shaped[88] structures, oligomers with a solid core[89] or containing an inner cavity[84]. Furthermore, due to the large variation in the reported types of oligomers of αS, their functional role during αS aggregation reaction was found to vary, and off-pathway stable oligomers incapable of seeding were reported[84,89] as well as stable oligomers capable of seeding[86]. Two distinct structural types of αS oligomers have been identified in two independent studies, disordered globular oligomers, and more compact fibril-like oligomers[79,90]. The second, more ordered type has been demonstrated to be more toxic than the first type, when applied on rat primary neurons[79], which is in good agreement with earlier reports that ordered prefibrillar oligomers may be the key inducers of cytotoxicity[78]. In an earlier study, the two types of oligomers were proposed to be sequential intermediates on the pathway to fibril formation[79], while in a later study[90], the more compact oligomers were proposed to be off-pathway species.

Despite the large variation in the reported types of αS oligomers and their different roles in the aggregation process, the stable oligomers of αS are generally characterised by β-sheet content that is intermediate between monomers and mature fibrils[79,91], hydrophobicity that is higher than of monomers or fibrils[92,93], and are composed of approximately 25-30 monomer units[84,89,94].

Multiple mechanisms have been suggested to underlie the cytotoxicity of αS oligomers, such as their interactions with lipid membranes leading to the membrane disruption and pore formation; the sequestration of intracellular components such as parts of cytoskeleton, transcription factors or components of degradation system; the induction of oxidative stress that results in lipid peroxidation; the direct interaction of oligomers with cellular receptors resulting in cell apoptosis (reviewed in Andreasen et. al. 2015[91]).

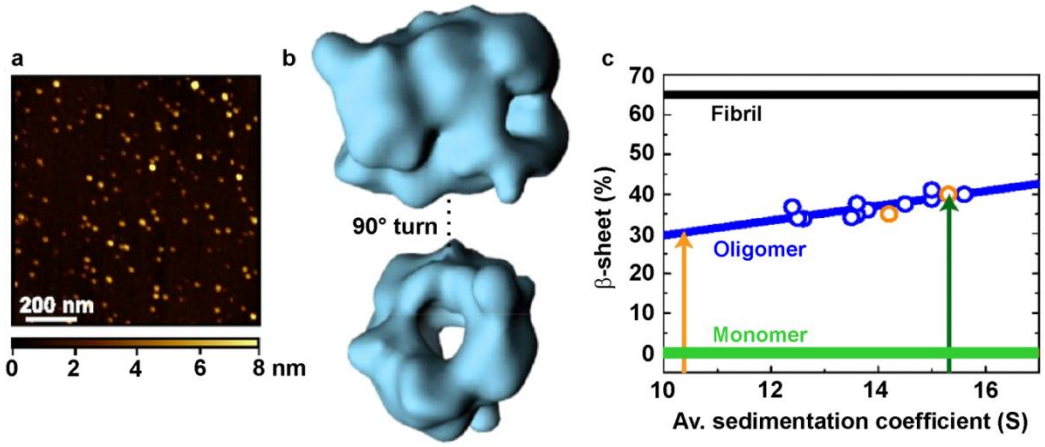

Figure 1.4. Characterisation of stable αS oligomers prepared *in vitro* by using lyophilisation protocols. **a.** Representative AFM image of isolated oligomeric sample. **b.** 3-dimensional reconstruction of an average αS oligomer from cryo-EM imaging, depicting a characteristic central cavity. **c.** Analysis of oligomer structural contents using analytical ultracentrifugation. The results suggest the gradual acquisition of β-sheet conformation during oligomer growth. (From Chen *et.al.*, 2015[84]).

1.1.6 αS aggregation

The aggregation of αS is implicated in PD and PD-related disorders, such as LB variant of AD, dementia with LBs (DLB), multiple system atrophy (MSA), Hallervorden-Spatz disease, Down's syndrome, and infantile neuroaxional dystrophy[95-97].

Generally, it has been shown that fibrillisation of wild-type (wt) αS is relatively inefficient and requires high protein concentrations and long timescales ranging from days to weeks[98], unless inducers are used to increase the rate of the process. For example, acceleration of αS aggregation can be achieved using various anionic detergents, polyamines, lipids or acidic pH[11]. αS is known to bind several metal cations, including Fe^{2+}, Al^{3+}, Zn^{2+}, Cu^{2+}, and Ca^{2+},[30] and the binding of Cu^{2+},[99] and Ca^{2+} [100] was shown to influence the aggregation of αS by promoting oligomer formation *in vitro*. Additionally, mechanical agitation such as continuous shaking or stirring can be used to promote the fibrillisation process[98,101,102]. It is well-established that the aggregation of αS can be initiated by protein misfolding. Uversky *et. al*. identified a reversible structural change in αS monomer at the conditions of either low pH or high temperatures. It was proposed to be an early-stage 'aggregation-prone' intermediate on the path towards fibril formation, because the conformational change matched the onset of fibril detection[102]. The intermediate was monomeric and less compact than a globular structure, hence termed 'partially-unfolded'. It was shown to have β-sheet character, with the same structural characteristics at conditions of either low pH or elevated temperature. Authors explained the temperature-induced formation of the intermediate by an increase in hydrophobic interactions, and the pH-induced formation due to the decrease in the negative charge in the C-terminal region via the protonation of carbonyls. They proposed that any factors shifting the equilibrium towards the folded monomer state will promote fibril formation. In addition to low pH, high temperature and non-polar molecules were suggested.

αS aggregation is known to be a nucleation-polymerization process[103], characterised by a sigmoidal reaction profile (Fig. 1.5). There is an initial lag phase, when oligomeric nuclei are formed, followed by an exponential growth phase, where nuclei grow through monomer addition while forming protofilaments and fibrils. The process ends with the steady-state phase, when equilibrium between αS soluble forms and fibrils is reached. There exists a limiting concentration for this process, termed "the critical aggregation concentration" (CAC), below which the protein is thermodynamically stable in its unfolded form, and above which it tends to lower its free energy through fibrillisation. The values reported for αS vary, but tend to be in the low-micromolar range[104,105]. The sigmoidal profile, however, does not represent a full picture of a multitude of microscopic processes occurring during αS aggregation. For example, it was realised that fibril growth can be largely influenced by secondary nucleation events like fibril fragmentation[106]. Cremades *et. al.* identified a slow structural

interconversion between oligomers during the initial stages of αS aggregation using single-molecule techniques[79]. It was determined to be of the order of half-life of *in vivo* αS turnover.

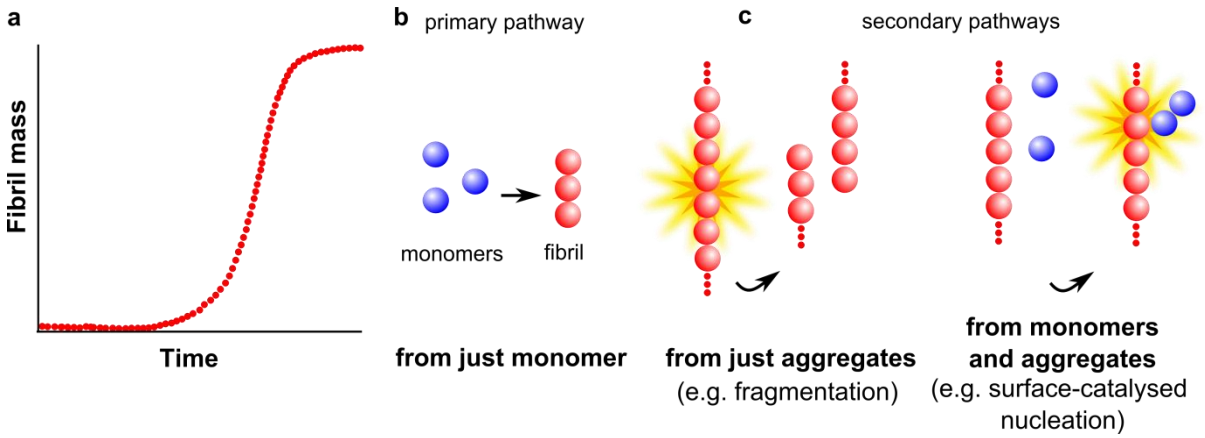

Figure 1.5. Typical aggregation kinetics and underlying microscopic reactions. **a.** The aggregation reaction of αS is commonly described by the sigmoidal kinetic profile. The microscopic mechanisms that lead to the production of aggregates during the aggregation process can be separated into primary nucleation, when aggregates are generated solely from monomeric units (**b.**) and secondary nucleation reactions (**c.**), involving the production of new aggregates from the existing aggregates, or from both monomers and the existing aggregates. (From Cohen *et. al*., 2012[107]).

1.2 Single-molecule methods

1.2.1 Principles of single-molecule FRET experiments

It has been discussed above that oligomers of αS are commonly considered to be the most cytotoxic species in PD. During αS aggregation, however, they constitute a low fraction of the total protein concentration and are present in a vast excess of monomer, are transient and highly heterogeneous. Therefore, it is difficult to characterise them by bulk techniques, which depict average features of an ensemble. Single-molecule techniques are more useful in this case, because they enable detecting individual species[108]. Single-molecule confocal microscopy methods have been developed and used by the Klenerman group to study the oligomer formation during the aggregation reactions of a number of amyloidogenic proteins such as the SH3 domain from bovine phosphatidylinositiol-3'-kinase (PI3-SH3)[109], of αS[79] and Aβ[110]. These techniques were also utilised to studying the interactions of the oligomeric species with molecular chaperones[110] or cell membranes[111].

In this work, single-molecule FRET (sm-FRET) experiments have been performed on fluorescently labelled αS molecules in order to investigate early stages of the aggregation of this protein. FRET, which stands for Förster resonance energy transfer (or fluorescence resonance energy transfer), is an intermolecular non-radiative transfer of energy from an excited donor fluorophore to an acceptor fluorophore, with the efficiency given by[112]:

$$E = \frac{R_0^6}{R_0^6 + R^6} \tag{1.1}$$

where R is the donor-acceptor separation, and R_o is the distance at which 50% energy transfer occurs, and is dependent on the relative orientation of the fluorophores and their spectral overlap.

The dependence on donor-acceptor separation is advantageous for the structural characterisation of biomolecules and monitoring their conformational changes[113]. When applied to αS aggregation studies, sm-FRET technique has demonstrated the ability to discriminate between oligomers of distinct structural types, follow their formation, size distribution, conformational conversion and stability[79].

In the sm-FRET experiments carried out in this thesis, custom-built single-molecule confocal setup was implemented, that is described in more detail in Chapter 2, section 2.6. The setup enables the detection of fluorescence emission from individual fluorescently-labelled protein monomers and oligomeric aggregates as they travel through the laser excitation region. This technique allows the detection and individual characterisation of large numbers of oligomeric aggregates present in aqueous solutions without the need to physically separate these species from monomeric protein. This is achieved by analysing an equimolar mixture of fluorescently labelled protein solutions during the aggregation reaction. In a typical αS aggregation experiment, a 1:1 stoichiometric ratio of Alexa Fluor 488 (AF488) and Alexa Fluor 594 (AF594) labelled αS is combined and incubated with agitation in order to induce its aggregation (Fig. 1.6a). Aliquots are withdrawn from the mixture at defined time-intervals. Upon withdrawal, the solutions are immediately diluted for single-molecule analysis, and continuously passed through a microfluidic channel that allows to reduce the sampling time[114,115]. A 488 nm laser beam is focussed into the centre of the channel, to excite the AF488 dye directly, and the emitted fluorescence is simultaneously collected in both AF488 (donor) and AF594 (acceptor) channels (Fig. 1.6b). AF594-labelled monomers passing through the confocal volume are undetectable, whereas AF488-labelled monomers give rise to single bursts in the donor channel, enabling the level of monomeric αS to be monitored during the aggregation reaction. As oligomers typically contain both types of labels, they are detected as simultaneous intense bursts in the donor and the acceptor channels, due to the emission from both the directly excited AF488 and from the non-radiatively excited AF594 via FRET (Fig. 1.6c). In this manner, oligomers can be distinguished from monomers despite the fact that the latter are found at much higher concentrations; and the

oligomer numbers and fractions in solution can be quantified as a function of the reaction time. In addition, the fluorescence intensities recorded in both donor and acceptor channels for each oligomer can provide information on the structural characteristics of the detected oligomers. More detailed experimental procedures and analysis protocols for sm-FRET experiments are presented in Chapter 2, sections 2.4.-2.8., and the results of these experiments are shown and discussed in Chapters 3-5.

1.2.2 Principles of single-molecule TCCD experiments

Two-colour coincidence detection (TCCD) can be performed utilising the same experimental setup as the one used for sm-FRET experiments. In contrast to sm-FRET, where irradiation only by 488 nm laser beam is used, TCCD involves dual excitation by a pair of overlapped laser beams, operating at 488 nm and 594 nm, or at 488 nm and 633 nm, depending on the AF label pairs of the analysed protein samples. In TCCD experiments, in contrast to monitoring FRET signal between the dye pairs, direct fluorescence emission from both AF488 and AF594 (or AF647) is detected as a consequence of direct dual-colour laser excitation. Singly labelled protein monomers will give rise to non-coincident fluorescence bursts, whereas oligomeric aggregates bearing two different fluorophores are expected to produce two fluorescence bursts that are coincident in the two emission channels, and can therefore be distinguished from the non-coincident monomeric bursts, as is illustrated in Fig. 1.6d. The procedures that were used to carry out these experiments are detailed in the next chapter, General methods, in sections 2.11-2.12. To note, this approach is not restricted to the analysis of aggregates that are sufficiently compact in order to exhibit detectable emission due to FRET. Therefore, TCCD technique has been applied in this thesis for the measurements of aggregates that were not necessarily expected to exhibit high degree of compactness, such as co-oligomers formed as a result of the direct interaction of αS with other aggregation-prone proteins, described in Chapter 6.

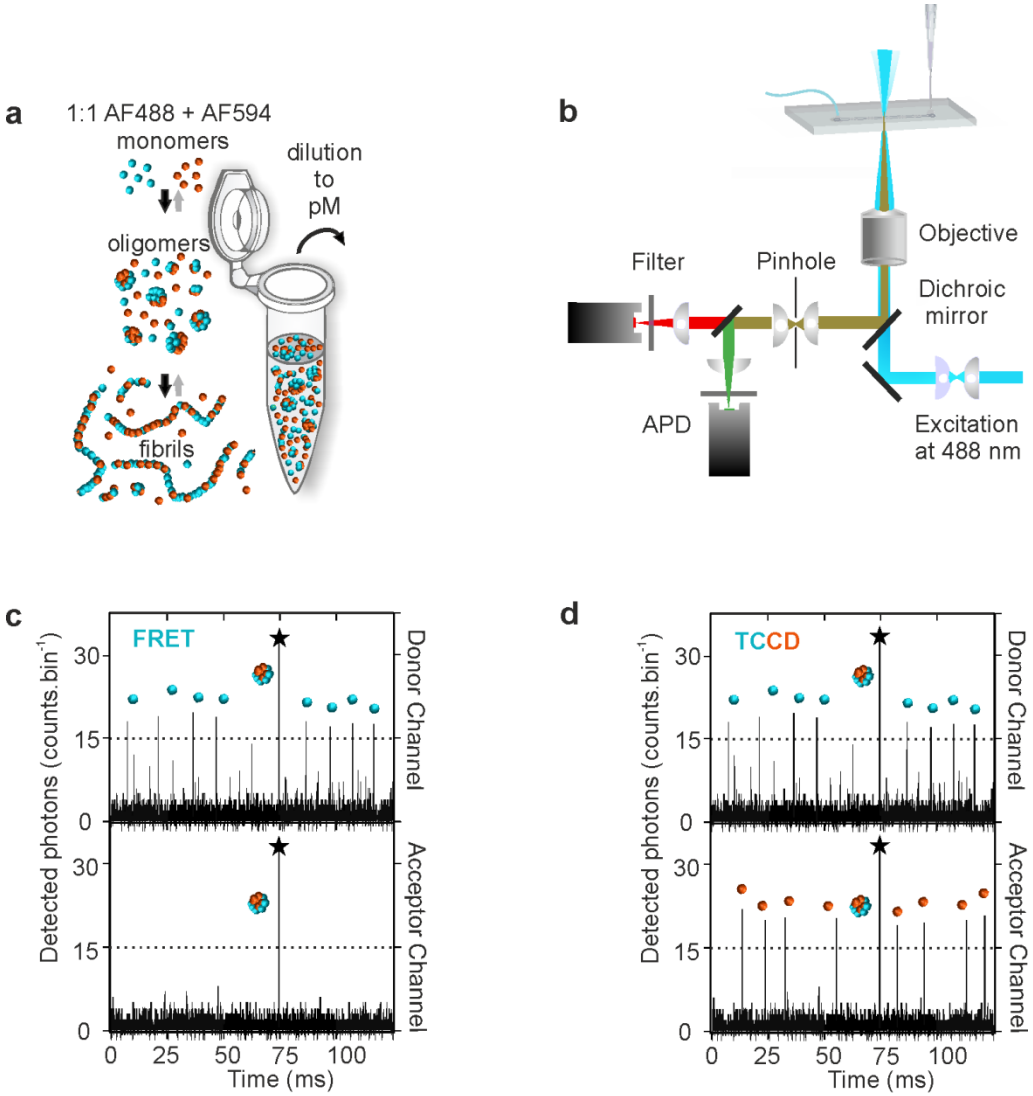

Figure 1.6. Schematic representation of sm-FRET and TCCD experiments. **a.** 1:1 stoichiometric ratio of αS monomer labelled with AF488 and AF594, shown as blue and orange spheres, was combined at a chosen initial concentration and allowed to aggregate. During the process, the monomeric protein assembles into oligomers, the main focus of the present thesis, and then amyloid fibrils. Aliquots were withdrawn, diluted and analysed using a custom-built single-molecule microscope. **b.** Schematic of the setup used for the sm-FRET experiments, with one colour laser excitation and two-colour detection. On the top of the confocal microscope objective, a microfluidic device is placed, and a protein sample flown through its channel at a constant rate. **c.** Representative sm-FRET fluorescence intensity traces, when 488-nm excitation is used. Non-coincident bursts in the donor channel arise from the AF488-labelled protein monomers (represented as blue spheres), and monomers are typically present in excess, while the AF594-labelled monomers (orange spheres) are not detected. The coincident intensity burst, marked with black stars in both channels, corresponds to the oligomer. **d.** Representative TCCD fluorescence intensity traces, when simultaneous 488- and 594-nm laser excitation is used. Non-coincident bursts in both channels arise from either AF488- or AF594-labelled monomers, present in excess. The coincident intensity burst, again marked with a black star, denotes an oligomer.

1.3 Aims and structure of this thesis

The aim of this thesis is to apply the described single-molecule techniques, sm-FRET and TCCD, to study the aggregation of αS protein in solution at a range of starting conditions. As it has already been discussed, these methods allow the detection and characterisation of individual molecules and aggregates of αS, and enable to follow the earliest steps of its self-assembly that cannot be resolved using more conventional bulk experimental approaches.

The main objectives of the presented research are:

1. To study the aggregation of αS at a broad range of starting concentrations by sm-FRET in order to obtain quantitative kinetic profiles of oligomer formation and monomer depletion.

2. To illustrate how the resulting dataset can be applied in order to develop an explicit kinetic model of αS aggregation and enable extracting reaction orders of individual microscopic steps of this mechanism. Furthermore, to illustrate how the obtained parameters can be used to making predictions of the aggregation and seeding behaviour of αS at physiologically-relevant conditions that are not readily accessible experimentally. Moreover, to put forward a potential mechanism of αS spreading in cellular environment.

3. To investigate the influence of two αS-specific antibodies on its aggregation pathway, particularly on the early stages of this process comprising the formation and conformational conversion of oligomeric species.

4. To study the oligomerisation of αS in the presence of a biologically-relevant aggregation inducer, a fatty acid, and to compare and contrast the resulting oligomers to the oligomers formed by αS in aqueous buffer in the absence of the fatty acid.

5. To investigate the co-oligomerisation of αS with two other major proteins implicated in neurodegenerative diseases, amyloid-beta and tau, by performing their co-incubations at low physiologically-relevant concentrations.

The order of the subsequent chapters in this thesis is the following:

Chapter 2 describes the general methods and data analysis strategies used to carry out the experimental work presented in this thesis.

In Chapter 3, the aggregation of αS is investigated by single-molecule techniques at a wide range of the starting protein concentrations. The experimental datasets are presented that enable the development of a detailed kinetic model of αS aggregation. The main outcomes of this kinetic analysis are discussed. Based on the data-driven predictions, a hypothetical mechanism of αS spreading in disease is proposed.

In Chapter 4, the aggregation of αS is studied in the presence of two specific antibodies, NbSyn2 and NbSyn87. Their influence on the formation and properties of αS oligomers is described.

Chapter 5 presents the experiments where a biologically-relevant fatty acid is used to induce the oligomerisation of αS. The resulting oligomers are compared to the oligomers formed by αS in the absence of the fatty acid.

In Chapter 6, oligomerisation of αS and related aggregation-prone proteins is investigated at low starting protein concentrations. The formation of co-oligomers composed of two different proteins is identified.

Chapters 3-6 of this thesis are organized in a stand-alone manner according to a common structure. Each chapter begins with a literature review to provide the background for the presented experimental work. The description of methods that are specific to the experiments in the chapter follows. Subsequently, detailed results of the experiments are presented along with their discussion. Finally, the main experimental findings and their interpretation are reviewed and summarised.

Chapter 2
General methods

2.1 Scope of this chapter

This chapter summarises the most commonly utilised experimental protocols and data analysis methods, routinely carried out for the projects described in this thesis. Additional experiments or analysis methods that are specific to the individual projects will be described in the Methods sections of the corresponding chapters.

2.2 αS expression and purification

Monomeric alanine to cysteine full-length mutant (A90C) or full length wild-type (wt) αS were expressed and purified either by Dr. Nadia Shivji, Beata Blaszczyk or Eva Klimont based on the protocol by Hoyer *et. al*.[116], and normally available as 300-400 µM aliquots stored at -80°C. A90C was stored with addition of dithiothreitol (DTT) to prevent cysteine oxidation and disulfide bridge formation.

2.3 αS labelling procedure

Labelling of A90C αS at the residue 90 of αS was achieved via a selective thiol-maleimide reaction, since position 90 is the only cysteine residue in the αS mutant. This labelling process occurs via Michael-type conjugate addition, forming a thioether as a final product, as shown in Fig. 2.1.

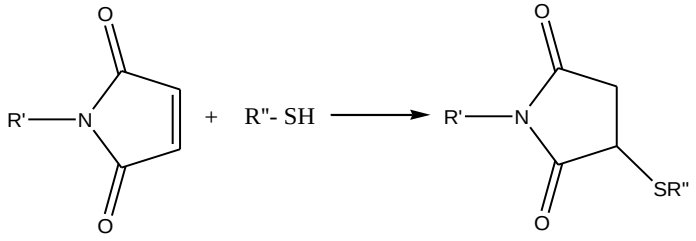

Figure 2.1. Reaction scheme for labelling of A90C αS. Maleimide and thiol react to form a thioether. R' represents the remaining part of AF488 or AF594 molecules; and R'' denotes 139 residues of αS.

PBS buffer (10 mM phosphate, 0.27 mM KCl and 137 mM NaCl, pH 7.4) was degassed by stirring under vacuum for 1 h. 1-2 ml aliquots of αS were eluted with the buffer through a PD10 desalting column containing Sepadex G25 matrix for DTT removal. Eluted fractions were combined and the overall concentration was determined by absorbance at 280 nm, using ε = 5,600 M^{-1} cm^{-1}. Subsequently, either AF488 solution in dimethyl sulfoxide (DMSO), or AF594, or AF647 (maleimide linkers, Invitrogen Lifesciences) solution in DMSO was added to the protein in a molar ratio 1:1.5 protein:dye. The solutions were stirred in dark at 4°C over a period of at least 3 h. Subsequently, each of the solutions was loaded onto a PD10 desalting column and eluted with Tris buffer (25 mM Tris, 100 mM NaCl,pH 7.4), to remove excess free dye. The labelled protein of each colour separately was concentrated by ultracentrifugation for 5 min at 4,000 rpm and 4°C, using centrifugal filter device with 10 kDa cutoff (Amicon). This resulted in protein of 100-200 µM, determined by absorbance at 495 nm and ε = 72,000 M^{-1} cm^{-1} for AF488-labelled portion, at 594 nm and ε = 96,000 M^{-1} cm^{-1} for AF594-labelled portion, and at ε = 265,000 M^{-1} cm^{-1} for AF647-labelled portion. The resulting samples were aliquoted into <100 µL portions, flash-frozen in liquid N_2 and stored at -80°C prior to single-molecule measurements. The reaction completion was confirmed by mass spectrometry. The peak at 14,492.2 amu due to the unlabelled A90C was negligible, whereas peaks at 15,192.2 amu for the case of AF488-labelled αS, at 15,379.2 amu for AF594-labelled αS, and at 15,477.2 amu for AF647-labelled αS were intense. Since it was found that the absorbance at 280 nm was strongly affected by the presence of AF fluorophores, the labelling efficiency could not be determined using absorbance and mass spectrometry was used. From the ratios of the intensities of the peaks corresponding to labelled and unlabelled protein, the labelling efficiency was typically >98% (see Appendix 1 for representative mass spectra).

2.4 Sample preparation for αS aggregation experiments

For sm-FRET aggregation experiments, the AF-labelled αS was singly used upon defrosting. A 1:1 molar ratio of AF488 and AF594-labelled monomeric αS were combined in Tris buffer (25 mM Tris, 0.1 M NaCl, 0.01% NaN_3, pH 7.4) up to a chosen starting protein concentration (0.5-140 µM, depending on the experiment) and a sample volume of 300 µL. The AF488 and AF594 dye pair was chosen as the least interfering fluorophore combination for αS fibril formation shown by the previous studies[115]. The solutions were incubated in the dark at 37°C with constant agitation at 200 rpm (New Brunswick Scientific Innova 43), and aliquots were withdrawn at regular intervals for sm-FRET experiments. The purity of the starting material was confirmed by sm-FRET measurements of the samples prior to the incubation, and only solutions devoid of pre-formed aggregates were used for time-dependent measurements.

2.5 Production of microfluidic devices

The microfluidic devices used for sm-FRET measurements of αS solutions were produced according to previously established protocol[114]. SU-8 2025 photoresist (MicroChem) was spin-coated onto a silicon wafer at 3,000 rpm for 30 s, and prebaked for 15 min at 95°C. Then it was exposed to UV light through a mask aligner with straight channels, and hard-baked at 95°C for 5 mins. A mixture of approximately 1:10 (w/w) ratio of curing agent (Sylgard 184, Dow Corning) to PDMS was poured over the master, degassed and baked at 65°C overnight. The procedure allowed devices with the channels of 25 µm height and 100 µm width. They were separated from the master, cut and punched using biopsy punches to introduce holes. Subsequently, the devices were exposed to oxygen plasma for 7 s, sealed to a microscope glass slide and baked at 65°C overnight.

2.6 sm-FRET data acquisition

Aliquots from the αS aggregation sample were diluted in a serial dilution up to 280 pM immediately prior to the measurement, using Tris buffer of the same composition as for the aggregations. The analysed solution was introduced into an inlet of a straight-channelled microfluidic device via a gel-loading tip, and passed through the channel at a constant rate of 2 cm s^{-1} via a syringe pump (PHD2000, Harvard Apparatus). The setup used for single-molecule measurements was analogous to previously described[115], and was built by Dr. M. Horrocks. It is schematically shown in Fig. 1.4b.

For sm-FRET measurements, a collimated 488 nm laser beam (Spectra Physics NewPort Cyan) was directed through a back port of an inverted microscope (Nikon Eclipse Ti-U) at 2 mW power (measured at the back port of the microscope), where it was reflected by a dichroic mirror (Semrock DiO1 R405/488/594) and sent through an oil immersion objective (Plan Apo VC 60 x, NA 1.40, Nikon) to be focused 10 µm into the centre of a microfluidic channel. Fluorescence signal was collected by the same objective, imaged onto a 100 µm pinhole (Thorlabs) and separated into two channels by a dichroic mirror (Horiba 585DRLP). The pinhole was conjugate with the plane of focus of the microscope objective and the point of the laser excitation, and thus eliminated out-of-focus fluorescence and scattered light, and reduced the background noise. Donor fluorescence was filtered by a long-pass (Edge Basic 514) and a band-pass filter (535AF45 Omega Filters) before being focused onto an avalanche photodiode, APD (Perkin Elmer). Acceptor fluorescence was directed through a long-pass filter (610ALP Horiba) and a band-pass filter (BrightLine 629/53) before being focused onto a second APD. Synchronous output from the APDs was collected by custom-implemented field-programmable gate array, FPGA (Celoxica RC10) (programmed by Dr. A.

Zhukov). Data were typically acquired for 400 s (80 frames, 100,000 bins per frame, 50 μs bin-width) per aliquot, and consisted of time-binned photon bursts in the donor and the acceptor channel. All measurements were made at ambient temperature around 20°C. The utilised experimental setup had an additional 633 nm laser line (Melles-Griot HeNe) and corresponding set of filters, allowing operation in the 488/633 nm mode in the cases where AF488 and AF647 dye pairs were used for the experiments.

2.7 Alignment of the instrument

Manual alignment of the single-molecule setup was routinely carried out to ensure that the detected fluorescence events were recorded coincidently and their intensities were maximised. Alignment involved the collimation and overlap of the two laser beams, 488 nm (Spectra Physics NewPort Cyan) and 594 nm (Cobolt Lasers), operating at the powers of 120 μW and 35-40 μW, respectively. The shapes and positions of the laser beams were adjusted manually by using sets of optical mirrors and projecting both beams onto a CCD camera. The beam overlap was initially inspected by projecting the adjusted laser beams onto a wall. To quantify the overlap, 25 pM dual-labelled (with AF488 and AF594) DNA sample was used (AtdBio), with the length of 40 base pairs, which makes it incapable of FRET. The sample was placed on a microscope coverslide, and irradiated by the overlapped laser beams. The fluorescence signal was detected in both channels simultaneously, and its intensity was maximised by manually adjusting positions of the pinhole and the APDs. The chosen laser powers enabled the detection of equal average fluorescence intensities in both channels, and were optimised by varying the laser powers in both channels. The data were collected with 1 ms bin times, 8,000 bins per frame, 80 frames and a total duration of 400 s. Subsequently, a custom-written "TCCD'' program (by Dr. Clarke) was used to analyse the collected results.

The program automatically determined the association quotient, given by[117]:

$$Q = \frac{(C-E)}{A+B-(C-E)} \tag{2.1}$$

where *A* and *B* are the event rates in the donor and acceptor channels, *C* is the rate of coincident events, *E* is the rate of chance coincident events. The program selected the fluorescence bursts in both channels above a defined threshold, corrected for the chance coincident events and outputted the Q. The instrument was considered suitable for the sm-FRET experiments once the value of 0.2 or more was obtained.

2.8 sm-FRET data analysis

Data were analysed using custom-written Igor Pro (Wavemetrics) code (written by Dr. M. Horrocks), according to a previously reported method[115]. Time-bins with intensities greater than 15 photons bin^{-1} in the donor (emission from AF488) and the acceptor (AF594) channel simultaneously (the AND criterion)[118] were assigned to be due to oligomeric events and selected for the analysis. The donor counts which did not fit the criterion but were above the applied threshold were saved separately and assigned as monomeric αS bursts. The threshold of 15 photons bin^{-1} for both channels was determined using the previously established optimised threshold selection method[117]. The values of the photon bursts were corrected for the cross-talk and the autofluorescence from the donor to acceptor channels according to $I_D = (D - A_D)$, where I_D is the modified intensity in the donor channel, D is the original intensity in the donor channel, A_D is the autofluorescence in the donor channel (1.6 photons bin^{-1}, corresponding to the average signal from buffer only), and $I_A = (A - A_A - C \times D)$, where I_A is the modified intensity in the acceptor channel, A is the original intensity in the acceptor channel, A_A is the autofluorescence in the acceptor channel (1.3 photons bin^{-1}), C is the cross-talk from donor to acceptor channel (13%). The crosstalk was negligible from the acceptor to donor channel. For every simultaneous oligomeric burst, the FRET efficiency was calculated:

$$E = \frac{I_A}{(I_A + \gamma I_D)} \tag{2.2}$$

where I_D is the donor intensity in the presence of an acceptor, I_A is the acceptor intensity and γ is the gamma factor specific to the instrument (0.99), which accounts for the relative detection efficiencies of the dyes and their quantum yield. The FRET efficiency values were binned into histograms with a bin width of 0.05. Subsequently, the data were split into two size groups: small oligomers consisting of 2-5 monomer units (-mers) and large oligomers (6-150-mers). Further details of the size estimation are included in section 2.10. Large aggregates, either occupying consecutive time-bins or greater than 150-mers, were excluded from the analysis as detailed in Horrocks *et. al.*[115].

2.9 Analysis of kinetic traces from sm-FRET experiments

The resulting FRET efficiency histograms were split into the two size groups based on the general difference in their appearance. At small sizes, one peak was observed in the FRET efficiency histograms in all measured samples. At large sizes, either one, or two FRET efficiency peaks could be distinguished, especially at the later stages of the aggregation reaction. Whenever the FRET efficiency

histograms showed two distinguishable distributions, separate kinetic traces for the two distributions were extracted. For this, the FRET histograms of the two separate size groups were globally fitted (eq. 2.3, Origin 7.0) to a single Gaussian distribution for 2-5-mers, or a double Gaussian distribution for 6-150-mers, using GaussAmp functions:

$$y = y_0 + A\exp\left(-\frac{(x-x_c)^2}{2w^2}\right)$$
$$y = y_0 + A\exp\left(-\frac{(x-x_c)^2}{2w^2}\right) + A_2\exp\left(-\frac{(x-x_{c2})^2}{2{w_2}^2}\right) \quad (2.3)$$

where A and A_2 are the amplitudes, x_c and x_{c2} the centres, corresponding to average FRET efficiency values, w and w_2 the widths of the distributions. The centres and the widths were global parameters, and the amplitudes were local parameters. The fitted Gaussian distributions were integrated and divided by histogram bin width (0.05) to give the total number of oligomers in each population for each timepoint. In the cases where the histograms displayed a single peak, they were integrated and divided by histogram bin width (0.05) to give the total number of oligomers for each timepoint. The resulting numbers of oligomers, plotted against aggregation time, formed the basis of the oligomer kinetic traces. In order to obtain a more conventional representation of the kinetic traces, showing the change in oligomer concentrations with time, further corrections were performed. Firstly, the numbers of oligomers were normalised to the average monomer bursts, taken at the beginning of the aggregation process where the monomer bursts did not undergo a rapid decrease due to monomer depletion. To note, the value of the average monomer bursts was twice the average value of the bursts arising from AF488-labelled monomer, to account for the 1:1 stoichiometry of the AF488 and the "invisible" AF594 monomer in the sm-FRET experiments. This gave an approximate estimate of oligomer fractions in the samples. Subsequently, the fractions were multiplied by the starting total protein concentration (μM) to give approximate oligomer concentrations.

The kinetic traces of monomer depletion were obtained from the selected monomeric burst counts above the chosen threshold, normalised to the monomeric burst counts at time zero to give the monomer fractions, and multiplied by the starting bulk protein concentrations.

2.10 Apparent oligomer size distributions from sm-FRET experiments

In the sm-FRET experiments, the apparent size distributions of oligomers were derived using fluorescence intensity values of the simultaneous bursts, according to the following equation:

$$Apparent\ \ size = 2 \times \left(\frac{I_D + \gamma^{-1} I_A}{I_{Dmonomer}} \right) \tag{2.4}$$

where I_D is the donor intensity in the presence of an acceptor, I_A is the acceptor intensity and γ is the gamma factor (0.99) and $I_{Dmonomer}$ is the average intensity of donor monomers. The expression estimates the number of donor monomers per oligomer, and the factor of 2 is due to assumed 1:1 dye stoichiometry in the oligomers. Large species, either occupying neighbouring bins, or more than 150-mers in size, were excluded, as these were assumed to originate from fibrils. These size distributions have units of number of monomers per oligomer (abbreviated as "–mers" throughout), and are termed "apparent" as they serve to broadly reflect the changes in the average populations of oligomer sizes rather that to report on the discrete sizes of oligomers. This limitation in the size estimation is due to the inhomogeneous laser excitation, stochastic nature of fluorescence emission and potentially different paths the oligomers can take through the confocal volume during the detection. The determination of exact physical sizes of individual oligomers of αS has been achieved previously by other methods such as single-molecule photobleaching[94] or analytical ultracentrifugation[84], and is beyond the scope of the present method.

2.11 TCCD data acquisition

The coincidence in TCCD experiments can be quantified using the association quotient Q, defined in eq. 2.1. In these experiments, Q value arising purely due to chance coincidence events was determined by analysing free AF dyes in solution, as will be detailed in the subsequent chapters. This was done in order to adjust the sample concentration to ensure the measurements in single-molecule regime, and data acquisition at a total concentration of 100 pM or less was found optimal. Following the dilution, solutions were immediately introduced into a straight channel of a microfluidic device via a gel-loading tip and withdrawn at a constant rate of 1 cm s^{-1} via a syringe pump, as in the sm-FRET measurements. Overlapped laser beams were focused into the middle of the channel. For each sample, data were typically acquired for 600 s, with 100 μs bin-width, chosen according to the expected residence time in the excitation region at the chosen flow speed[114], 100,000 bins per frame and a total of 60 frames. The fluorescence photon traces in two separate channels, the emission from AF488 and AF594 dyes (or AF647, when 1:1 AF488 and AF647 samples were used, and the setup was operating in 488/647 mode), were collected simultaneously and outputted using custom-programmed FPGA (Colexica). All measurements were made at ambient temperature around 20°C, similarly to sm-FRET measurements.

2.12 TCCD data analysis

The collected photon traces were analysed using custom-written Igor Pro 6.22 (Wavemetrics) software (written by Dr. M. Horrocks) analogous to previously described[115]. The data were corrected for autofluorescence and for crosstalk. Photon bursts with intensities greater than the threshold of 15 photons bin^{-1} in the blue and in the red channels were selected according to previously established threshold selection approach that allowed maximising the detection of coincident events. Simultaneous events in both channels above the threshold (the AND criterion[118]) were selected. To account for any possible coincident events due to chance, the desynchronisation approach was used[117]. Time-bins in the blue channel were randomly re-numbered before the selection of simultaneous events in the two channels above the threshold. Using these outputs, the association quotient Q was estimated according to eq. 2.1.

2.13 Bulk ThT measurements

Bulk thioflavin-T (ThT) assays were performed to monitor fibril formation by αS, incubated at the same conditions as the samples used for sm-FRET experiments. For the assays, either unlabelled wt αS was used, or AF594-labelled αS, and the same buffer and incubation conditions as described for sm-FRET assays. The aliquots were withdrawn at the same time intervals as for the sm-FRET measurements. Withdrawn aliquots were pre-mixed with ThT solution to contain 18 μM of this dye. Measurements were performed on Cary Eclipse spectrometer with 440 nm excitation and emission at 470-600 nm. Maximum intensity values from the background-corrected fluorescence spectra were plotted against incubation time.

2.14 TEM imaging

For transmission electron microscopy (TEM) imaging, the sample preparation was the same as for the solutions prepared for the sm-FRET or TCCD experiments, and either labelled αS, unlabelled αS or other protein samples were used at a range of starting concentrations from 10-70 μM, unless specified otherwise. ~10-15 μL volumes of the samples were applied onto carbon-coated 400-mesh copper grids (EM Resolutions) for 5 min, and washed with distilled water. Negative staining was carried out by using 2% (w/v) uranyl acetate. TEM images were acquired using Tecnai G2 microscope (13218, EDAX, AMETEK) operating at an excitation voltage of 200 kV.

Chapter 3
Aggregation of αS studied by sm-FRET

In this chapter, the aggregation of αS protein is studied by sm-FRET, and the results are put into the context of its spreading in PD. Firstly, literature is reviewed that supports the spreading of αS aggregates both in disease and in various model systems. Two types of αS oligomers previously identified in this laboratory by sm-FRET technique are introduced. Subsequently, sm-FRET experimental results of the aggregation of αS at a range of starting protein concentrations are presented, along with the optimisation of these experiments. The differences in the concentrations and FRET efficiency distributions of the generated oligomer populations are shown, depending on the starting protein concentrations. Following this, the results of kinetic modelling of the αS aggregation datasets are presented, and the main predictions derived from this analysis are discussed. Finally, based on the predictions, a hypothetical primary role of αS aggregates upon entering a cell during the spreading process is suggested.

3.1 Introduction: Prion-like hypothesis of αS spreading

3.1.1 Spreading of αS aggregates in disease

The deposition of the insoluble αS inclusions in PD and related synucleopathies follows a specific pattern which correlates with clinical symptoms. This specific pattern of deposition appears to be different in different types of synucleopathies, as was established based on autopsy studies. Two commonly accepted classifications are McKeith classification[119], used mostly for the description of the spreading of αS in DLB, and Braak staging[120], commonly used for PD. According to Braak staging, the progression of αS pathology starts in the gut and olfactory system, and spreads along the brainstem to the vagal nerve, reaches the substantia nigra, advancing to the limbic structures and in the final stages progresses to neocortex[120]. This specific pattern is known as ‘gut-to-brain’ spreading of pathology[121]. It is not universally present in all PD patients, and there is some controversy about the various details of the classification[122], although the general pattern of the spreading is widely accepted, and is frequently well-correlated with the appearance and the increasing severity of clinical symptoms. For example, the olfactory system is one of the earliest systems to suffer, according to this staging pattern, and indeed hyposomnia is present in around 90% of the early-stage cases of sporadic

PD[123]. It is interesting to note that LB inclusions are also observed in about 10% of people aged over 60 who do not exhibit any symptoms of pathology. Neverteless, these patients have decreased levels of dopaminergic and noradrenergic neurons, alghough to a lesser extent than the patients with clinical symptoms[124]. The identification of this form of LB pathology, termed as incidental LB disease, shows that the disease may begin much earlier than the pathological symptoms become evident. It was found that the aggregates found in PD were more stable in comparison to the aggregates found in the incidental LB disease[125].

In additional support of the fact that αS deposits are able to spread, striking observations were made in PD patients who underwent a surgery in 80s and 90s, which involved grafting young neuronal cell transplants into their striatum in order to restore the neurotransmission of dopamine. Over years after this surgery, the transplaned neurons had developed LB deposits, corroborating the fact that the aggregates could spread during the disease[126]. Despite the fact that the spreading of αS lesions was observed and correlated with the pathology, it remains unclear what is the molecular-level mechanism driving this process, and whether this spreading is cell-driven, protein-driven or is a consequence of a combination of several driving forces. For example, there exists an opinion that the above mentioned Braak stages are a consequence of different properties of neuronal cells in the different parts of the brain, specifically, their proneness to protein aggregation, and therefore the observed aggregation is cell-driven[127]. One other increasingly popular explanation is the prion-like hypothesis, which originates from the discovery reported by Prusiner in 1982 that prion protein was the constituent of the infectious particles causing scarpie disease[128]. The proposed underlying mechanism of prion propagation was that the prion aggregates were able to act as templates in order to induce a very rapid stochastic misfolding of the normally present soluble proteins, this way generating a cascade of insoluble pathogenic protein aggregates. Later, based on numerous experimental reports demonstating the spreading of other amyloidogenic proteins, such as amyloid-beta and tau, along with multiple similarities between the resulting protein-folding diseases, it was proposed that their spreading was goverened by a ‘prion-like’ mechanism[129].

At the molecular level, the prion-like propagation is frequently linked to the process of templated seeding, in which the aggregates of αS act as templates to promote the misfolding and aggregation of soluble protein molecules[130] in the same manner as prion protein. The prion-like hypothesis of αS propagation has gained a lot of attention over the recent years[127,131,132]. However, it has not been universally accepted, and the prion-like role of αS in the process of its pathological spreading is still under debate[133], numerous alternative hypotheses exist to explain the observations, and the research in this area is actively progressing in order to both pinpoint the molecular origins of the process, and attempt to prevent or slow down the propagation of pathogenic aggregates[127].

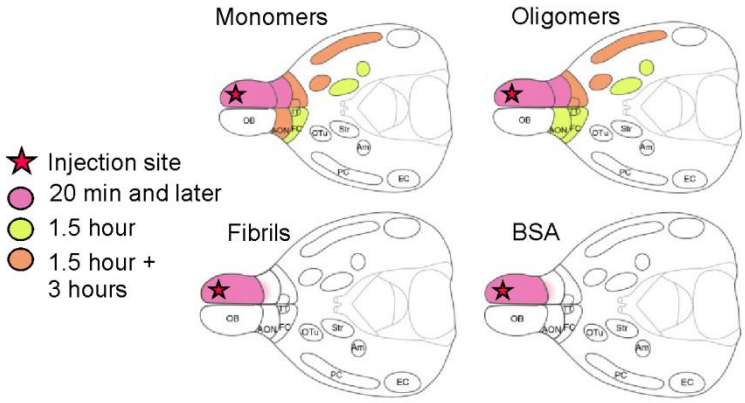

Figure 3.1. Temporal evolution of αS aggregates after the injection of different forms of human αS into olfactory bulbs of wild-type mice. The shaded areas denote cells positive for human αS at the specified time points past injection, and indicate a faster transfer of monomers and oligomers in comparison to fibrils of αS. (Figure from Rey *et. al*., 2013)[134].

3.1.2 Experiments to mimic the spreading of αS in animal models and cell culture

Numerous experiments have attempted to recapitulate the spreading of αS aggregates in various biological systems, such as cultured cells and animal models. For example, cell-to-cell transmission of αS by endocytosis and exocytosis in neuronal cell culture was demonstrated, and found to occur concomitantly with lysosomal disfunction and cell apoptosis[135]. Seeding was demonstrated to occur in neuronal cells upon the addition of αS oligomers[136]. The transfer of αS was observed from the brains of transgenic mice to grafted neurons[137]. Studies performed in wild-type and transgenic mice showed that injection of fibrils of recombinant αS could lead to the aggregation of the endogenous protein[138-140]. Experiments in monkeys demonstrated that injections of brain extracts from PD patients, containing LBs, into brains resulted in progressive neuronal cell death[141]. Interestingly, injections of distinct types of αS species, either monomers, oligomers or fibrils, were made into olfactory bulbs of transgenic mice[134]. The outcome of these was that the aggregate spreading was observed between the brain regions inter-conneced by axons, and that fibrillar aggregates travelled slower than monomers and oligomers, as is illustrated in Fig. 3.1. In addition to the numerous reported observations of the ability of αS aggregates to transfer between neurons, it was demonstrated that they could travel from neurons to oligodendrocytes, a type of glial cells in nervous system[142], adding a further dimension towards the complexity of the spreading process. To note, αS is not expressed in glial cells in healthy adult human brain[143], and the pathological transfer from neurons to glia may potentially be a useful feature from the diagnostic standpoint. Indeed, the deposits of αS were observed in oligodendrocytes in addition to neurons in patients with MSA[144] and PD[145], however, reports have demonstated that αS micro-RNA expression was absent, at least in the cases of MSA[146]. The fact that αS is capable of

transmitting between the cells where it is originally expressed to the cells where it is not expressed further strengthens the fact that it can spread. One key conclusion from the *in vivo* studies of the spreading of αS was that in order to be efficient, the process required the presence of endogenous αS protein. Therefore, pathogenic propagation was found to be not sustainable in αS-knockout animals[147]. Interestingly, in additional support of the direct connection between the aggregate spreading and cellular damage, normally observed in cell culture and animal models, the selective fate of the aggregate-containing neurons was unambiguously demonstrated in transgenic mice[148].

3.1.3 Experiments to model the spreading of αS *in vitro*

In vitro experiments have also addressed the intriguing phenomenon of αS spreading. To recap, αS is an unfolded IDP in solution, at neutral pH and physiologically-related temperature, whereas undergoes a conformation reorganisation when conditions are altered, for example, at low pH[149]. It is known from a large number of *in vitro* experiments that in aqueous solution, synthetic αS can self-assemble into fibrils, which are morphologically similar to the ones found in LBs[104,150] and have a cross-β-sheet structure[98]. It was demonstrated that the addition of pre-formed fibrillar aggregates to monomeric αS in solution accelerated its aggregation. This phenomenon is known as 'seeding'[104], and it has been identified for various isoforms of αS, including its pathological point-mutants[151]. Additionally, it was shown that during the *in vitro* aggregation of αS, the aggregates could multiply in acidic buffer, which may be relevant to the environment present in cellular endosomes[152].

3.1.4 Two types of αS oligomers previously identified by sm-FRET method

In this laboratory, sm-FRET technique was used to study the aggregation of αS *in vitro* at the starting concentration of 70 μM. In the study published in 2012[79] two distinct types of αS oligomers were observed during the aggregation process. These types of oligomers were distinguished based on their FRET efficiency distributions (eq. 2.2). The initially formed oligomers were characterised by FRET distibutions centered at lower values, and were termed "low-FRET oligomers". The oligomers formed at later times were characterised by the FRET distributions centered at higher values, and were therefore termed "high-FRET oligomers". The high-FRET species were characterised by a distribution of apparent sizes ranging from 5-150 monomer units, where the apparent sizes were derived from fluorescence emission and served only as estimates due to the different trajectories that oligomers can take through the confocal volume and the stocastic nature of fluorescence emission. The high-FRET oligomers were found to be more resistant to enzymatic digestion, more cytotoxic and more stable towards the changes in buffer conditions compared to the low-FRET types, confirming

that the changes in FRET efficiency distributions represented the changes in αS oligomer structures[79,115]. The two identified types of oligomers were proposed to be two sequential intermediate species on the pathway to αS fibril formation.

3.2 Methods

3.2.1 sm-FRET experiments to monitor the aggregation of αS

Sm-FRET experiments were carried out with the oligomer samples at a range of starting total αS concentrations from 0.5-140 μM according to the protocols described in General methods, section 2.4.

3.2.2 TIRFM sample preparation

For total internal reflection fluorescence microscopy (TIRFM) imaging, αS was 1:1 AF488 and AF647 dual-labelled, and buffer and incubation conditions were the same as for the samples in sm-FRET experiments. Samples with starting protein concentrations of 5 and 70 μM were incubated for >54 h to allow characterisation of oligomers at the steady state, and fibrillar material was removed by centrifugation for 10 min at 12,800 x g. Borosilicate glass slides (631-0122, VWR International, 20x20 mm) were cleaned by argon plasma (PDC-002, Harrick Plasma cleaner) for 1.5 h. Subsequently, frame-seal slide chambers (SLF-0601, Bio-rad, Hercules, CA, USA, 9x9 mm) were attached to the glass and 70 μL Poly-L-lysine (P4707-50ML, Sigma-Aldrich, mol wt 70,000-150,000) added on top and incubated for 30 min before being washed with Tris buffer of the same composition as used for the aggregations. Each glass slide batch was checked for the absence of fluorescent artefacts by imaging a buffer-containing blank slide. For imaging, protein was diluted to 100 pM concentration, added to the coverslide and incubated for 10 min.

3.2.3 TIRFM data acquisition

Imaging was performed using a home-built TIRFM setup (built by Dr. P. Jönsson) described previously[153]. Inverted Nikon Eclipse TE200 microscope (Nikon Corporation, Tokyo, Japan) was used and a 60× magnification (Plan Apo TIRF, NA=1.45) oil-immersion objective (Nikon Corporation). Dual illumination by a diode laser operating at 488 nm (PC13589; Spectra Physics, Canada) and a He:Ne laser operating at 633 nm (25LHP, Melles Griot, CA) were utilised. The TIRF mode was achieved by adjusting the position of aligned laser beams before they entered the objective. Fluorescence signal was split by a DualView (Optical Insights, Lilburn, CA) mounted dichroic and

after being separated into two colours was simultaneously recorded on each half of the chip of Photometrics Cascade II:512 EMCCD camera (Photometrics, Tucson, AZ). To adjust the overlap of images in both channels, a grid with evenly-separated holes in gold-on-glass was used. Data were acquired using MicroManager[154], and the dimensions of the recorded images were 512×512 pixels, with a pixel size of 107×107 nm in the sample plane. The acquired datasets consisted of short video files, recorded by stream acquisition of 50 images with an exposure time of 100 ms. A new coverslide was used for every 25 videos to avoid recording pre-bleached species. 200 videos were recorded per protein sample, and three separate sample preparations were analysed for 5 µM concentration (total of 600 videos), and the same number for 70 µM concentration. All measurements were made at ambient temperature (c.a. 21°C).

3.2.4 TIRFM data analysis

Using TIRFM data, apparent sizes of oligomers were determined by normalising oligomer fluorescence intensities to the average monomer brightness as described in previous studies[111]. Briefly, the data were analysed using custom-written MATLAB software (R2011b, MathWorks, Natick, MA), developed by Dr. K. Ganzinger. The fluorescence images were background-corrected and spots detected above empirically determined thresholds, (5 and 7 std above the background for the blue and the red channel) chosen to be in agreement with what is detected by eye. Firstly, by analysing predominantly monomeric data the average 647-labelled monomer intensity ($I_{monomer}$) was determined. It was defined as the average intensity of detected spots in the first frame prior to photobleaching (N=5,123) minus the average intensity of the spots in the last frame after the photobleaching and was 41 ± 0.6 (sem) counts. Subsequently, oligomer intensities were extracted from the red (AF647 fluorescence) channel (I_{red}). Oligomers were distinguished from monomers by detecting coincident spots in the red and the blue channels, with a requirement for the colocalized particles to stay within 300 nm of each other to account for any limitations in image registration (c.a. 120 nm) and localisation precision (c.a. 50 nm for both detection in the blue and red channels). A centroid fit to the bright objects was followed by a Gaussian fit, and the extracted intensity values corresponded to the amplitudes of the Gaussian fits[155]. The intensities were averaged over multiple frames prior to photobleaching. To determine the apparent sizes, the oligomer intensities were doubled to account for the "invisible" blue fluorophores (since oligomers were created by aggregation of a 1:1 mixture of AF488 and AF647 labelled protein monomers), and divided by average monomer brightness determined:

$$Apparent\ size = \frac{2 \times I_{red}}{I_{monomer}} \tag{3.1}$$

The apparent size values were represented as histograms with bin-widths of 1. The size distributions were corrected to account for potentially present non-coincident singly-labelled oligomers, by multiplying each size population by the factor based on the binomial probability, which corrects for the assumption that each oligomer contains an equal number of red and blue fluorophores:

$$F_{one-colour} = \frac{2^x}{2^x - 2} \quad where \;\; x\,is-mer \geq 2 \tag{3.2}$$

3.3 Results

3.3.1 Results of control bulk and TEM imaging experiments to verify the ability of AF-labelled αS to assemble into fibrils

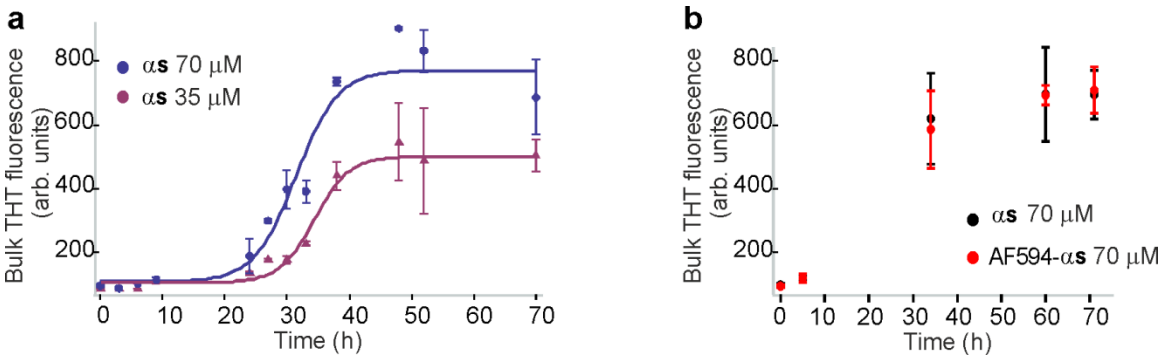

Figure 3.2. a. Bulk ThT fluorescence traces, showing the progression of fibril formation for unlabelled wt αS at the same incubation conditions as for the sm-FRET experiments. (n=3, std). Fit to sigmoid function with $t_{1/2}$(70 μM)=31.5±1.3 h and $t_{1/2}$(35 μM)=34.3±0.9 h (error from the fit). **b.** Progression of fibril formation, monitored by ThT fluorescence emission, using either unlabelled wt or AF594-labelled αS at 70 μM (n=3, std).

For sm-FRET experiments presented in this chapter, αS with an alanine to cysteine mutation at the residue 90 of αS (A90C) was used, which enabled the attachment of a single AF dye per protein molecule. The mutation was demonstrated not to significantly affect the aggregation properties of αS in the previous studies from this laboratory[79,115,156], because the residue 90 is located at the periphery of the β-sheet core. In order to confirm this, bulk ThT measurements and TEM imaging experiments were carried out according to the protocols described in General methods.

Firstly, bulk ThT fluorescence traces were recorded, employing ex-situ measurements upon withdrawal of αS aliquots from the samples incubated under the same conditions as in the subsequent sm-FRET experiments (in the dark at 37°C with constant agitation at 200 rpm). In Fig. 3.2.a, the

resulting fluorescence intensity traces indicate that fibril formation under these experimental conditions is detectable past 24 h and reaches a plateau phase after 40 h. Interestingly, there is no large difference between the time-frame of this process when the starting αS concentration is halved, and an equilibrium phase is reached within 40 h both at 70 µM and 35 µM concentrations. Therefore, this time-period is the most interesting for monitoring the formation of oligomers, since their formation is expected to precede fibril formation. Secondly, the aggregation was monitored by bulk ThT assay for both unlabelled wt αS as well as AF594-labelled αS under the same incubation conditions (Fig. 3.2b), and a close time-progression was observed, confirming that the attachment of the AF tag does not substantially interfere with the aggregation process. Finally, dual-labelled samples of AF488 and AF594-tagged αS were incubated over a period of 3 d under the same conditions as for the bulk ThT and sm-FRET experiments, and imaged by TEM (Fig. 3.3.). The presence of amyloid fibrils and no evidence of amorphous aggregation support the absence of substantial influence of the attachment of AF dyes to αS on its aggregation propensity.

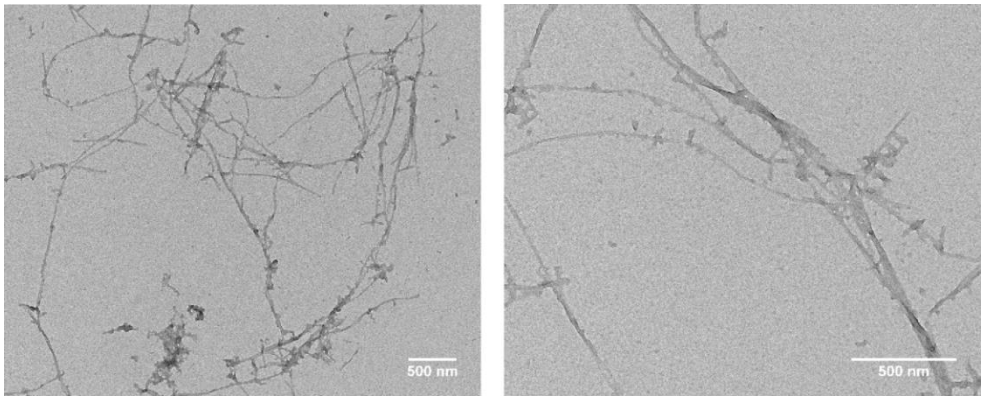

Figure 3.3. Representative TEM images of fibrils, formed by AF-labelled αS. 1:1 AF488 and AF594-labelled αS samples are prepared under the same incubation conditions as the samples for bulk ThT and sm-FRET experiments. After prolonged incubation with agitation, fibrils are observed.

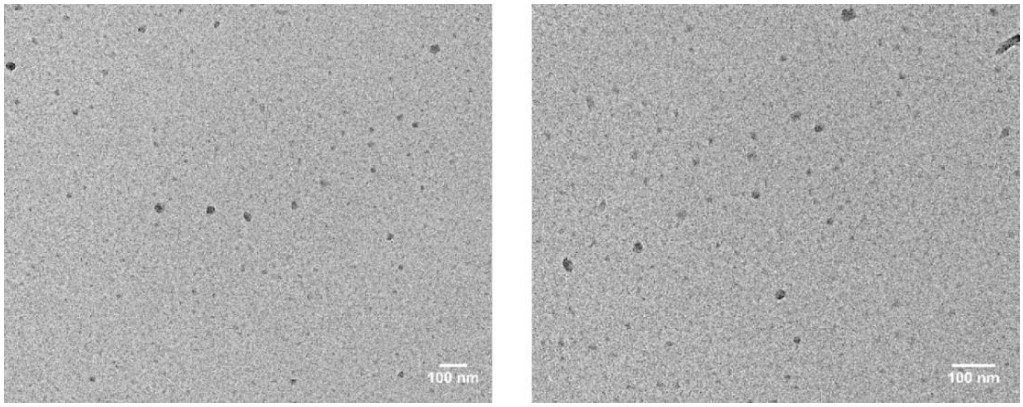

Figure 3.4. Representative TEM images of oligomers formed by 1:1 AF488 and AF594-labelled αS samples with the starting protein concentrations of 70 μM (left) and 35 μM (right), incubated for 24 h at the same conditions as for the bulk ThT experiments and sm-FRET measurements, followed by centrifugation for 10 min at 12,800 x g in order to remove large fibrils. Spherical oligomers and a low number of short protofibrils are present in the supernatant.

3.3.2 Results of control TEM imaging and sm-FRET experiments to verify oligomer formation by αS and to optimise detection conditions

Once it was confirmed that the fluorescently-labelled protein was able to assemble into fibrils, its oligomerisation properties were investigated. Firstly, oligomers of αS were visualised by TEM in order to confirm their presence and to determine their morphology. These species were smaller than amyloid fibrils, as expected, and round-shaped, as shown in Fig. 3.4.

Subsequently, the incubation conditions were varied in order to select optimum conditions for oligomer generation. While it is known that αS assembles into fibrils in the presence of shear forces, its oligomer formation was reported upon incubation either with[79] or without[84] shaking, and its efficiency was found to depend on many factors such as shaking rate, buffer conditions and the starting protein concentration. Thus, comparative sm-FRET experiments were performed, where αS oligomerisation was monitored in solutions at 0.5-35 μM both in the presence and in the absence of shaking. The results in Fig. 3.5 show that the oligomerisation was more efficient with shaking, judged by higher numbers of oligomers detected under these incubation conditions.

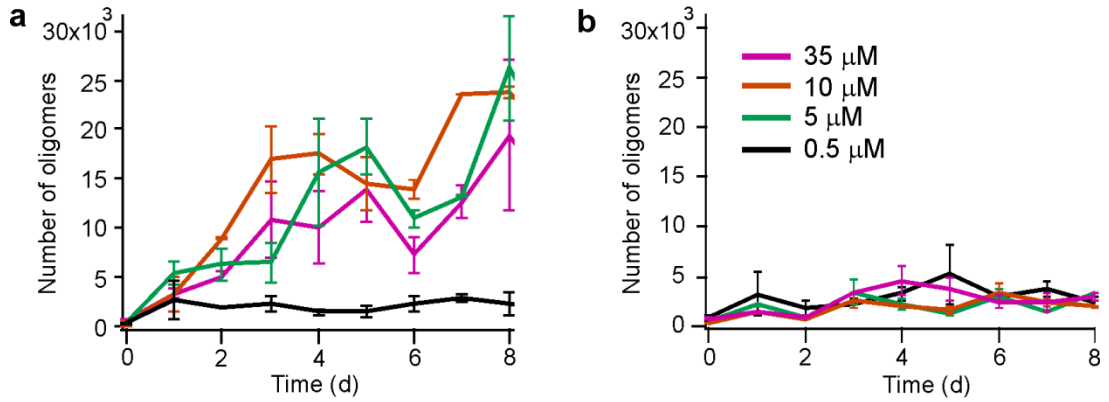

Figure 3.5. Results of sm-FRET assays monitoring the numbers of oligomers formed in the samples of αS at 0.5-35 μM concentrations upon incubation with shaking (**a.**) or under quiescent conditions (**b.**) (n=3, sem).

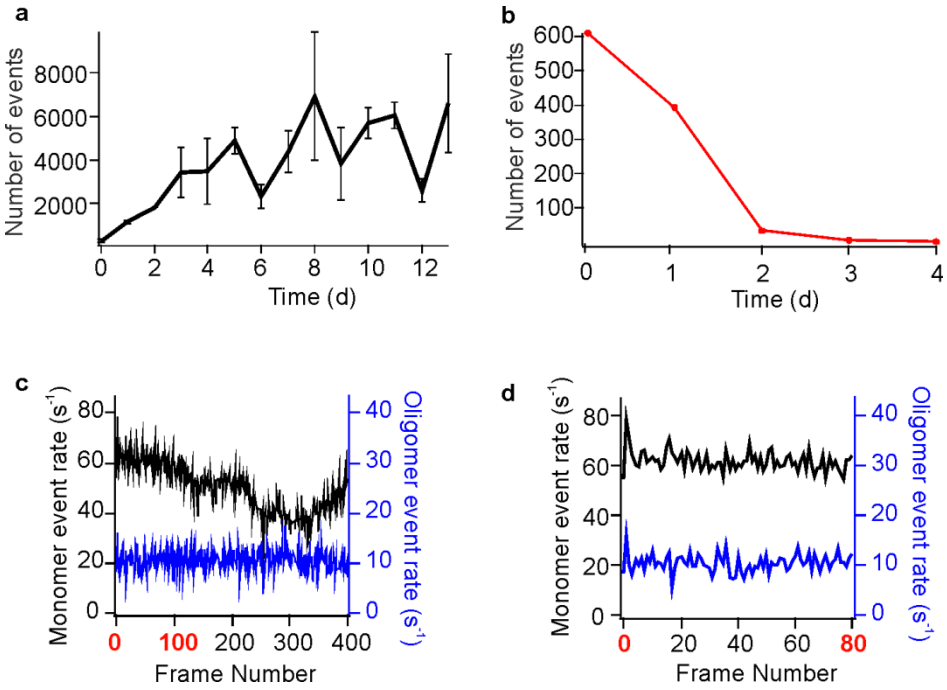

Figure 3.6. Sticking controls for αS oligomerisation experiments. **a.** 35 μM solution of αS incubated in DNA low-bind test-tubes (Eppendorf) (n=3, sem). **b.** 35 μM solution incubated in a non-coated flat-cap test-tube (Star Lab). Drop in the detected numbers of oligomers is due to their sticking to the walls of the test-tube. **c.** Representative traces of monomer burst rate and oligomer burst rate, resulting from sm-FRET measurement using 35 μM aggregated αS sample and detection up to 2,000 s (400 frames). **d.** Within the first 400 s (80 frames) of detection, both the monomer and oligomer burst rates are stable, indicating the absence of either sticking or dissociation within this detection time-period.

It was additionally confirmed that not only the presence of shear forces, but also the choice of the test-tubes used for the incubation of αS samples affected the results, and test-tubes with hydrophobic coating enabled the oligomers to stay in solutions and not to adhere to the walls of the test-tubes, as is illustrated in Fig. 3.6 a and b.

Furthermore, the potential sticking or oligomer dissociation during sm-FRET measurement were considered during the choice of experimental conditions. Since the solutions were analysed in single-molecule regime, this required their high dilutions up to ~280 pM concentration of αS. In order to select a detection time over which there was no appreciable oligomer dissociation, the event rates of coincident bursts versus time were analysed (Fig. 3.6). In addition, because the protein solutions can encounter many surfaces during the sm-FRET detection, such as the walls of a gel-loading tip used as a vessel and surfaces of the microfluidic channel, sticking of both monomer and oligomers can occur during the detection. Therefore, the event rates of detected monomeric bursts over time were also analysed in order to select a detection time-period where the event-rates were stable (Fig. 3.6 c and d).

The final consideration for choosing optimum conditions for sm-FRET aggregation experiments using αS was whether large fibrillar species present in the aggregating samples strongly contributed to the signal. As it has been detailed in General methods (section 2.8), sm-FRET experiments are designed to be selective for small aggregates, because large species occupying consecutive time-bins are excluded during the analysis, as well as the species that are assigned apparent sizes of 150-mers and more. The effectiveness of the size-exclusion method was previously validated by Dr. M. Horrocks[115]. From the recorded bulk ThT traces (Fig. 3.2), even though amyloid fibrils are detectable in αS solutions during the second day of the aggregation reaction, their concentration is higher on the third day. In order to check whether the size-exclusion approach in sm-FRET experiments was sensitive to the concentration of fibrils, aggregation timecourses were recorded over a period of 54 h. In these measurements, the protein solutions were recorded either immediately after their withdrawal from the aggregating samples, or following centrifugation of the withdrawn solutions for 10 min at 12,800 x g to separate insoluble fibrillar pellets before the sm-FRET analysis. These experiments were carried out using relatively high starting αS concentrations, 70 μM and 35 μM, since at these concentrations fibril formation was found to be very efficient under shaking conditions. From the results (Fig. 3.7), there was no noticeable difference in the numbers of detected oligomers in either case over a period of first 33 h of incubation, indicating that the contribution of fibrillar species was negligible in the sm-FRET experiments during this time period, and generally small within 54 h.

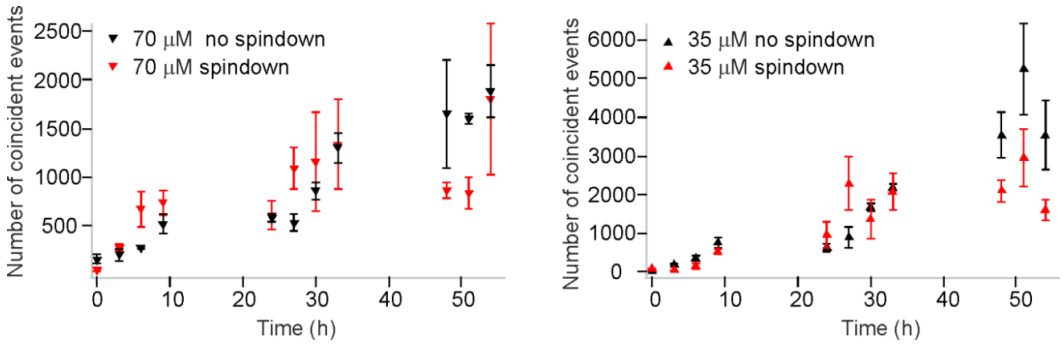

Figure 3.7. Control sm-FRET measurements to assess a potential contribution from large fibrils to the signal in the kinetic measurements of oligomer formation (n=3, sem). Dual-labelled samples of αS were incubated at 70 μM and 35 μM starting concentrations, and the sm-FRET measurements were carried out using the samples either directly withdrawn from the incubating solutions (shown in back), or using the supernatants of the samples after centrifugation for 10 min at 12,800 x g (shown in red). The results are represented in numbers of coincident events versus incubation time. The data are broadly unaffected within the first 33 h. Comparable numbers of aggregates present at this time regardless of the presence or the absence of centrifugation confirm that the signal at this time mainly arises from the small oligomeric species, and that the signal arising from fibrils that are already present at 24-33 h does not contribute to the measurement. At later times, higher numbers of aggregates are detected in the samples without centrifugation, presumably due to a contribution from fibrils which are highly abundant at this late incubation time. All of the subsequent sm-FRET measurements were performed without centrifugation, unless otherwise stated.

3.3.3 Results of sm-FRET oligomer formation by αS at a range of starting protein concentrations

In these experiments, αS oligomer formation was measured in solution at physiologically-related pH and 37°C (as detailed in General methods, section 2.4), with initial monomer concentrations of 0.5, 5, 10, 35, 70 and 140 μM using sm-FRET technique to follow the changes in the numbers of oligomers in the samples within first 54 h. As in all of the previously described control experiments, equimolar quantities of AF488 and AF594-labelled αS were combined up to the chosen starting concentration, allowed to aggregate and aliquots were withdrawn for the measurements at the times indicated. As has already been discussed, the attachment of AF dyes at the residue 90 of αS molecule was found not to significantly affect its fibril formation. In addition, because residue 90 is at the periphery of the fibril-forming NAC region of αS, attachment at this position results in the fluorophores becoming in close proximity on the formation of β-sheet structure during aggregation, enabling the conversion process to be followed by monitoring the changes in the FRET efficiency values (eq. 2.2 in General methods). As has already been stated, it was found in the previous works from this laboratory that lower FRET efficiencies were observed for initially formed oligomers lacking significant persistent structure, termed low-FRET oligomers, while higher FRET efficiencies were identified for more compact β-sheet-rich oligomers, termed high-FRET oligomers[79,115].

Within 54 h after the initiation of the aggregation reaction, oligomer formation was observed for all concentrations of αS, and the highest concentrations of oligomers were formed in the samples with the highest initial protein concentrations, and varied as a function of the initial monomer concentration, as shown in Fig. 3.8a. In this figure, the results for the solutions at 0.5 μM starting protein concentration are included but because the resulting oligomer concentrations are low in comparison to other data, these results are separately shown in Fig. 3.9. The FRET efficiency histograms of the oligomers measured at various timepoints (Fig. 3.8b), particularly at high starting protein concentrations, indicated the existence of two distinct populations. At early times, low-FRET population could be observed, centered at FRET efficiency value of ~0.4, which represented the initially formed, disordered low-FRET oligomers. At later times, the second population centered at higher FRET efficiency values was detected, corresponding to more compact, high-FRET oligomers, in agreement with the previous studies that were carried out at the 70 μM concentration of αS[79,115].

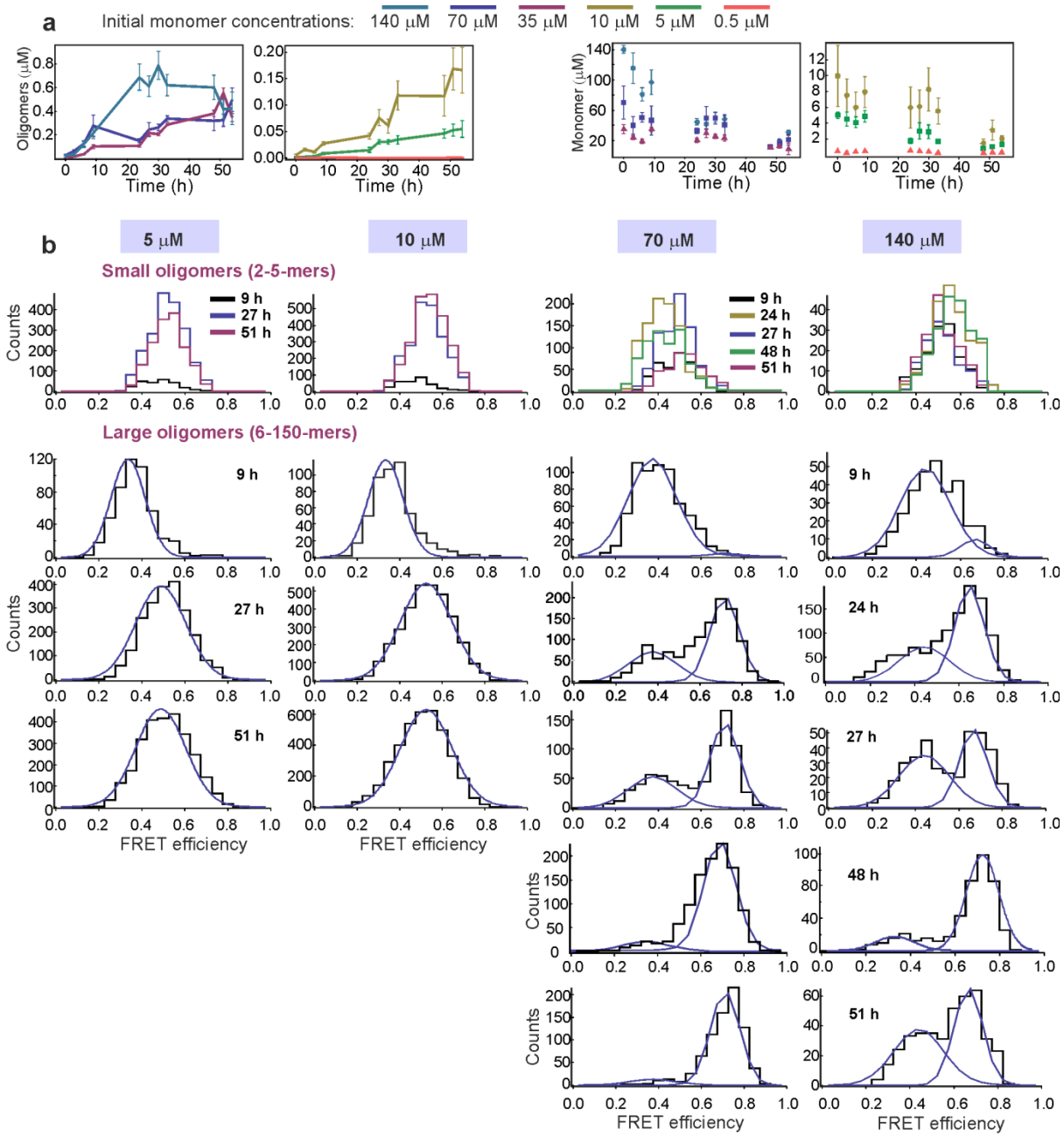

Figure 3.8. Results of the sm-FRET aggregation experiments using αS at a range of starting concentrations. **a.** Kinetic profiles of oligomer formation and monomer depletion, plotted against the incubation time (n=6, sem). To note, the increase in the oligomer concentrations for 0.5 μM solutions is present and the resulting species are in the low-nanomolar range, which is not readily visible on the scale in **a.** Magnification is shown in Fig. 3.9. **b.** Representative FRET efficiency histograms, resulting from sm-FRET aggregation experiments with initial protein concentrations of 5, 10, 70 and 140 μM, detected over 400 s. The data were split into two apparent size groups: small (2-5-mers) and large (6-150-mers) oligomers. For the large oligomers, illustrative fits to Gaussian functions are shown in blue (eq. 2.3), and the resulting mean FRET efficiency values, E, were: for 5 μM, 9 h E=0.34, 27 and 51 h global E=0.49; for 10 μM, 9 h E=0.33, 27 and 51 h global E=0.52; for 70 μM, global E(low-FRET)=0.37 and global E(high-FRET)=0.71; for 140 μM, global E(low-FRET)=0.44 and global E(high-FRET)=0.67. Further details of the fitting functions and the resulting average parameters (n=6) are in section 3.3.3. and Table 3.1.

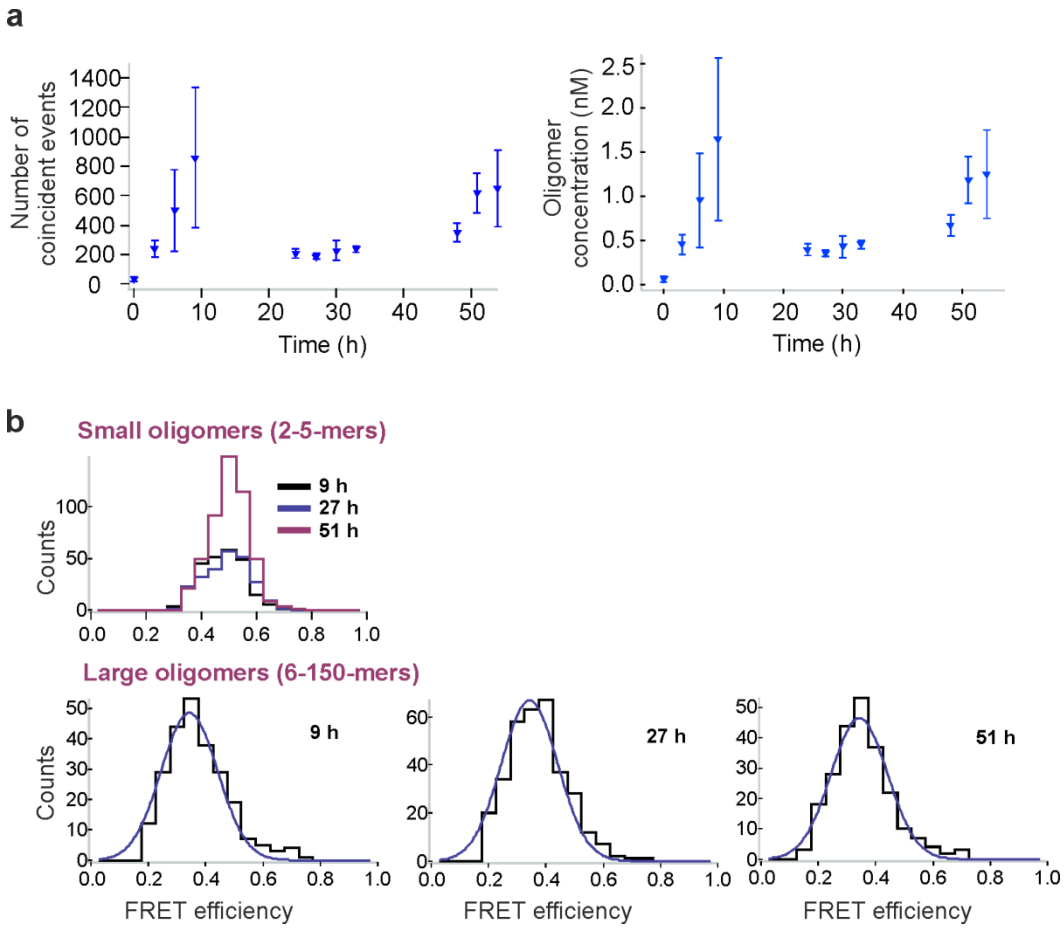

Figure 3.9. Sm-FRET results of αS aggregation at 0.5 μM starting protein concentration. **a.** Oligomer kinetic profiles, represented both in numbers of oligomers versus incubation time, and the concentrations of oligomers versus incubation time (n=6, sem). **b.** Appearance of FRET efficiency histograms of samples with 0.5 μM starting protein concentrations. The histograms of large oligomers are fitted to the single-Gaussian function (eq. 2.3), with E(global)=0.34. No shift in the centres of the histograms is observed within the time of the aggregation experiment.

The experimental data were divided into groups with different oligomer apparent sizes, based on the number of peaks that were resolvable in the FRET efficiency histograms. Typically, in these data, one peak was observed at low apparent sizes probably due to low photon counts arising from small species, and two peaks were observed at larger apparent sizes, starting from 6-mers, as is illustrated in Fig. 3.10. Therefore, the groups included "small" oligomers containing 2-5-mers which showed one peak in the FRET histograms, and "large" oligomers containing 6-150-mers where two peaks could be identified in the FRET histograms. As has already been discussed before, species composed of more than 150-mers, and species occupying neighbouring time bins, typically observed in the samples past the first day of incubation, were assumed to arise from fibrils and excluded from the measurements.

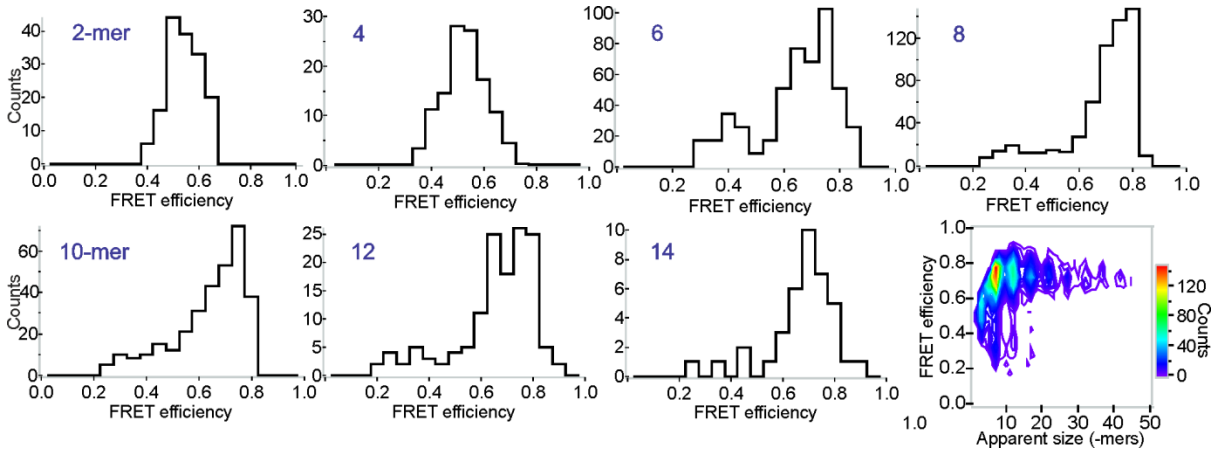

Figure 3.10. Appearance of FRET efficiency histograms resulting from a 35 µM sample of αS after 30 h of incubation and extended detection time (2,500 s), split into individual apparent sizes. Typically, the histograms display a single peak below 5-mers, due to the applied thresholds and low photon counts from these small species, and start to show two FRET populations at 6-mers and higher. This is the basis for splitting the sm-FRET data into size groups of 2-5-mers and 6-150-mers.

Examination of the histograms obtained for the lowest concentration samples (0.5 µM) showed that only the low-FRET population could be observed during the studied aggregation period (Fig. 3.9). For the 5 and 10 µM samples, the low-FRET distribution was clearly detectable during the first 9 h of the measurements, whereas at later times the histograms showed a much broader single distribution, and the overall oligomer concentrations were extracted without separation into the low- and high-FRET sub-populations (Fig. 3.8). FRET efficiency histograms for 35, 70 and 140 µM starting protein concentrations showed two distinguishable distributions attributed to low- and high-FRET oligomer types (Fig. 3.8b), and separate kinetic traces for both types were obtained using global fitting to a single Gaussian distribution for 2-5-mers, or a double Gaussian distribution (eq. 2.3 in General methods). The resulting parameters are in Table 3.1, where x_c and x_{c2} are the centres of the FRET efficiency histograms, corresponding to the average FRET efficiency values, and w and w_2 are the widths of the distributions.

Table 3.1. Parameters from the global fitting to GaussAmp functions (eq. 2.3). Error is std from n=6, where n is a dataset from a separate experiment.

conc	Small (2-5-mers)				Large (5-150-mers)							
	x_c	std(x_c)	w	std(w)	x_c	std(x_c)	w	std(w)	x_{c2}	std(x_{c2})	w_2	std(w_2)
(µM)												
35	0.532	0.005	0.087	0.002	0.399	0.066	0.105	0.010	0.641	0.017	0.0921	0.009
70	0.515	0.033	0.236	0.357	0.336	0.007	0.114	0.032	0.654	0.007	0.0951	0.009
140	0.539	0.007	0.085	0.003	0.423	0.038	0.099	0.008	0.629	0.010	0.0859	0.005

The centres and the widths were shared, and the amplitudes of the histograms were varied during the fitting procedure (eq. 2.3). The fits using the global parameters listed in Table 3.1 accurately described individual histograms up to (and including) 33 h, the early aggregation time period where the contribution from fibrils was negligible. Following this fitting, the kinetic profiles of low-FRET oligomer and high-FRET oligomer sub-populations were obtained, as reported previously for 70 µM samples[79]. The kinetic traces for these low- and high-FRET species separately are shown in Fig. 3.13b, and have distinctly different kinetics of formation, with the low-FRET population appearing and increasing within the first 24 h of the experiment, but the high-FRET population reaching a maximum value at longer times.

3.3.4 Results of oligomer apparent size populations derived from sm-FRET and TIRFM measurements

The apparent size estimation in sm-FRET experiments was based on oligomer fluorescence intensity, as discussed in detail in General methods (section 2.10), and the representative size distributions are shown in Figure 3.11. This shows that the majority of the species detected at all times in the aggregation reaction were smaller than 10-mers. The distributions displayed the progression to larger mean apparent sizes with time, indicating oligomer growth during the aggregation reaction.

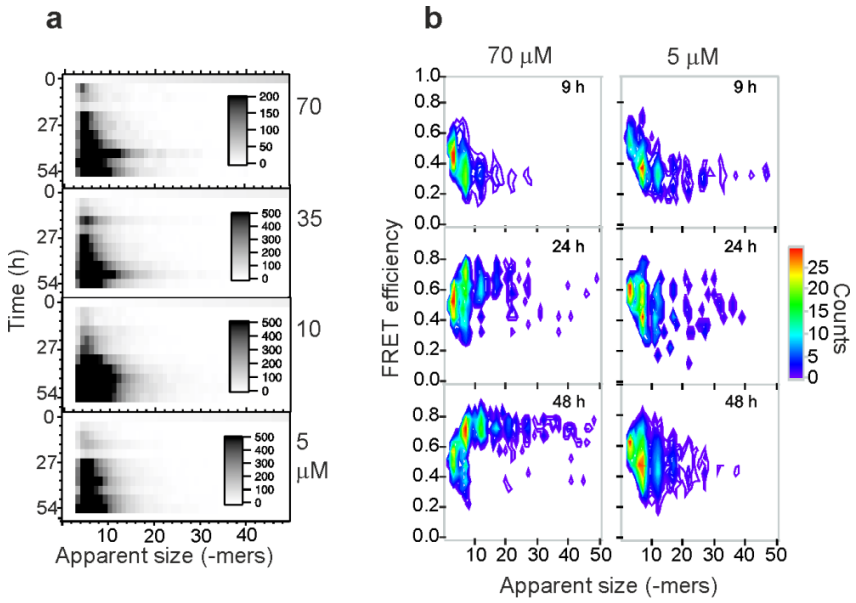

Figure 3.11. a. Number density histograms showing the evolution of apparent oligomer size distributions due to αS oligomer growth in the aggregation experiments for 5-70 µM samples. **b.** Representative contour plots of FRET efficiency against populated apparent oligomer sizes of 70 µM and 5 µM samples after 9, 24 and 48 h of aggregation. The conversion process from low-FRET oligomers to high-FRET oligomers at 70 µM is observed, as indicated by the shift in the mean FRET efficiencies to higher values.

Additional TIRFM measurements were performed to confirm the derived apparent size distributions, as detailed in the Methods section of this chapter (section 3.2). The results of these experiments are shown in Fig. 3.12. Interestingly, despite the differences in instrumentation used in this experiment in comparison to sm-FRET, the resulting apparent size populations were similar, indicating that the majority of species had the apparent sizes below 10-mers. The similarity is rather unsurprising considering that either method is based on the size estimation from fluorescence intensities, and indicates the absence of any strong preferential surface absorption of oligomers with specific apparent sizes, or substantial influence of the sample illumination geometry in these experiments.

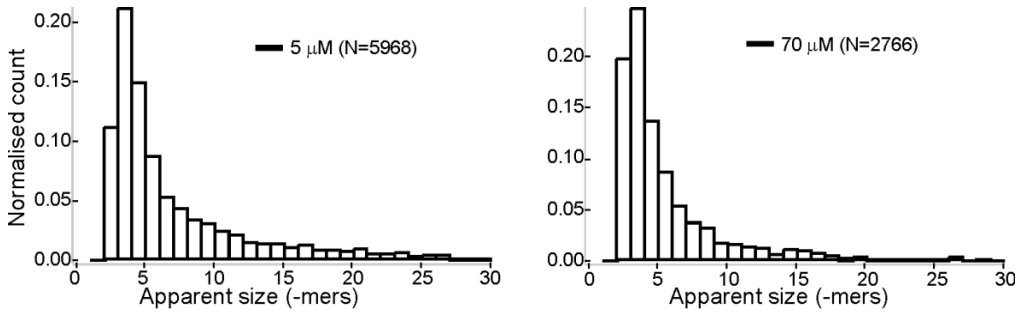

Figure 3.12. Apparent size distributions derived from TIRFM measurements of oligomers using 5 μM and 70 μM samples at the steady state. Similar to the apparent size estimation from the sm-FRET measurements, the values are derived from fluorescence intensities, as detailed in section 3.2. The results are in agreement with the data from the sm-FRET measurements. The total numbers of analysed oligomers are specified. Histograms are normalized to the total area. There is no substantial difference in the distributions derived for 5 μM and 70 μM samples.

While the fluorescence-derived size populations are termed "apparent" throughout this work and there are clear limitations in the determination of discrete sizes of oligomers from fluorescence intensities (discussed in 2.10), it is also worth noting that the precise size estimation of individual oligomers within mixtures has generally been very challenging. Multiple experimental approaches have been previously applied in order to overcome this challenge, with varying degrees of success. Size estimation of oligomers has been possible using atomic force microscopy imaging (AFM). However, because sample preparation requires immobilisation of the protein aggregates on a solid substrate, most commonly freshly-cleaved mica, it is potentially limited by a possible bias in the surface adhesion of oligomers of particular sizes. Moreover, it depends on the resolution of the AFM tip, which is known to be especially restricted in the lateral direction[157]. Size estimation using size-exclusion chromatography successfully separates oligomers from monomeric protein, as has been demonstrated in the studies of αS[84,89], whereas does not discriminate between the differently sized oligomer sub-populations. Similarly, gel electrophoresis also provides limited separation due to the restricted pore sizes of the used gels. Combination of size-exclusion chromatography and multiangle

light scattering has proven to be more successful, although able to discriminate between oligomer size groups with distinctly different mean size distributions rather than individual discrete oligomers. Using this method, for example, a sub-population of αS oligomers consisting of 30±6 monomers were separated[89]. Analytical ultracentrifugation has also been applied with a similar outcome, which allowed separating two distinct sub-populations of αS oligomers, with the average sizes of 18-mers and 29-mers[84]. Single-molecule methods based on fluorescence intensity, such as the methods presented in this work and previous studies[83,110,111,115,156,158,159], do not discriminate between low-order species effectively and instead reflect on the overall time-dependent or sample-dependent changes. One alternative and fairly promising experimental single-molecule approach for the size estimation is based on counting the fluorescence bleaching steps. This has been successfully applied to fluorescently-labelled amyloid-beta in order to characterise the exact stoichiometry of amyloid-beta oligomers[160], although was not suitable for the characterisation of high-order oligomers, larger than 20-mers, because of the inability to observe discrete bleaching steps in the aggregates bearing too many fluorophores. The latter issue was addressed by applying the fluorescence bleaching step counting method to study sub-stoichiometrically labelled protein molecules of αS to characterise larger species consisting of 31-mers[94].

3.3.5 Results of kinetic modelling of the profiles of oligomer formation and monomer depletion from sm-FRET and insights into αS spreading

Single-molecule timecourses recorded using sm-FRET at the range of the starting protein concentrations between 0.5 and 140 μM were subsequently analysed by Dr. G. Garcia, who applied a nucleation-conversion-polymerisation model in order to globally fit the datasets of monomer depletion and oligomer formation, and then made predictions of αS seeding behaviour using the parameters extracted from the fitting. These results are briefly described and reproduced in this section in order to illustrate how the sm-FRET data can be employed to study the mechanism of αS aggregation and to make predictions of this process under a variety of starting conditions that cannot be readily accessed experimentally. The applied nucleation-conversion-polymerisation model introduces a series of conformational conversion steps prior to fibril formation, as is schematically shown in Fig. 3.13a.

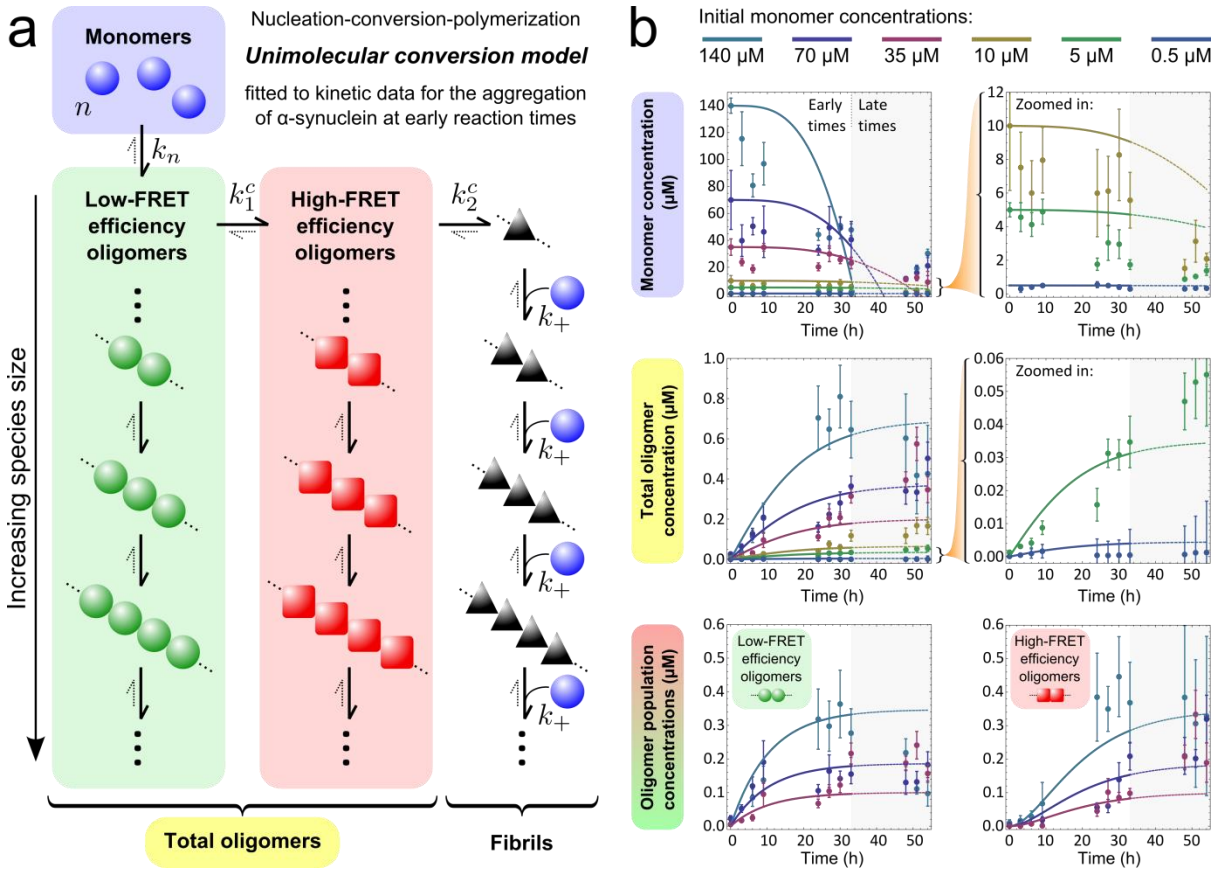

Figure 3.13. Modelling the kinetics of αS aggregation (Figure reproduced from Iljina & Garcia *et. al.*, 2016[83]). **a.** The model considers coarse-grained conversion reaction between oligomeric populations with no size dependence, and allows fibrils to grow once formed. Unimolecular conversions with no monomer dependence are assumed between populations. **b.** The resulting nucleation-conversion-polymerization model is used to describe the oligomer populations derived from sm-FRET, whereby monomer units form low-FRET oligomers with rate constant k_n and an average reaction order of n. These oligomers can then convert to ordered high-FRET oligomers via a first-order reaction with rate constant k_1^c, with a subsequent final first-order conversion to fibrils with rate constant k_2^c. Fibrils can then recruit single monomer units to grow in a succession of elongation steps, with a length-independent rate constant k_+. At early reaction times, reverse reactions were neglected, and conversion constants were fixed as equal such that $k_1^c = k_2^c \equiv k_c$. The resulting simplified model, with four free parameters, was fitted globally to early-time (up to 33 h) kinetic data showing changes with time in monomeric and oligomeric populations for a range of initial monomer concentrations. The resulting nucleation reaction order was found to be $n = 0.90 \pm 0.1$, with rate constants $k_n = (4.0 \pm 2.0) \times 10^{-4}\ \mu\mathrm{M}^{1-n}\mathrm{h}^{-1}$, $k_c = (9.5 \pm 5.0) \times 10^{-2}\ \mathrm{h}^{-1}$, and $k_+ = (9.0 \pm 7.0) \times 10^{-2}\ \mu\mathrm{M}^{-1}\mathrm{h}^{-1}$.

The model (developed and utilised by Dr. G. Garcia) considers a general mechanism where low-FRET oligomers are formed from monomeric units in solution. These low-FRET oligomers then convert to high-FRET oligomers, which in turn convert into fibrils. Fibrils then grow by monomer addition. A summary of the fitting results is shown in Fig. 3.13b, and the obtained parameters (listed in the caption of Fig. 3.13) are consistent with earlier results using sm-FRET datasets of αS aggregation at a single starting concentration of 70 μM[79,115].

To note, in this model oligomers are considered to be on-pathway to fibril formation, which is supported by several experimental observations. The presence of the lag phase in the formation of high-FRET oligomers relative to that of the low-FRET oligomers suggests that these species originate from the rearrangement of their preceding low-FRET species. This is further confirmed by the oligomer release upon fibril disaggregation, which has been observed in fibril disaggregation experiments carried out in previous work[79]. By the principle of microscopic reversibility this shows that both high- and low-FRET species are on the pathway to form fibrils. In addition, a correlation between the rates of the oligomer and fibril formation for αS and its pathological mutants has been recently observed in this laboratory, particularly the inhibition of both of these processes for A30P point-mutant of αS, further supporting the oligomer on-pathway nature[156]. Additionally, from the TEM imaging, the diameters of oligomers and fibrils generated in these experiments appear comparable (Figs. 3.2 and 3.3).

The key application of the kinetic analysis to the sm-FRET datasets was to carry out simulations using the fitting parameters, derived in Fig. 3.13, in order to make predictions of the impact of seeding with either high-FRET oligomers or small fibrils. These results have been described in detail in Iljina & Garcia *et. al.* 2016.[83] Several key conclusions have been made as a result of these simulations. Both high-FRET oligomers and small fibrils were found to be effective at seeding. The impact of seeding was found to vary not only depending on the nature of the seeds, but also on the initial αS monomer concentration; and to be ineffective below 10 nM of starting αS and particularly prominent at the concentrations above 1 μM.

Furthermore, to assess the role of seeds in αS aggregation at more physiologically-related conditions, the numbers of oligomers or fibrils were predicted that would need to be introduced to a volume approximately corresponding to a single cell $(10\ \mu m)^3$ in order to double the aggregation rate in the presence of a set of chosen initial concentrations of αS, which include the range of reported *in vivo* concentrations of αS[161,162]. Following these predictions, if the monomer concentration is 2 μM, 10,000 fibrils were found to be required, or 16,000 high-FRET oligomers, and an approximately five times higher (9.4 μM) concentration of αS monomer would be needed for the production of this number of oligomers. These requirements for the templated seeding of αS are relatively high in comparison to, for example, recently reported results for tau k18 using a similar approach[159].

These resulting high requirements for the templated seeding by αS were subsequently linked to its potential role as a prion-like protein. The processes of templated seeding and prion-like spreading have been closely related in literature, and prion-like behaviour has been frequently assigned to αS, as has been detailed in section 3.1 of this chapter. Because the templated seeding in these simulations was found to be effective only in the presence of very high numbers of aggregates, it was hypothesised that this process is unlikely to be the main driving force behind the spreading of αS aggregates *in vivo*, where the presence of such high numbers of aggregates is unlikely to be common. Furthermore, using the same oligomer preparations as for the sm-FRET experiments, it was determined that only around 50 pM of oligomers are required in order to produce detectable release of reactive oxygen species, if the oligomeric solutions are applied to mixed neuronal cultures (as detailed in Iljina & Garcia *et. al*., 2016). This concentration, determined by the sm-FRET analysis, corresponds to 30 oligomers per volume of a single cell, $(10\ \mu m)^3$. The resulting number is much lower than the tens of thousands of oligomers that were determined to be required for the efficient templated seeding of αS. This difference suggests that the oligomers of αS have a higher propensity to cause cellular damage than to template the aggregation of monomeric αS. It was therefore hypothesised that the spreading may occur by an alternative cell-driven mechanism that does not strongly depend on the seeding effectiveness. In this mechanism, schematically illustrated in Fig. 3.14, the primary role of αS aggregates upon entering a cell is not to induce the aggregation of endogenous monomeric αS by templated seeding (Fig. 3.14a), but rather to stress the cell and trigger the production of reactive oxygen species and other compounds that in turn promote the aggregation of monomeric αS (Fig. 3.14b). It would be very interesting to experimentally test whether this mechanism of spreading occurs in cellular environment. If this model inferred from the kinetic analysis is dominant *in vivo*, then reducing cellular stress may be a potentially promising therapeutic strategy to prevent the spreading of αS.

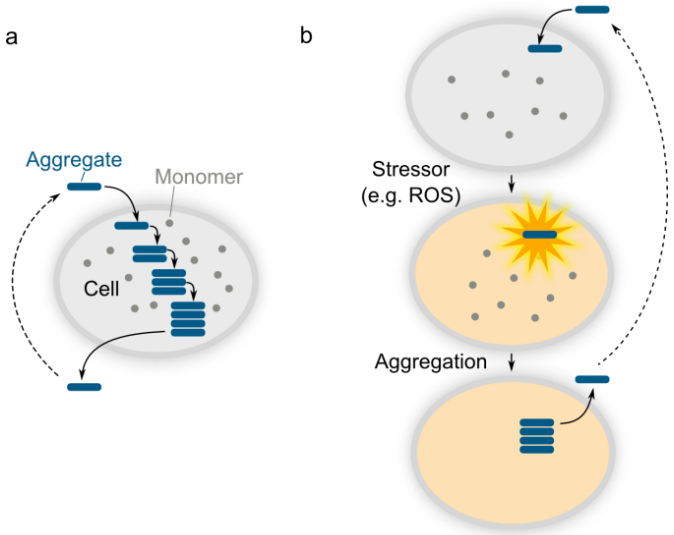

Figure 3.14. Schematic outline of two simplified models of αS aggregate spreading in cellular environment (Figure reproduced from Iljina & Garcia *et. al*., 2016[83]). **a.** Aggregate-driven, or prion-like, propagation of aggregated species. The primary role of the aggregate upon entering a cell is to induce the aggregation of monomeric protein by the mechanism of templated seeding. **b.** Cell-driven model. The initial role of the aggregate is to induce cellular stress, which disrupts the homeostasis and creates conditions where protein aggregation becomes favourable.

3.4 Summary and conclusions

The αS aggregates of αS are observed to spread during the disease both in human brain and in various disease models such as transgenic mice and cultured cells. Furthermore, αS is known to undergo a process of templated seeding, whereby added pre-formed aggregates of αS result in the accelerated aggregation of monomeric αS. In this chapter, the aggregation of αS was studied by sm-FRET under a range of starting monomer concentrations of 0.5-140 μM. Initially, sm-FRET experiments were optimised in order to select the conditions that would allow studying the oligomerisation process. Fluorescently-labelled αS used for the measurements was confirmed to form fibrils over a comparable timescale to the unlabelled protein. Oligomer formation was found to be most efficient under shaking conditions. The presence of hydrophobic coating on the walls of the test-tubes was found important for preventing oligomer adhesion during incubation. Optimum detection time in sm-FRET experiments was selected to minimise the effects of protein sticking or oligomer dissociation during the single-molecule measurements. The potential contribution from fibrillar aggregates to the measurements was assessed.

Following the optimisation, the kinetics of αS oligomerisation at 0.5-140 μM was studied. The results showed that the highest oligomer concentrations were generated at the highest starting protein concentrations. In addition, differences in the generated oligomer sub-populations were observed.

Two αS oligomer types, low-FRET and high-FRET oligomers that were previously identified by sm-FRET method in this laboratory, were clearly distinguishable at the starting αS concentration of 35 μM and above. The formation of the most compact oligomer type, the high-FRET oligomer, was not detectable at the lowest starting concentrations, 0.5 μM. The apparent size distributions of oligomeric species were estimated using both confocal sm-FRET technique in solution, and TIRFM imaging of surface-immobilised oligomers. The apparent size distributions of oligomers were found to peak at sizes below 10-mers by both methods, and the limitations of the methods used for oligomer size estimation were discussed. Subsequently, the results of theoretical analysis were presented. The kinetic model, developed and applied to the sm-FRET data by Dr. G. Garcia, considered oligomers as the intermediates on the pathway to fibril formation. This model was able to successfully fit the kinetic profiles at the full concentration range. Following the fitting, the numbers of αS aggregates that would be required for effective seeding were predicted. These predictions resulted in very high numbers in the order of 10^4 of aggregates. Based on these identified high requirements for seeding and a broad literature evidence of αS spreading, a cell-driven mechanism of αS spreading was proposed, where the primary role of αS aggregates is to stress cells, that ultimately triggers αS aggregation.

Chapter 4
Aggregation of αS in the presence of nanobodies

In this chapter, the aggregation of αS in the presence of two αS-specific antibodies, NbSyn2 and NbSyn87, was studied by sm-FRET. The effect of the Nb binding on the formation and the properties of oligomers of αS was investigated.

4.1 Introduction

Owing to the central role of protein aggregation in diseases such as PD, potential drug targets have been actively investigated[163], including reagents that are designed to bind to amyloidogenic proteins and inhibit their aggregation. Two commonly exploited strategies are active and passive immunization[164]. Active immunization uses an animal's immune system to generate antibodies upon administration of aggregation-prone proteins such as αS, whereas passive immunisation involves the delivery of antibodies.

Antibodies are large molecules composed of two heavy chains and two light chains, held together by disulfide bridges[165]. In the early nineties, antibodies that were composed of heavy chain dimers and lacked light chains were discovered to be naturally produced by the immune system of camelids[166]. Subsequently, their small and highly stable single-domain fragments, termed "nanobodies" (Nbs), were generated[167]. Nbs are small recombinant intact binding domains, which are approximately one quarter the size of camelid-derived antibodies (Fig. 4.1). A nanomolar-affinity binding of Nbs was found to inhibit the *in vitro* aggregation of proteins such as human lysozyme, beta-2-microglobulin, prion protein and amyloid-beta[168], enabling their use as valuable tools in the studies of protein aggregation. Moreover, the ability of Nbs to alter the conformations of target proteins in living cells was demonstrated[169]. In addition, Nbs raised against prion protein were shown to be able to cross the blood-brain barrier[170], making them potentially attractive in the context of protein-deposition diseases. Recently, two Nbs, NbSyn2[171] and NbSyn87[172] were developed, that bind to distinctive epitopes within the C-terminal domain of αS (residues 137-140 and 118-131) (Fig. 4.1). Even though these Nbs were raised against monomeric αS, they recognised the fibrils of αS because C-terminal region is exposed in amyloid fibrils[24]. This enabled their use as biophysical probes to study αS fibril maturation[172]. Subsequently, their effects on the conformations of monomeric αS were explored[173]. In addition, it is known from previous *in vitro* studies that the C-terminal part of αS is exposed in oligomers[174], making the Nbs directed at this region of αS good candidates for the studies of αS oligomerisation.

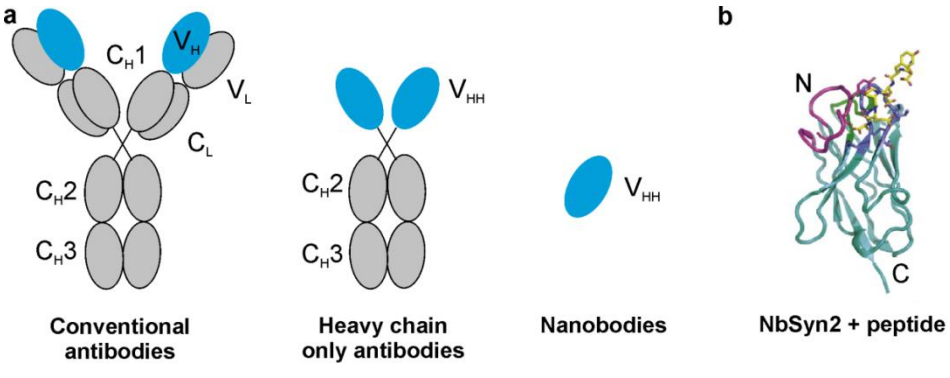

c

NbSyn87 QVQLQESGGGSVQTGGSLRLSCVASGY--SGY-MAWFRQAPGKEREGIAAIYR-GDKITYY
AHSVQGRFTISQANAKNTVYLLMNSLKPEDTAIYYCAA
RRVVADSPLLSKTYAYWGQGTQVTVSSHHHHHH

NbSyn2 QGQLVESGGGSVQAGGSLRLSCAASGIDSSSYCMGWFRQRPGKEREGVARINGLGGVKT
AYADSVKDRFTISRDNAENTVYLQMNSLKPEDTAIYYC
AAKFSPGYCGGSWSNFGYWGQGTQVTVSSHHHHHH

Figure 4.1. The structure and primary sequence of nanobodies **a.** Schematic representation of the relation between conventional antibodies, heavy-chain antibodies and nanobodies. Constant heavy domains are indicated with C, and variable domains (either heavy or light) with V. **b.** 3-dimensional representation of the crystal structure of NbSyn2 in complex with a peptide corresponding to the residues 132-140 of αS molecule, comprising a part of the binding epitope. N- and C- terminal regions of NbSyn2 are indicated. (From De Genst *et. al.*, 2010[171]). **c.** The primary sequences of NbSyn87 and NbSyn2, with binding epitopes highlighted in red (From Guilliams *et. al.*, 2013[172]).

4.2 Methods

4.2.1 Expression and purification of Nbs

Nbs used in this work were expressed and purified by Dr. E. De Genst. NbSyn87, NbSyn2 and a lysozyme-specific nanobody NbHul5g were expressed in the periplasm of *E. coli* and purified using immobilized metal affinity chromatography and size-exclusion chromatography as previously described[171].

4.2.2 Estimation of the concentration of free αS

This was estimated as the difference between the starting total concentration of αS and the concentration of bound αS in the presence of Nbs, calculated according to the following equation, based on the law of mass action[175] (see Appendix 2 for derivation):

$$[aS]_{bound} = \frac{1}{2}\left([aS] + [Nb] + K_d - \sqrt{([aS] + [Nb] + K_d)^2 - 4[aS][Nb]}\right) \quad (4.1)$$

where $[aS]_{bound}$ is the concentration of bound αS, $[aS]$ and $[Nb]$ are the starting concentrations of αS and Nb, 70 μM and 140 μM, respectively, and K_d is the corresponding dissociation constant[172].

4.2.3 Sm-FRET experiments

The experiments and data analysis were carried out according to the protocols described in General methods (sections 2.6-2.10). For the aggregation reactions, equimolar concentrations of AF488 and AF594-labelled A90C αS were combined in PBS buffer (10 mM phosphate, 0.27 mM KCl and 137 mM NaCl, pH 7.4) to a final volume of 300 μL, bringing the total αS concentration to 70 μM, either in the presence or in the absence of 140 μM of unlabelled NbSyn87, NbSyn2 or NbHul5g.

4.2.4 TEM Imaging

Imaging was performed according to the protocol in General methods, section 2.14. Since PBS buffer used for the sample preparation lead to the precipitation of negative stain, PBS buffer was exchanged for Tris (25 mM Tris, 0.1 M NaCl, pH 7.4) using spin filters with molecular cutoff of 5 kDa (Sartonis).

4.2.5 Proteinase-K digestion assays

To confirm the structural differences of αS oligomers generated in the presence of αS-specific Nbs to the oligomers formed in the presence of the non-specific NbHul5g, their susceptibility to PK digestion was measured. The sample preparation was the same as for sm-FRET kinetic measurements, and solutions contained a 1:1 dual-labelled mixture of αS (70 μM) with two equivalents of unlabelled Nbs. PK aliquots were prepared in PBS buffer of the same composition as in all previous experiments, with the addition of 1 mM $CaCl_2$, and stored at -80°C before use. Protein samples after 29-h incubation under the same conditions as in previous experiments were diluted into a range of PK concentrations between 0-10 μg ml^{-1} in PBS buffer with 1 mM $CaCl_2$. The total protein concentration during incubations with PK was 280 nM of αS and 560 nM of Nbs. Note that even though only fluorescently labelled αS was detected in this experiment and unlabelled Nbs remained undetected,

both αS and Nbs were expected to be susceptible to the digestion by PK. Therefore, αS samples in the absence of Nbs were not measured to ensure consistent comparison between the same starting total protein concentrations. The samples were incubated at 37°C for 10 min, and subsequently further diluted (up to 280 pM of αS) prior to analysis by sm-FRET. The results were presented as fractions of degradation against PK concentrations.

4.2.6 Nanobody labelling with AF dyes

Random lysine labelling was performed using N-hydroxysuccinimide (NHS) linked AF647 or AF488. 1.5 molar equivalents of AF647 (or AF488) NHS ester (Life Technologies) were added to unlabelled Nb solution in 100 mM sodium bicarbonate buffer (pH 8.3), and incubated with agitation for 3 h. The labelled protein was then separated from free dye using Sephadex G-25 loaded PD-10 desalting columns (GE Healthcare). The labelling efficiency was determined using UV-Vis absorbance measurements, and was above 90% (NanoDrop 2000c UV-Vis Spectrophotometer, Thermo Scientific). The stoichiometry of AF647 labelling of the nanobodies was determined according to the manufacturer's specifications and confirmed by mass-spectrometry and was found to be close to a 1:1 stoichiometry.

4.2.7 TCCD control measurements to confirm the absence of Nb to αS binding in single-molecule measurements

To verify the absence of direct binding between fluorescently-labelled Nbs and fluorescently-labelled αS at single-molecule concentrations, control TCCD experiments were performed. Dual laser excitation with either 488/594 nm or 488/633 nm laser beams (depending on the AF label pairs of the analysed samples) was used, and data acquisition and analysis were as described in General methods, sections 2.11-2.12.

For the measurements, 1:1 stoichiometric ratio of AF-labelled αS and AF-labelled NbSyn87 was used. This Nb was chosen owing to its highest affinity for αS and therefore the highest potential chance for it to remain bound in the single-molecule experiments. The following equimolar combinations were tested: AF647-NbSyn87 + AF488-αS, AF488-NbSyn87 + AF647-αS, AF488-NbSyn87 + AF594-αS. In addition, samples of free AF647 + AF488 and aggregated AF647-αS + AF488-αS were analysed as controls. For the measurements, the samples were diluted either in PBS buffer or deionised water up to single-molecule concentration suitable for TCCD analysis. The dilution into different buffers

served as a test for potential changes in the co-interaction of the Nb and αS due to the changes in pH and ionic strength. To determine Q (eq. 2.1 in General methods) corresponding to a non-interacting system and resulting purely from the chance-coincidence, 1:1 stoichiometric mixture of free AF dyes was analysed by TCCD, keeping the same detection conditions as for the protein measurements. As positive controls, the samples of dual-labelled αS incubated under agitation at 2 μM for 72 h were also recorded. The data were analysed in the same manner as the data recorded using the fluorescently labelled protein samples.

4.2.8 Comparison of average αS monomer fluorescence intensities in the presence or in the absence of unlabelled Nbs

As an additional test to verify that the unlabelled Nbs did not interfere with the fluorescence emission from AF labels on αS, the values of average monomer brightness in sm-FRET measurements were compared across the samples with or without the Nbs, following data collection with the sample dilutions into either PBS or water.

4.3 Results

4.3.1 NbSyn87 and NbSyn2 impede the formation of high-FRET oligomeric species of αS

To monitor the impact of Nbs on the formation of αS oligomers, sm-FRET kinetic experiments were carried out similarly to the experiments described in Chapter 3. The measurements of oligomer formation were chosen to be limited to the first 30 h of aggregation, since it was previously confirmed that the contribution from fibrillar species during this time was negligible (Fig. 3.7).

In these experiments, equimolar mixtures of AF488 labelled αS and AF594 labelled αS were used at the total protein concentration of 70 μM, either in the presence or in the absence of 140 μM of unlabelled Nbs. From the dissociation constants of NbSyn2 and NbSyn87 for monomeric αS, respectively ~264 nM and ~42 nM[172] at 37°C, it was calculated (eq. 4.1 in Methods) that under these conditions the free αS concentration is ~260 nM and ~40 nM, approximating full saturation of all binding sites (i.e. 99.7% for NbSyn2 and 99.95% for NbSyn87). The solutions were incubated with agitation under the same conditions as in the experiments in Chapter 3, and subsequently diluted 10^5-fold to generate appropriate conditions for single-molecule detection, and analysed using sm-FRET.

The solutions were recorded either following their dilution into aqueous buffer of the same composition as what was used for the incubations (PBS, defined in Methods), or following sample dilutions into deionised water, because it was recently found in this laboratory that dilution into low ionic strength solutions enabled a better separation of the low- and high-FRET oligomer types[115].

The average brightness of AF-labelled αS in the presence of the unlabelled Nbs was determined in order to verify that they did not affect the fluorescence properties of the dyes in the sm-FRET experiments. The resulting average AF488-αS monomer intensities selected above the threshold of 15 photons bin^{-1} are listed in Table 4.1. The values are all comparable, confirming the absence of alteration of fluorescence intensity values in the presence of Nbs. Furthermore, control TCCD experiments using AF-labelled Nbs and αS were performed to confirm that the Nbs were fully unbound from αS during the detection under both solution conditions, consistent with their previously reported K_d values[172]. The results of these control experiments are summarised in Table 4.2, listing the derived association quotients, Q, (eq. 2.1. in General methods). In all cases, the Q values for NbSyn87 + αS samples were comparable to the values obtained for the free dyes in solution, and lower than the Q value for aggregated αS. Therefore, based on these control experiments, it can be concluded that Nbs were fully unbound from αS during the detection.

Table 4.1. Average AF488-labelled αS monomer intensity above the threshold of 15 photons bin^{-1}, as determined from sm-FRET measurements ($N_{molecules}$ = 185,584).

Sample type	αS		αS + NbHul5g		αS + NbSyn2		αS + NbSyn87	
	PBS	**H_2O**	**PBS**	**H_2O**	**PBS**	**H_2O**	**PBS**	**H_2O**
Mean intensity (photons bin^{-1})	19.4	19.2	19.2	19.0	19.3	19.1	19.2	19.4

Table 4.2. Summary of %Q values (eq. 2.1), resulting from TCCD control experiments using 1:1 stoichiometric ratio of fluorescently labelled NbSyn87 and αS. Free dyes are measured as a negative control, and aggregated (for 72 h) dual-labelled αS as a positive control. Buffers used for the dilutions are specified.

	Free AF488 + AF647	αS, 2 μM	AF647-NbSyn87 + AF488-αS		AF488-NbSyn87 + AF647-αS		AF488-NbSyn87 + AF594-αS
%Q	**PBS**	**PBS**	**PBS**	**H_2O**	**PBS**	**H_2O**	**PBS**
	0.025 ± 0.030	0.917 ± 0.291	0.093 ± 0.13	0.094 ± 0.001	0.012 ± 0.029	0.051 ± 0.051	0.021 ± 0.010

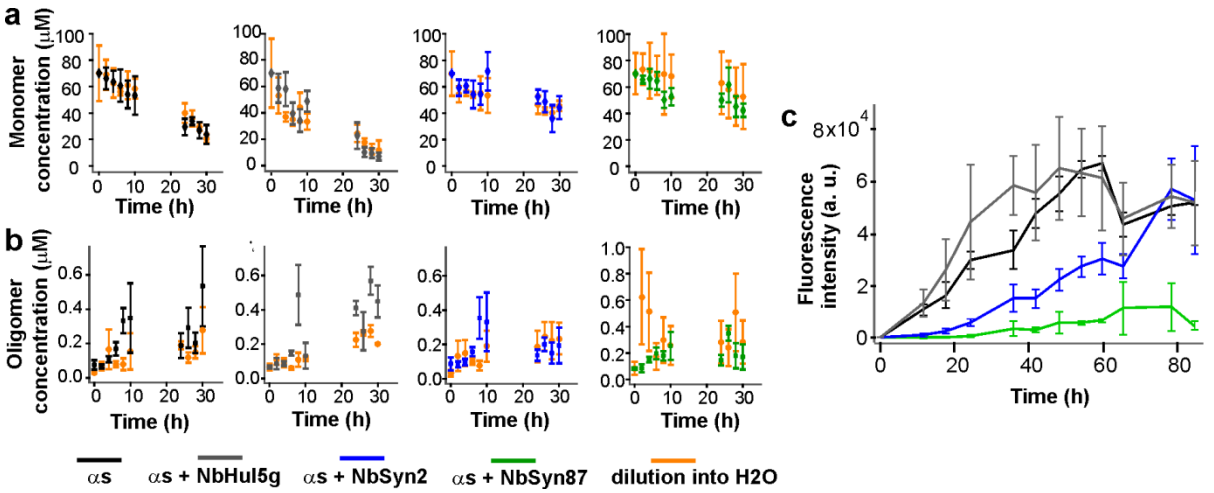

Figure 4.2. Aggregation kinetics of αS at 70 μM in the presence of 140 μM Nbs, studied by sm-FRET. **a.** Monomer depletion profiles (n=6, sem). **b.** Total oligomer concentrations (n=3, sem). **c.** Bulk ThT assays carried out (by Dr. E. De Genst) under the same incubation conditions as the sm-FRET assays, using 70 μM wt αS, either alone or in the presence of 140 μM Nbs (n=3, std).

Subsequently, the kinetic profiles of αS aggregation in the presence or in the absence of the Nbs were recorded by sm-FRET. The resulting kinetic profiles of monomer depletion and oligomer formation by αS are shown in Fig. 4.2.

The most rapid decrease in the monomer concentration, deduced from the monomer burst-rates (as detailed in General methods, section 2.9.) occurred in the samples containing 70-μM αS alone or in the presence of control NbHul5g, and was attributed to the formation of αS fibrils. Samples containing NbSyn2 and NbSyn87, however, showed slower monomer depletion. TEM images of the samples after prolonged incubation confirmed the presence of abundant amyloid fibrils in the solutions containing αS alone or in the presence of NbHul5g and NbSyn2, while only oligomers and short protofibrils could be detected in the presence of NbSyn87 (Fig. 4.3).

The kinetic profiles of oligomer formation were comparable across all samples and dilution conditions, suggesting that the αS-specific Nbs did not reduce the overall numbers of αS oligomers (Fig. 4.2b). However, the inspection of individual FRET efficiency histograms of the samples recorded upon dilution into water revealed clear differences between the control samples and the samples containing αS-specific NbSyn2 and NbSyn87 (Fig. 4.4).

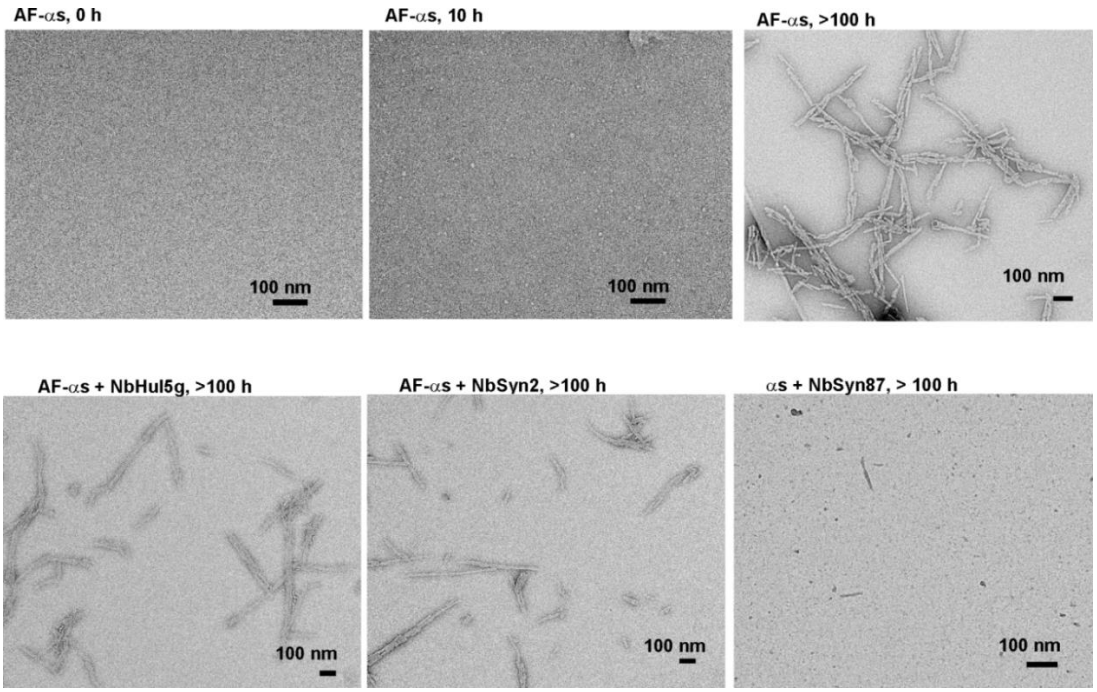

Figure 4.3. TEM images of aggregates formed in 1:1 AF488:AF594 dual-labelled αS solutions (70 μM). Top: labelled αS solutions at different time-points during the aggregation reaction with agitation. Bottom: αS solutions in the presence of 140 μM of unlabelled NbHul5g, NbSyn2 and NbSyn87 after >100 h incubation with agitation. Large amyloid fibrils and fibrillar fragments were observed in all samples at this time, except in the presence of NbSyn87, where short protofibrils were present along with round-shaped oligomeric aggregates.

As previously (Chapter 3), the FRET efficiency histograms were split into two groups, corresponding to the histograms derived from small oligomers containing 2-5-mers and large oligomers comprising 6-150-mers. This splitting allowed to identify the time-dependent changes more easily, which were most clearly observed in the histograms of large oligomers during aggregation, and were less visible for those of small oligomers due to low photon counts, as was illustrated in Fig. 3.10.

For the samples of αS-only and αS in the presence of control NbHul5g, two peaks could be observed in the FRET efficiency histograms of large oligomers (Fig. 4.4.), corresponding to the two previously discussed oligomer populations (section 3.1.4). Low-FRET oligomers were characterised by the population centred at an average FRET efficiency value (E) of 0.4, and high-FRET oligomers were indicated by a peak centred at E value of around 0.8 (Fig. 4.4). The high-FRET population was dominant by the end of the second day of incubation, in good agreement with the kinetics of high-FRET oligomer formation by 70-μM solutions of αS, as described in Chapter 3. In contrast, the FRET histograms of oligomers formed in the presence of αS-specific Nbs showed a single broad distribution centred at ~0.6, without a clear distinguishable peak of high-FRET oligomer sub-population. The appearance of these FRET efficiency histograms resembles those that have been obtained for αS solutions at low concentrations (5-10 μM of αS) in which high-FRET oligomers were not formed in

large proportions (Chaper 3). Therefore, the appearance of FRET efficiency histograms could suggest that in the presence of αS-specific Nbs, the formation of high-FRET oligomers was impeded.

To further test this hypothesis, comparative sm-FRET PK digestion assays were carried out (as described in Methods section 4.2.5) using the samples after 29 h of incubation, when the solutions were enriched in high-FRET oligomers. It was previously established that high-FRET oligomers are much more resistant to the digestion by PK enzyme in comparison to low-FRET oligomers[79]. The resulting PK digestion profiles are shown in Fig. 4.5. From this result, the populations of oligomeric species formed in the presence of NbHul5g are more resistant to PK digestion than those formed in the presence of NbSyn2 or NbSyn87. This is consistent with the presence of a higher proportion of high-FRET oligomers in solutions containing NbHul5g compared to the samples containing NbSyn2 and NbSyn87 and supports the hypothesis that NbSyn2 and NbSyn87 inhibit the formation of high-FRET oligomers. To note, the relative minor differences in the profiles derived for the samples aggregated in the presence of αS-specific Nbs (Fig. 4.5) may reflect the differences in the binding affinity of the two Nbs rather than the structural dissimilarity of the αS oligomers, formed in the presence of the αS-specific Nbs. The binding of αS-specific Nbs may protect against αS degradation. Because of the 10-fold difference in the affinities of the two αS-specific Nbs, higher fraction of αS was expected to be bound by NbSyn87 than by NbSyn2 under the PK incubation conditions, hence explaining the resulting higher stability of oligomers formed in the presence of NbSyn87 in comparison to the oligomers formed in the presence of NbSyn2.

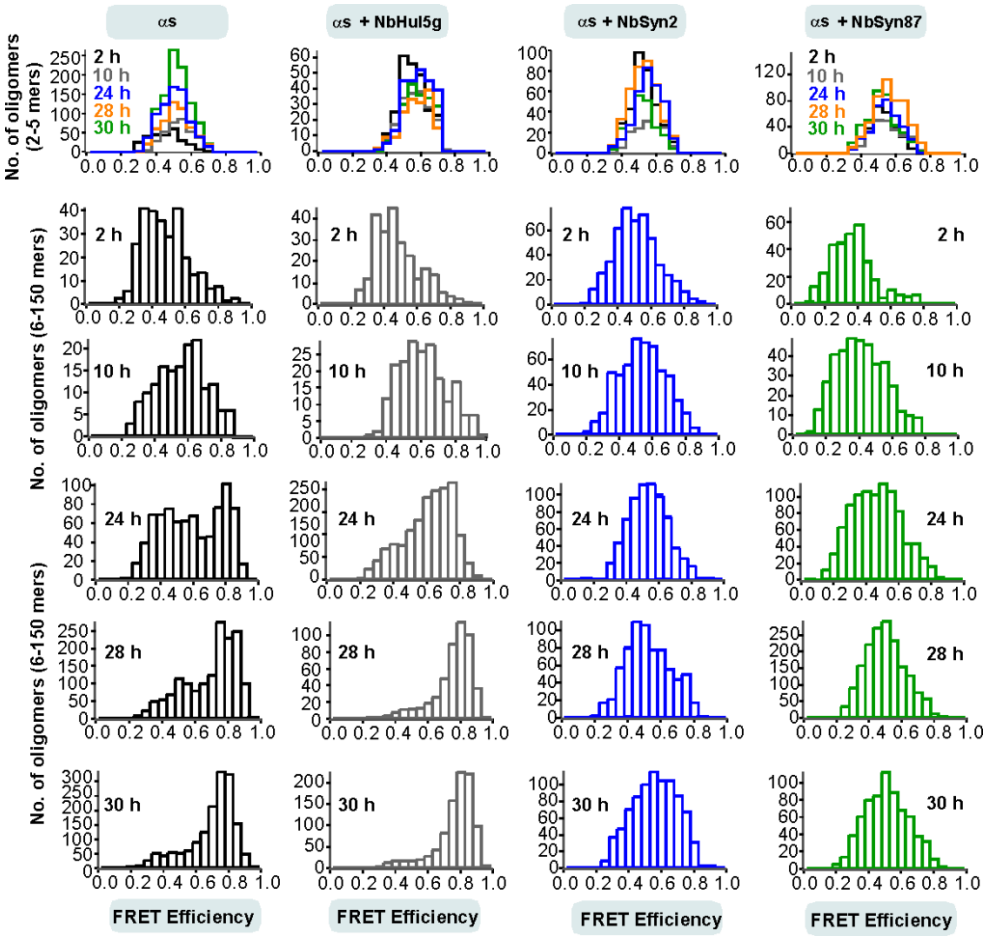

Figure 4.4. Representative FRET efficiency histograms obtained for different time points during first 30 h of αS aggregation, recorded upon dilution into deionised water for the sm-FRET detection. Here, the histograms have been split into two populations of apparent sizes, small (2-5-mers) and large (6-150-mers). For large oligomers, the differences in the FRET efficiency histograms can be observed.

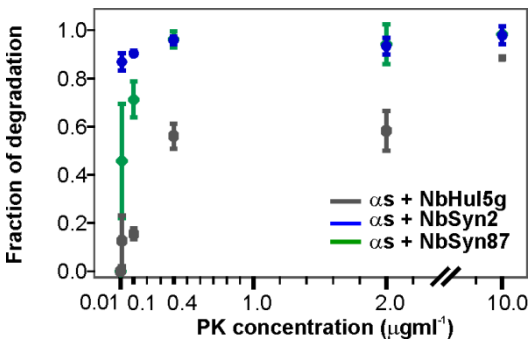

Figure 4.5. Results of comparative sm-FRET PK digestion assays. Fraction of degradation is defined as (number of oligomers in the PK-exposed sample / number of oligomers in the initial sample) (n=3, std). The αS control in the absence of Nbs was not measured for consistency, since it was presumed that PK would act on both the fluorescently-labelled αS and the unlabelled Nbs (see section 4.2.5).

4.3.2 NbSyn87 and NbSyn2 act to rapidly convert high-FRET oligomeric species into low-FRET oligomeric species

Subsequently, it was sought to check whether the αS-specific Nbs could disrupt pre-formed high-FRET oligomers. To this end, solutions from aggregation reactions of 70-μM dual-labelled αS without the Nbs were collected after 29-h incubation and analysed by sm-FRET to confirm the presence of high-FRET oligomers. Then, two equivalents (referring to the total αS concentration) of unlabelled NbSyn2, NbSyn87 or NbHul5g were added to these samples prior to sm-FRET analysis. The representative contour plots of FRET efficiency versus apparent oligomer size, and FRET efficiency histograms are shown in Fig. 4.6, and consistent results were obtained in at least three separate experiments.

The addition of NbSyn2 or NbSyn87 resulted in a decrease of the mean FRET efficiency values (Fig. 4.6b). These changes in FRET efficiencies cannot be explained by optical effects due to the binding of the Nbs to the oligomeric species, which was confirmed by the experimentally observed absence of coincidence between the labelled Nb and αS under the single-molecule detection conditions.

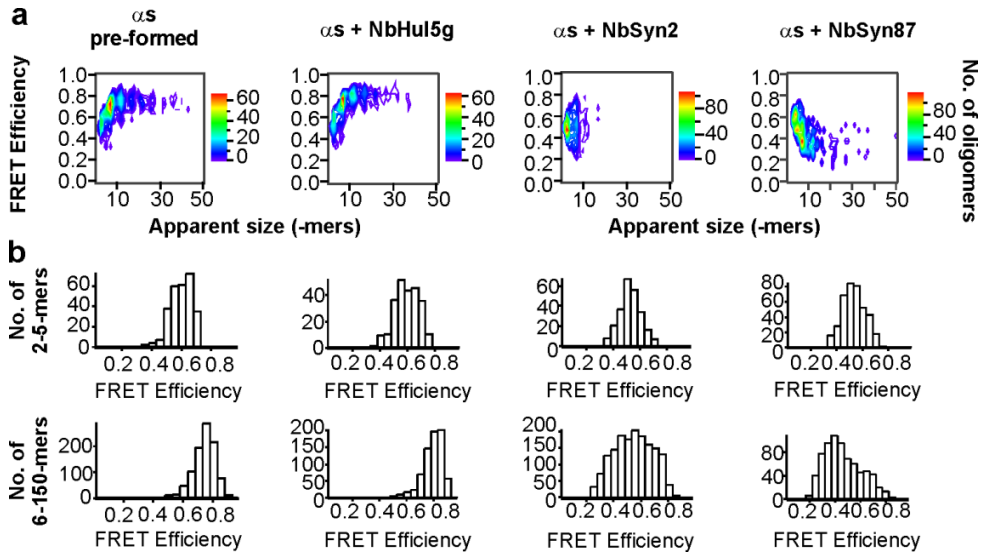

Figure 4.6. Results of sm-FRET measurements after addition of two equivalents of unlabelled Nbs to pre-formed high-FRET oligomers. **a.** Representative contour plots of FRET efficiency versus apparent oligomer size resulting from sm-FRET measurement performed immediately after addition of Nbs to aggregated solutions of αS (after 29 h), containing high-FRET oligomers. **b.** Corresponding FRET efficiency histograms split into two size populations, small (2-5-mers) and large (6-150-mers) oligomers. In the absence of Nbs and upon addition of non-specific NbHul5g, the majority of the detected large oligomeric species yielded FRET efficiency values above 0.6, characteristic of high-FRET oligomers. Upon addition of either NbSyn2 or NbSyn87, the average FRET efficiency distributions shifted to lower values, and this shift was particularly pronounced in the presence of NbSyn87.

The changes in FRET efficiency values following the addition of NbSyn2 or NbSyn87 can therefore be solely attributed to the Nb-induced conformational conversion of the high-FRET oligomers to the less ordered low-FRET oligomers, occuring rapidly after the addition of the Nbs. According to these results, the process was particularly fast in the presence of NbSyn87, occurring within 5 minutes, which was estimated from the length of the incubation time between the addition of the nanobodies and subsequent sm-FRET analysis. To measure the timescale of the conversion process more precisely, a stopped-flow technique would need to be designed that would enable the discrimination between different oligomer types. Alternatively, rapid real-time TIRFM FRET imaging could be used, or cryo-EM imaging of the samples, plunge-frozen rapidly after the addition of nanobodies. The more pronounced effect of NbSyn87 compared to NbSyn2 in this experiment is consistent with its known higher affinity for αS. The oligomers were expected to remain in the altered structure during sm-FRET analysis since the conformational reorganization from low-FRET to high-FRET oligomers needs to overcome a high energy barrier, reflected in the previously determined half-time of several hours[79]. It may be interesting to study the identified Nb-induced conversion in further detail, in particular, to determine whether or not the addition of Nbs can induce the conversion of fibrillar aggregates of αS to their precursor high-FRET and low-FRET oligomers. This may be achieved by performing experiments similar to those described in the present section, but using pre-formed amyloid fibrils rather than high-FRET oligomers and monitoring the conversion process over an extended period of time.

4.4 Summary and conclusions

In this chapter, the effect of two αS-specific nanobodies on its aggregation pathway was studied using sm-FRET. The two nanobodies, NbSyn2 and NbSyn87, are known to recognise the C-terminal part of αS molecule and bind to this region with nanomolar affinity.

The oligomerisation of αS at 70 μM was studied either in the presence or in the absence of two molar equivalents of the Nbs. Initial control experiments indicated that the Nbs were unbound from αS under single-molecule conditions. The kinetic profiles of oligomer formation were found to be similar both in the presence and in the absence of Nbs, suggesting that these antibodies did not decrease the overall numbers of formed oligomers. Interestingly, the kinetics of monomer depletion was found to be slower in the presence of the Nbs than in their absence. In addition, fibril formation was found to be abolished in the presence of NbSyn87, judged by TEM imaging. FRET efficiency distributions of oligomers revealed that in the presence of the Nbs, the formation of high-FRET oligomer type was supressed. Oligomers formed in the presence of the Nbs were found to be more susceptible to PK digestion relative to the oligomers formed in the presence of a control non-specific Nb. It was also

found that pre-formed high-FRET oligomers could undergo a rapid conformational conversion to low-FRET oligomers upon the addition of excess Nbs.

These experimental results are consistent with an impact of NbSyn2 and NbSyn87 on the early conformation conversion between low-FRET and high-FRET oligomers taking place prior to fibril formation. This action leads to the destabilisation of high-FRET oligomers and the shift of the total oligomer population to low-FRET species, which ultimately results in the inhibition of fibril formation, particularly in the presence of NbSyn87.

Chapter 5
Aggregation of αS in the presence of arachidonic acid

In this chapter, fatty acid-induced oligomerisation of αS is characterised at the single-molecule level. The resulting species are compared to the oligomers of αS formed in aqueous buffer in a set of sm-FRET assays to reveal a lower stability of the fatty-acid induced species.

5.1 Introduction

While αS is the main component of the solid pathogenic deposits in PD and DLB brains, lipids have been found to be co-localized with αS in the brain-stem LBs[176] and cortical LBs[177]. αS is localized to presynaptic nerve terminals in close proximity to synaptic vesicles[43,44], and is involved in the transmission of vesicular cargo[47], as well as in vesicle trafficking and retrieval[39]. These processes occur via phospholipid membrane-based mechanisms[178-181], implying a direct connection between the normal physiological function of αS with phospholipids and fatty acids (FAs). Furthermore, αS shares structural homology with the family of FA-binding proteins and was shown to bind FAs in a dose-dependent fashion[182]. Soluble oligomers of αS have been identified in the cytosols of PD and DLB human brains, and their detection was enhanced by delipidation, suggesting that oligomers are complexed with lipids and FAs *in vivo*[183]. Other *in vivo* observations additionally support the interplay between αS and FAs. For example, dietary intake of polyunsaturated FAs resulted in a substantial increase in αS gene expression in rats[184,185]. In addition, αS oligomerisation and neuronal injury in mice were detected as a consequence of FA dietary intake[186]. Moreover, a significant increase in the cytosolic levels of polyunsaturated FAs along with αS oligomer accumulation were observed in PD human brains[187].

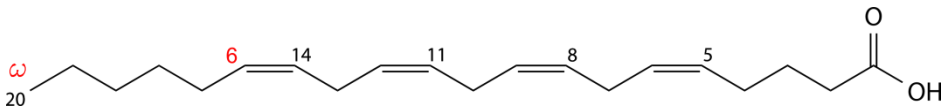

Figure 5.1. Chemical structure of arachidonic acid. It belongs to the class of omega-6 fatty acids, since its first double bond is located at the sixth carbon starting from the omega end (shown in red).

Arachidonic acid (ARA) is an unsaturated FA (Fig. 5.1) and is one of the most abundant FAs in grey matter phospholipids of human brain[188]. ARA is continuously released from the phospholipid membranes into endocrine cells and neurons by the action of enzymes[189], and has very diverse functions *in vivo*. Its content is elevated in conjunction with inflammatory response caused by noxious substances[190], stimulation of certain receptors[191], during traumatic brain injury[192,193], and ARA is a precursor to pro-inflammatory substances termed eicosanoids[194]. Increased concentration of free ARA was shown to lead to the elevation of metal ion concentration in neurons, which caused apoptosis, and therefore ARA was referred to as a 'death pore opener'[195]. On the other hand, ARA is constructively involved in the action of numerous other ion channels (reviewed in Meves, 2008)[196]. In addition, it activates a plasma membrane protein syntaxin, which is critical to the growth and regeneration of neuronal cells[197,198]. It also takes part in the enhancement of the formation of SNARE protein complex[198] which drives cell exocytosis. Furthermore, ARA facilitates neurotransmission and was proposed to act as a retrograde messenger in the process of long-term potentiation[199], although this remains controversial[200]. In addition, the presence of ARA has been discovered to mediate a short-term increase in the neurotransmitter release at synapses in vertebrates, confirming its involvement in synaptic plasticity[201].

Multiple *in vitro* studies have demonstrated that ARA was able to promote the self-assembly of αS, leading to the formation of either oligomeric or fibrillar aggregates, depending on the acid to protein ratios[11,183,202,203]. Initially, the effect was shown only with ARA present at 1 mM concentration in solution[202], which is above its critical micelle concentration (CMC), measured to be 60 μM[203,204]. Subsequently, the promotion of αS aggregation in the presence of ARA was reported at lower concentrations of ARA[11,203], including 10 μM concentration[183]. Interestingly, a rapid change of αS from unstructured to alpha-helical conformation in the presence of ARA was observed[203], implying a rapid interaction between monomeric αS and ARA. In addition, a shift in the CMC of ARA from 60 μM to 100 μM was observed, and proposed to be due to the dispersion of ARA micelles by the direct binding of αS to the FA[203]. These observations imply a possibility that the FA itself is a constituent of the formed aggregates, although this remains to be confirmed experimentally. In addition, the reported sodium dodecyl sulfate-resistance and the stability of the ARA-induced aggregates of αS upon boiling, chromatographic procedures and addition of denaturants[202] suggests a possibility that these species may be cross-linked, which also requires verification. Despite the increasing focus on the oligomers of αS as the key cytotoxic species in the disease[21,76,205], and the numerous observations of the ARA-induced oligomer formation in the presence of the excess of ARA, it is not entirely clear whether these aggregates differ from the oligomers of αS that are formed in the absence of the FA, owing to the challenges in characterising large numbers of either species due to their low concentrations in solutions and limited methods for their comparison.

5.2 Methods

5.2.1 ARA solution preparation

ARA (Sigma Aldrich) was stored under nitrogen at -80°C, and aqueous stock solutions were freshly prepared prior to all experiments by adding the pure FA to ice-cold buffer (25 mM Tris, 0.2 M NaCl) followed by vigorous agitation.

5.2.2 αS aggregation

For the preparation of αS oligomers in the absence of ARA, protein solution was made, containing 1:1 stoichiometric ratios of AF488- and AF594-labelled αS in Tris buffer (25 mM Tris, 0.1 M NaCl, 0.01% NaN_3, pH 7.4), and a total protein concentration of 35 μM unless stated otherwise. The aggregation mixture was incubated in the dark over 24 h at 37°C with constant shaking at 200 r.p.m. (New Brunswick Scientific Innova 43, 25 mm orbital diameter), and subsequently centrifuged for 15 min at 12,800 x g and separated from fibrillar pellet.

For the preparations of ARA-induced oligomers of αS, an aggregation mixture contained 1:1 ratio of AF488- and AF594-labelled αS, with the total αS concentration of 35 μM, and 1 mM concentration of ARA, combined in Tris buffer (25 mM Tris, 0.1 M NaCl, 0.01% NaN_3, pH 7.4). The mixture was incubated in the dark over 24 h at 37°C without agitation.

5.2.3 sm-FRET measurements and data analysis

Single-molecule confocal setup, the experimental procedure and data analysis were carried out according to the protocols described in the General Methods chapter, sections 2.5-2.10.

5.2.4 Preparation of fluorescently labelled duplexes for control measurements

DNA duplexes dual-labelled with AF dyes were used. For the preparation of the DNA duplexes, synthetic complementary pairs of oligonucleotides were purchased from ATDBio, and were purified by the supplier by double HPLC. The dual-labelled duplexes were formed by heating a 1:1 mixture of

either TCCD olig 1 and 2, or FRET olig 1 and 2 (the primary sequences of the oligonucleotides are included in section 5.3.3.) at a total concentration of 1 μM to 95°C, and slowly cooling to room temperature. The duplexes were diluted to single-molecule concentrations into Tris buffer of the same composition as used for the aggregation preparations, either in the presence or in the absence of ARA.

5.2.5 CD measurements

Circular dichroism (CD) measurements presented in Fig. 5.2c were carried out with the assistance of Dr. L. Tosatto. For experiments in Fig. 5.2c, samples were prepared in the same way as for the sm-FRET experiments, using AF594-labelled αS, and diluted into Tris buffer to the final protein concentrations of 3-10 μM prior to the measurements. Spectra were recorded on Jasco J-810 spectropolarimeter, using a quarz cuvette of 1 mm path length. The spectra were acquired between 205 and 250 nm, with an interval of 0.2 nm, and an average of 10 accumulations per spectrum, using 1 nm bandwidth and a scanning speed of 50 nm min^{-1}. The spectra were corrected for the background from the buffer in the case of αS in buffer samples, and for the background from the buffer with ARA, for the samples containing ARA. FFT smoothing with a window of 25 datapoints was applied (Origin 7.0), and the resulting spectra were presented as millidergees versus wavelength. For experiments in Fig. 5.9d, samples containing 2 μM αS (1:1 AF488-αS and AF594-αS) and 10 μM ARA at a total volume of 300 μL were incubated for 24 h under the same conditions as before. Subsequently, 10 samples (3 mL) were combined and centrifuged in a filter device with a molecular cut-off of 100 kDa (Amicon Ultra, Millipore). It was expected that some of the ARA-induced oligomers would remain on top of the filter resulting in the multimer-enriched sample. The spectra of both flow-through and the solution remaining on the filter were acquired using the same spectrometer and settings as before, between 200 and 250 nm, with 20 accumulations per spectrum. The spectra were corrected for the background from buffer. No additional smoothing was applied, and the results were expressed as millidegrees versus wavelength. For the measurement in Fig. 5.8c (of the samples washed with buffer to remove excess ARA), the protein concentration was 4 μM, the spectrum was recorded using identical settings as above, with 20 accumulations per spectrum, and the spectrum of buffer was subtracted from the spectrum of the sample.

5.2.6 Oligomer stability at different ionic strengths

It was recently demonstrated using the sm-FRET method that αS oligomers had differential stabilities depending on the ionic strength of buffer solutions[115]. To compare the stability of the ARA-induced oligomers and αS oligomers formed in pure buffer with respect to the changes in ionic strength, the samples after 24 h of incubation were diluted 1:100,000 into either Tris, Tris/2 (Tris buffer diluted with an equal volume of deionised water), Tris/4, Tris/8 and Tris/16, and analysed by sm-FRET immediately after dilution (Fig. 5.7c).

5.2.7 Proteasome degradation assays

Mammalian 26S proteasomes (expressed and purified by Dr. Y. Ye) were purified from HEK293T cells overexpressing rpn11-His-TEV-biotin acceptor sequence (kind gift from Lan Huang, UC Irvine) and purified using established protocols[206,207]. Cells were grown until 100% confluent and collected and resuspended with a scraper in ice-cold Proteasome buffer (50 mM Tris, pH 7.5, 0.5% NP-40, 10% glycerol, 5 mM ATP, 1 mM DTT, 5 mM $MgCl_2$). Dounce homogenizer was then used for cell lysis and the lysate was cleared by centrifugation at 3,000 × g for 5 min at 4°C. This lysate was subsequently incubated with 2 ml bed volume of NeutrAvidin beads (Pierce) at 4°C overnight. Unbound proteins were washed off with 20 ml proteasome buffer and bound proteasomes were cleaved off the column with 6 µl of TEV protease (Invitrogen). Proteasomes were concentrated to >2 µM and frozen in aliquots for single use. For the comparison between the ARA-induced oligomers and αS oligomers formed in pure Tris buffer with respect to their stability towards degradation by 26S proteasome, samples containing 35 µM αS in buffer, or 35 µM αS plus 1 mM ARA after 24 h of incubation were diluted 1:3.75 for proteasomal degradation. The final assay contained 40 nM proteasome, 125 mM ATP.$MgCl_2$, 5 µM creatine kinase and 0.1 M creatine phosphatase in 50 mM Tris buffer (pH 7.4). The resulting samples were analysed by sm-FRET both immediately after mixing, and after incubation for 12 h under quiescent conditions at 37°C. The fractions of non-degraded oligomers were determined as the numbers of oligomers after the incubation with the proteasome divided by the numbers of oligomers immediately after mixing (Fig. 5.7d).

5.2.8 Oligomer disaggregation upon dilution

To further compare the stabilities of ARA-induced oligomers and oligomers of αS formed in pure buffer, both types of samples after 24 h of incubation were diluted 1:100,000 into Tris buffer of the same composition as for the aggregations, incubated at quiescent conditions at ambient temperature in low-binding test-tubes (Protein LoBind, Eppendorf), and regular aliquots were analysed by sm-FRET over 7 h after dilution, ensuring that the aliquots were withdrawn for the analysis at the same incubation time for either type of samples, to allow a comparison of the disaggregation reactions (Fig. 5.7e). The same experiment was carried out using ARA-induced oligomers prepared at 2 μM αS and 10 μM ARA, and compared with the disaggregation profiles of the ARA-induced oligomers generated at high concentration, as show in Fig. 5.9e.

5.2.9 Proteinase-K digestion assays

To carry out further structural comparison between the ARA-induced oligomers and αS oligomers formed in pure Tris buffer, their susceptibility to PK digestion was investigated (Fig. 5.7f). β-sheet structure, present in fibrils and high-FRET oligomers, is resistant to PK digestion, as was shown in previous works[79]. PK aliquots were prepared in Tris buffer defined above, with the addition of 1 mM $CaCl_2$, and stored at -80°C before use. Samples after 24 h incubation were diluted into a range of PK concentrations between 0-10 μg ml^{-1} in Tris buffer with 1 mM $CaCl_2$, incubated at 37°C for 5 min, and subsequently further diluted for sm-FRET analysis.

5.2.10 Depletion of ARA concentration

ARA-induced oligomers were prepared as described above, and subsequently the concentration of free ARA was decreased by washing with copious amounts of buffer, and the protein was concentrated using a spin filter with a molecular cutoff of 5 kDa (Sartorius). Based on the total volume of buffer used for washing in this experiment, the concentration of ARA would be reduced to less than 500 nM. Note that this estimation is a lower bound and does not account for the ARA binding to αS. This preparation is referred to as "ARA washed" in Fig. 5.8.

5.2.11 Comparison of ARA-induced multimerisation using pathological mutants of αS

In order to investigate whether the formation of ARA-induced oligomers could be observed at low physiologically-related concentrations when using pathological mutants of αS, dual-labelled A90C αS was used, and dual-labelled A30PA90C, A53TA90C and E46KA90C αS variants, denoted as A30P*, A53T* and E46K* in Fig. 5.9f, where '*' indicates that these isoforms carry the A90C mutation for the fluorophore incorporation in addition to the disease-associated mutation. The pathological mutants were expressed and purified by Dr. L. Tosatto as previously described in detail[141]. Samples of 2 μM αS of every isoform in the presence of 10 μM ARA, or in its absence (6 separate samples in each case) were prepared and incubated at 37°C without shaking for >30 h to allow steady-state aggregate populations, and subsequently analysed by sm-FRET, keeping the protein concentration for the detection the same for all samples, as judged by comparing the monomer burst rates. Numbers of the detected aggregates were compared (Fig. 5.9f).

5.3 Results

5.3.1 The presence of ARA results in rapid oligomer formation by αS

The self-assembly of αS was monitored in solutions of 35 μM αS in the presence of 1 mM concentration of ARA, above CMC of the FA[203,204]. The samples were incubated under quiescent conditions, either in the presence or in the absence of ARA. Since the aggregation of pure αS in physiological buffer is known to be inefficient at quiescent conditions *in vitro*[98], the oligomerisation at 35 μM concentration of αS in the absence of ARA was negligible, and only a small increase in the numbers of detected oligomers was observed over a 24-h incubation (Fig. 5.2a). In contrast, 35 μM αS incubated with 1 mM ARA showed a rapid formation of oligomers, judged by the presence of high levels of detected FRET events, recorded shortly after the addition of ARA (Fig. 5.2a). The increase in the numbers of these species continued most rapidly for 6 h, followed by a plateau and a subsequent slight decrease after 20 h (Fig. 5.2a), which could be due to a partial disaggregation of the species or, alternatively, due to their higher-order association. In addition to the rise in the numbers of multimers over time, there was an identifiable increase in their average apparent sizes, observed from the broadening of the apparent size distributions (Fig. 5.2b). Typically, there was a progression towards larger species within first 6-7 h of the experiment, and no subsequent change, suggesting that their formation reached a steady state within this time period.

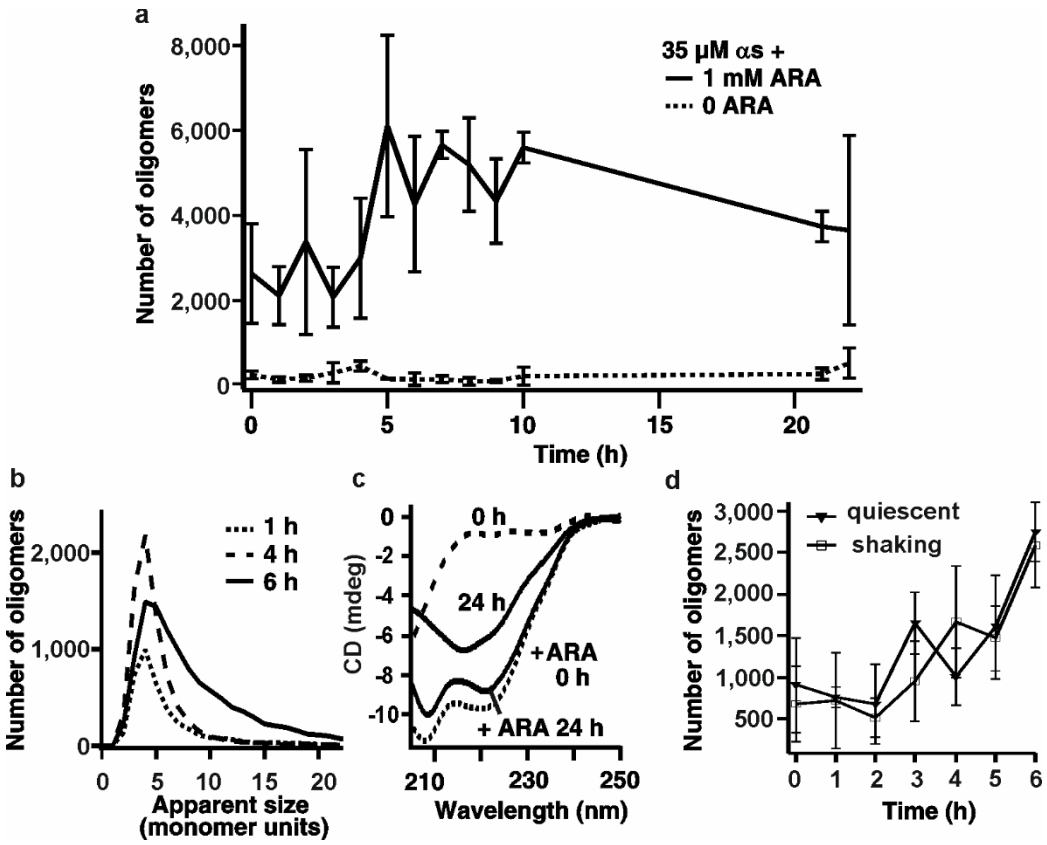

Figure 5.2. Effect of ARA on αS. **a.** Kinetic profile of αS aggregate formation induced by ARA at quiescent conditions, and of αS aggregation in pure buffer under quiescent conditions (n=3, std). **b.** Time-evolution of the apparent size histograms indicating growth of the aggregates. **c.** CD spectra of AF594-labelled αS with and without ARA. Without the acid, at 0 h protein is mostly in random-coil conformation, and contains beta-sheet structure at 24 h with shaking, indicated by a broad negative band at 217 nm. In the presence of ARA, both shortly after addition and after 24 h of incubation, CD spectra show the features corresponding to the alpha-helical state, negative bands at 208 nm and 221 nm. Raw data are shown because the protein concentration for the measurement was approximate, not allowing for an accurate conversion to mean residue ellipticity. **d.** Kinetic profile of aggregate formation by 35 μM αS in the presence of 1 mM ARA under either shaking or non-shaking conditions (n=3, std). Comparable results suggest the absence of the effect of shaking on the kinetics of aggregate formation in the presence of ARA.

5.3.2 CD spectra indicate a rapid attainment of alpha-helical conformation in the presence of ARA

CD measurements showed that the fluorescently labelled αS was intrinsically disordered in the absence of ARA at the beginning of the experiment, and acquired β-sheet conformation after 24 h of incubation, which overall indicated that the labelled protein assembled into fibrils as in previous works[79,83] (Fig. 5.2c). In contrast, the spectra of the samples in the presence of ARA were characteristic of alpha-helical conformation shortly upon addition of ARA, and after 24 h of

incubation (Fig. 5.2c). The observed attainment of alpha-helical conformation by αS in the presence of ARA is in agreement with previously reported results for αS with ARA[203], as well as for αS in the presence of the excess of a structurally similar docosahexaenoic acid[208]. Generally, the transition from the disordered to alpha-helical state is typical for αS upon its association with lipid membranes[178,180], and suggests that αS binds ARA at the chosen experimental conditions.

5.3.3 Results of control experiments to investigate the photophysical effects of ARA on AF dyes

In order to verify that in the measurements the coincident fluorescence signal was arising from the formed multimers of αS, control experiments were performed. Firstly, the absence of any background fluorescence from the ARA solution in buffer was confirmed. Secondly, it was checked that there was no apparent effect of ARA on the fluorescence signal from the fluorophores in the sm-FRET experiments, which was confirmed by performing control measurements using dual-labelled (AF488 and AF594) 40-base pair DNA samples with the oligonucleotides of the following sequences:

TCCD olig 1: AF488-TAGTGTAACTTAAGCCTAGGATAAGAGCCAGTAATCGGTA

TCCD olig 2: AF594-TACCGATTACTGGCTCTTATCCTAGGCTTAAGTTACACTA

FRETolig 1: TACTGCCTTTCTGTATCGC-AF488-
-TATCGCGTAGTTACCTGCCTTGCATAGCCACTCATAGCCT

FRETolig 2:
AGGCTATGAGTGGCTATGCAAGGCAGGTAACTACGCGATAAGCGATACAGA-AF594

The protocol for the preparation of the dual-labelled duplexes is detailed in the Methods section 5.2.4. Solutions containing TCCD DNA duplex were measured using a dual laser excitation, by illuminating the samples with overlapped 488 nm and 594 nm laser beams. FRET DNA duplex had the dyes close enough for the FRET process to occur; therefore, the experiments were carried out using 488 nm laser excitation, according to the same protocol as what was used for the sm-FRET measurements of the dual-labelled protein samples. In both cases, the numbers of the recorded coincident events in the donor and the acceptor channels were counted for the samples in pure buffer, and in the presence of ARA, and were compared (Fig. 5.3a and b). In addition, the average intensities of the fluorescence bursts in both the donor and the acceptor channels were compared (Fig. 5.3c).

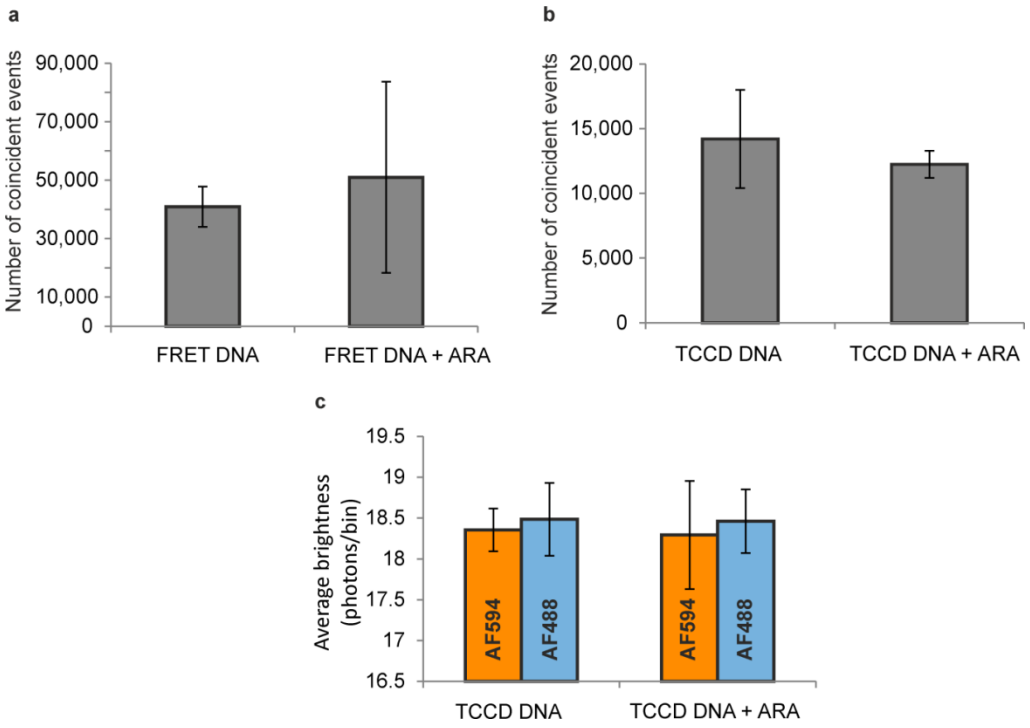

Figure 5.3. Control experiments to investigate the photophysical effects of ARA on AF dyes in the single-molecule experiments. **a.** and **b.** Number of coincident events recorded for either FRET or TCCD DNA duplexes diluted into pure buffer, or into buffer containing ARA (n=5, std). **c.** Average intensity of the fluorescence bursts in both the donor and the acceptor channels, derived from TCCD experiments with dual-laser excitation.

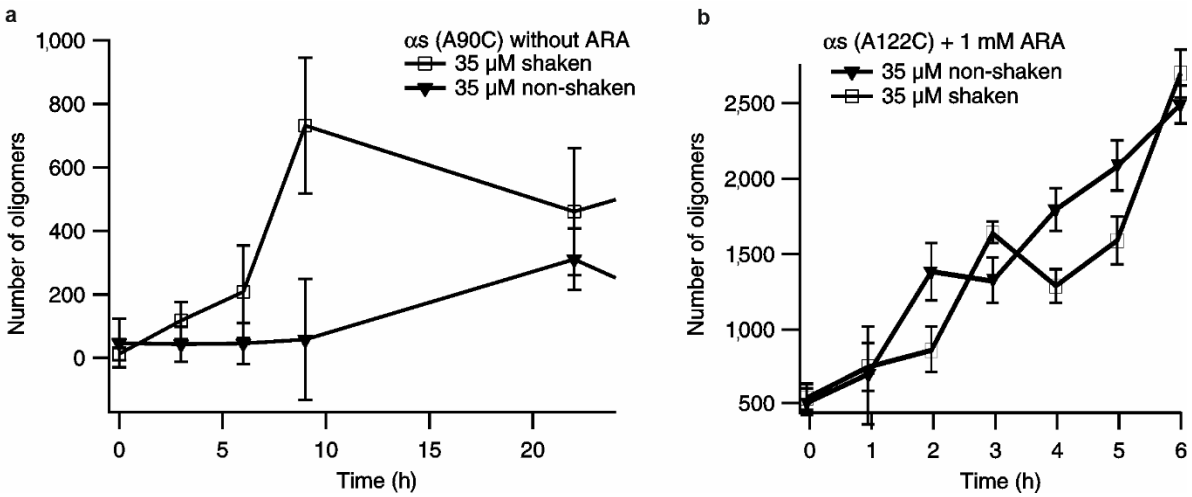

Figure 5.4. Control aggregation experiments. **a.** 35 μM αS in buffer. Aggregation is promoted by shaking, therefore shaking conditions are chosen for αS–only oligomer production in all further experiments (n=3, std). **b.** 35 μM A122C isoform of αS in the presence of 1 mM ARA (n=3, std). Comparable results under either shaking or non-shaking conditions, similarly to the results with A90C mutant of αS, shown in Fig. 5.2d.

5.3.4 Determination of the optimum conditions for the preparation of ARA-induced oligomers and oligomers in buffer

To check whether the formation of αS oligomers, promoted by ARA, occurred when shear forces were introduced, incubations with shaking were performed as well as incubations under quiescent conditions, which yielded comparable results at the same starting concentrations of αS and ARA (Fig. 5.2d). The preparations of the ARA-induced oligomers and the oligomers formed in its absence have been carried out at several other starting conditions in order to select the most high-yielding protocols. Firstly, it was tested whether the rapid multimerisation of αS promoted by ARA was specific to A90C isoform only, or whether it could occur when using another mutant of αS, A122C, where the fluorophore was incorporated in the C-terminal part insead of NAC region. Rapid ARA-induced oligomer formation was observed in these experiments when using an A122C mutant of αS instead of the A90C, where fluorophore was attached to a molecule of αS at residue 122 instead of residue 90 (Fig. 5.4). This indicated that the effect was not specific to the chosen A90C isoform of αS, and also may suggest that neither residue 122 nor 90 were directly involved in the binding to the FA. It is interesting to note that previously, the residues 2-19 and 123-140 in the αS molecule were identified to be homologous with a motif of FA-binding proteins[182]. The absence of any inhibition of the ARA-promoted oligomerisation in the case of incorporating the fluorescent dye at the residue 122, neighbouring with 123, may suggest that the ARA binding region in the C-terminal part of αS is either absent or comprises later residues. Since there was no difference in the acid-induced oligomer formation under either quiescent or shaking conditions, all subsequent ARA-induced oligomer preparations were carried out without shaking. In the case of control samples, 35 μM αS in Tris buffer, the oligomerisation was more efficient under shaking conditions, reflected by the higher numbers of the detected species under these conditions (Fig. 5.4), and therefore the subsequent preparations of αS oligomers in buffer were carried out with shaking. Typically, the observed numbers of oligomers were much higher in the samples containing ARA compared to the samples without the FA, indicating that the oligomers promoted by ARA were much more abundant. In addition, the aggregations using 35 μM αS and 1 mM ARA yielded the highest concentrations of ARA-induced oligomeric species amongst several other attempted combinations, summarised in Fig. 5.5. The quiescent preparation using 35 μM αS and 1 mM ARA was found to be the most high-yielding among other tested preparations, including incubations using different isoforms of αS or varying concentrations of both αS and ARA, as detailed in Figs. 5.4 and 5.5.

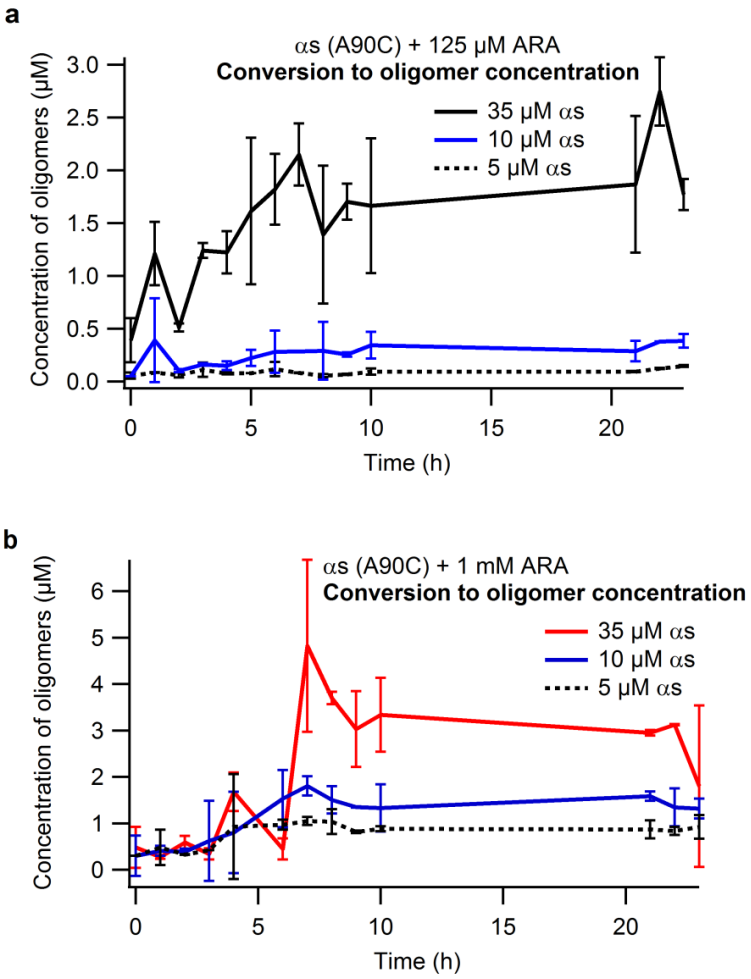

Figure 5.5. Kinetic profiles of ARA-induced oligomer formation at different starting total αS concentrations (n=3, std in each case). In **a.** and **b.**, oligomer concentrations were approximately estimated by normalising to the monomeric bursts (twice the bursts in the donor channel) to estimate the fraction of oligomers, and subsequent multiplication by the bulk starting total protein concentration. The highest estimated concentration of oligomers was generated at 35 μM αS in the presence of 1 mM ARA.

5.3.5 Further evidence for the differences between ARA-induced oligomers and oligomers formed in its absence

Once the ARA-induced oligomers of αS were observed, it was sought to compare these multimers to the toxic high-FRET oligomers of αS which are formed by the protein in aqueous buffer. As it was demonstrated in the preceding chapters, αS assembles into β-sheet-rich oligomers in aqueous buffer under constant agitation, consistent with the previously published results from this research laboratory[79,83,115]. Therefore, the same strategy as before was used to prepare these αS-only oligomers (see Methods section 5.2.2 for details), and a series of comparative experiments using ARA-induced oligomers and αS-only oligomers was carried out, as will be described in the following sections.

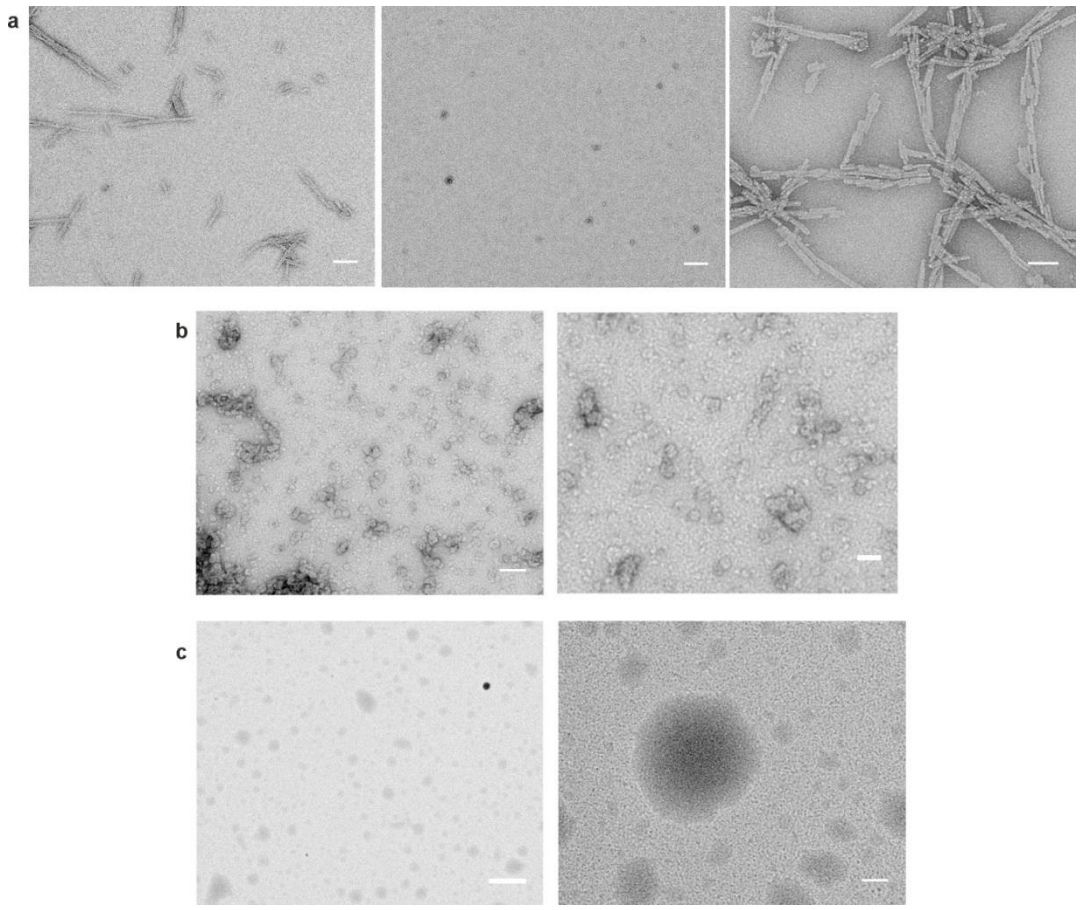

Figure 5.6. TEM images of aggregates. **a**. αS aggregates in buffer (35 μM, 24 h, shaking). From left to right: before centrifugation (15 min at 12,800 x g), a mixture of oligomers and fibrils is observed; oligomers are present in the supernatant after centrifugation; insoluble pellet after centrifugation contains fibrillar aggregates. Scale bars (left to right) 200 nm, 200 nm and 100 nm. **b.** ARA-induced oligomers of αS (35 μM, 1 mM ARA, 24 h, non-shaking). No fibrils observed after centrifugation. Abundant soluble oligomers and oligomer agglomerates are present. Scale bars 100 nm (left) and 50 nm (right). **c.** ARA acid micelles in buffer (1 mM ARA) in the absence of αS. Scale bars 1 μm (left) and 100 nm (right).

5.3.6 Morphological differences by TEM

Firstly, using TEM imaging, it was observed that the ARA-induced oligomers had markedly different morphologies compared to the oligomers of αS formed in aqueous buffer (Fig. 5.6). In the case of αS samples in buffer solution, after 24 h of incubation the solutions contained a mixture of monomers, soluble oligomeric species as well as insoluble fibrils (Fig. 5.6a). The majority of the insoluble fibrils could be removed by centrifugation, as judged by TEM and confirmed in previous studies[83], therefore this step was introduced for the preparation of the αS-only oligomers. In the ARA-containing αS solutions, abundant populations of oligomers were observed, frequently associated into higher-order assemblies (Fig. 5.6b). Interestingly, these aggregates were soluble, judged from the absence of

fibrillar aggregates in TEM images and the absence of insoluble pellets after centrifugation of the samples. In the absence of αS, at 1 mM ARA, micelles were formed (Fig. 5.6c). In the presence of the protein, however, the aggregates visualized using TEM were smaller compared to the micellar structures, which is consistent with the previously reported observation that αS is able to disrupt the micelles of ARA[203]. Overall, ARA-induced oligomers were larger and had less regular shapes than the αS-only oligomers, probably due to the association with the FA, and had a tendency to assemble into higher-order soluble agglomerates. They looked similar in morphology to the previously reported oligomers of αS in the excess of docosahexaenoic acid[208].

5.3.7 Comparative sm-FRET assays

Having observed by TEM that ARA-induced oligomers had different morphologies compared to αS-only oligomers, further differences were investigated between these types of species (Fig. 5.7). Firstly, a closer inspection of the FRET efficiency histograms revealed clear differences (Fig. 5.7a). The FRET efficiency histograms obtained for the samples of αS-only oligomers were in good agreement with the previous results, showing a conversion from low-FRET oligomer type to high-FRET oligomer type. As in previous experiments (Chapter 3), after 9 h of incubation mainly disordered oligomers were present with the mean FRET efficiency value E=0.4, whereas after 24 h the majority of the population contained more compact oligomers with high FRET values, E=0.6. In contrast, ARA-induced oligomers gave rise to FRET efficiency histograms that showed a single peak with E value of 0.5 after 9 h of incubation and a broader FRET distribution after 24 h, as shown in Fig. 5.7a. Since the appearance of FRET efficiency histograms was found to be well-correlated with the stability of oligomeric aggregates in previous works[79], the observed differences in the appearance of the FRET efficiency histograms of the ARA-induced multimers compared to αS oligomers in buffer solution could suggest differences in oligomer stabilities, and possibly differences in their structures. In addition, αS oligomers formed in the presence of ARA were found to be larger in terms of average numbers of monomers per oligomer, particularly at later incubations times past 6 h of incubation, as shown in Fig. 5.7b.

To explore whether these differences in the FRET histograms and apparent size distributions of the ARA-induced oligomers compared to αS-only oligomers were associated with the differences in oligomer stabilities, more comparative experiments were carried out. Previously, it was found that the high-FRET oligomers were more stable with respect to dilution into low ionic strength buffer in comparison to their preceding disordered oligomers. Therefore, the stabilities of ARA-induced multimers and αS-only (high-FRET) oligomers to the changes in ionic strength were compared.

Samples were diluted into buffers with varying ionic strength and the numbers of oligomers in solution were counted using sm-FRET (Fig. 5.7c). The result showed that the αS-only high-FRET oligomers prepared in buffer were stable with respect to the changes in ionic strength, which agreed with the previous results. In contrast, ARA-induced oligomers dissociated to a greater extent at low ionic strengths, which is probably due to the lack of β-sheet structure in these species.

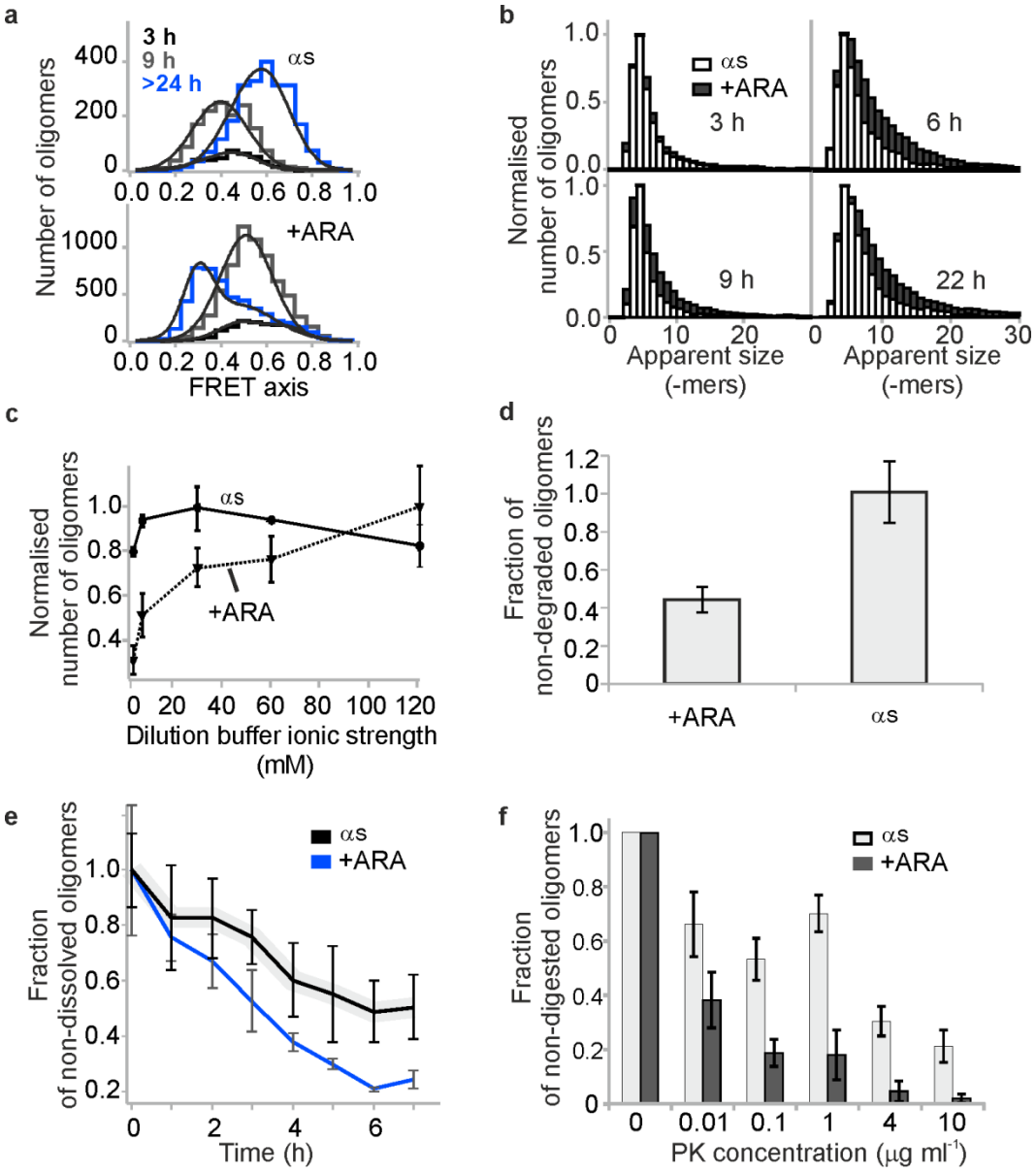

Figure 5.7. Comparative sm-FRET experiments to investigate the differences between ARA-induced oligomers and oligomers formed in aqueous buffer during 24 h of incubation. **a.** Appearance and time evolution of FRET efficiency histograms. Fits to eq. 2.3, with FRET eficiency values (E) of E(αS 9h)=0.4±0.01, E(αS 24h)=0.57±0.01, E(αS ARA 9h)=0.52±0.01, E(αS ARA 24h)=0.301±0.003 and 0.48±0.03. **b.** Comparison of apparent size distributions. **c.** Salt gradient measurements (n=3, std). **d.** Degradation by 26S proteasome over 12 h (n=3, std). **e.** Oligomer disaggregation upon dilution into aqueous buffer to 280 pM (n=3, std). **f.** Comparative dose-response assay of PK digestion (n=3, std).

Next, it was investigated whether the lower structural stability of ARA-induced αS oligomers could facilitate their enzymatic degradation. The 26S proteasome is the main protein degradation machinery in eukaryotic cells, including degradation of αS monomers upon modification by ubiquitin[209], yet it was reported to be inactive to certain αS aggregates[210]. In order to compare the susceptibilities of the ARA-induced oligomers and the αS-only oligomers towards degradation by the proteasome, comparative assays were carried out, using identical degradation mixtures and incubation conditions for both kinds of oligomers and exposing both types of aggregates to mammalian 26S proteasome for a period of 12 h (Fig. 5.7d). Over this selected incubation time, the numbers of ARA-induced oligomers were reduced upon proteasome-treatment. In contrast, the samples devoid of ARA were not targeted by the proteasome, in agreement with the previous literature. This suggested that ARA-induced oligomers were more degradable by proteasome in comparison to the αS-only oligomers.

To confirm that ARA-induced oligomers were less stable than αS-only oligomers, oligomer disaggregation experiments were carried out, where the oligomeric samples were diluted to single-molecule concentrations in buffer, and left under quiescent conditions for several hours. During this time, the decrease in the numbers of oligomers due to their dissociation into monomers in solution was monitored by sm-FRET (Fig. 5.7e). While the decrease in the numbers of oligomers was observed for both the ARA-induced oligomers and the oligomers formed in its absence, it was faster for the former species confirming the previous findings of their lower stability. This difference points towards structural differences of the ARA-induced oligomers compared to αS-only oligomers.

To gain further information about this difference, comparative proteolytic digestion assays were performed, by exposing both the ARA-induced oligomers and the oligomers formed in the absence of ARA to varying concentrations of PK enzyme (Fig. 5.7e). Previous studies showed that high resistance to PK digestion was characteristic for β-sheet conformation in αS aggregates, and amyloid fibrils were the most resistant in this assay[79]. Here, both types of oligomers were susceptible to PK digestion. However, the fractions of remaining non-digested oligomers were consistently higher in the samples containing αS-only oligomers, additionally indicating that the ARA-induced oligomers were less stable, consistent with the lack of β-sheet structure in these aggregates.

5.3.8 Attempts to remove ARA from the multimers

Lastly, it was investigated whether ARA itself was a constituent of the ARA-induced oligomers. Due to the observed tendency to assemble into large agglomerates (Fig. 5.6b), it was presumed that the association of ARA-induced oligomers into larger aggregates could occur via the free FA molecules,

and it was set out to test whether these species could remain stable upon decreasing the concentration of ARA in solution. To address this, ARA- and αS-containing samples were prepared as described above, and the concentration of the FA was decreased by washing with the excess of aqueous buffer and by subsequently concentrating the protein solutions, as described in Methods (section 5.2.10). This resulted in the increase in the numbers of recovered oligomers (Fig. 5.8a), as well as an 11 ± 5% increase in the population of small species consisting of less than 6-mers, and a drop in the sub-population of larger oligomers (Fig. 5.8b). This indicated that the multimers had undergone a partial dissociation during the process (Fig. 5.8b), suggesting that the excess of FA molecules stabilised the larger multimers. Nevertheless, the finding that the majority of the aggregates could be recovered and remained sufficiently stable to be detected at picomolar concentrations of the protein in the sm-FRET experiments implies a degree of stability, and indicates a strong binding of ARA to αS in these aggregates. These observations are compatible with the previous reports of the stability of the FA-induced multimers of αS upon chromatographic procedures[202,208], and highlight the difficulty of removing FAs from αS under these conditions. The result that the oligomers partially dissociated upon the decrease of FA suggests that ARA is a stabilising constituent of these aggregates, which is consistent with previous related findings that αS co-aggregated with anionic lipids[211]. Consistent with this, the CD spectrum of αS solution, recorded after decreasing the concentration of ARA, indicated that the alpha-helical conformation was preserved in the samples (Fig. 5.8c).

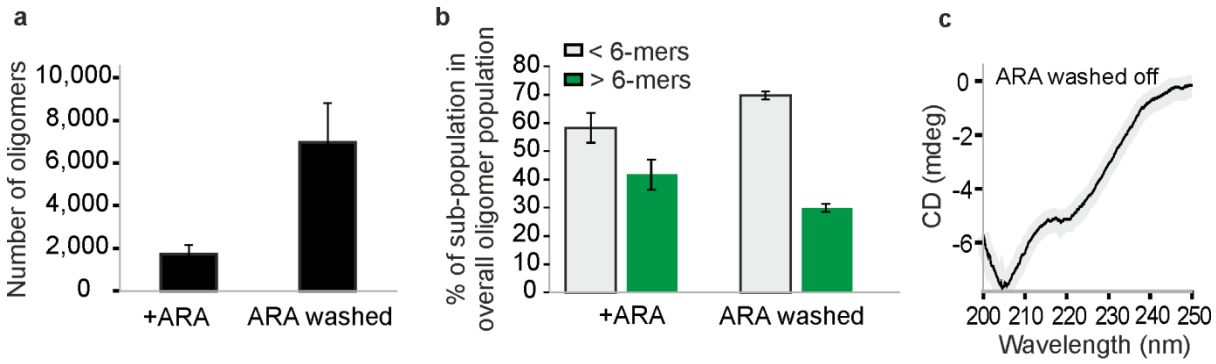

Figure 5.8. ARA depletion experiments and comparative cell assays. **a.** Numbers of oligomers, detected by sm-FRET before and after decreasing the concentration of ARA by washing with excess buffer (see Methods section 5.2.10) (n=3, std). **b.** The increase in the smallest oligomers (2-5-mers) is observed, whereas the fraction of larger species drops, indicating that oligomers undergo a partial dissociation upon separation from the FA. **c.** CD spectrum acquired after washing the protein sample, showing that alpha-helical conformation is retained. The detection of intact small multimers and alpha-helical conformation indicate that ARA is still present in solution and bound to αS in these multimers. Thus, it is very difficult to fully separate the FA from αS under these conditions. (Raw data are shown because the protein concentration for the measurement was approximate, not allowing for an accurate conversion to mean residue ellipticity).

5.3.9 ARA-induced oligomer formation at physiologically-relevant concentrations of αS and ARA

In the above experiments ARA has been used at high concentration above its CMC value[203,204]. Because ARA is a biologically relevant molecule and occurs *in vivo* at concentrations below its CMC, the experiments were extended to more physiologically-relevant ARA concentrations of 2-10 μM[196] (Figs. 5.9 and 5.10). In addition, the concentrations of αS protein at the synapse were reported to be in the range 2-5 μM[212]. Therefore, to mimic the concentrations of both αS and ARA found *in vivo*, 2 μM αS and 10 μM ARA were combined. Under these conditions, a rapid multimerization was still observed shortly after the addition of ARA, as shown in Fig. 5.9a, and an increase in the numbers of oligomers was present during the first 6 h, resembling the timescales of the process at higher concentrations (Fig. 5.2a). The numbers of the detected oligomers, and their estimated concentrations (Fig. 5.10b) were lower in comparison to the results in the high-concentration experiments, which highlights the challenge of monitoring this low-concentration process by more conventional bulk methods. Despite the lower overall numbers of oligomers, the growth of these species was again observed, with similar apparent size distributions compared to the higher-concentration reaction (Fig. 5.9b), and very similar FRET efficiency histograms (Fig. 5.9c). Further, CD measurements were used to determine the conformation of these multimers. Preliminary attempts to measure the solutions containing 2 μM αS and 10 μM ARA resulted in the spectra indicating the presence of intrinsically disordered protein. This was consistent with the single-molecule observations that even though the multimers were present in the solutions, the majority of αS was still in its monomeric form, as is indicated by the low estimated concentrations of the multimers (Fig. 5.10b). Therefore, the multimers were enriched using 100 kDa spin-filters, as described in Methods (section 5.2.5), and their CD spectrum indicated that these species were alpha-helically-folded, similarly to the species generated at 35 μM αS with 1 mM ARA (Fig. 5.9d). To note, the retention by the 100 kDa cutoff filter is consistent with the oligomers being the size of a tetramer and larger.

Based on these results, it could be concluded that the preparation at 2 μM αS and 10 μM ARA yielded the same species as the higher-concentration preparation, even though the overall numbers of multimers were low at these physiologically-related concentrations. To confirm this conclusion, the disaggregation of the low-concentration multimers was monitored, by diluting the samples to single-molecule concentrations and recording the decrease in their numbers over time due to their dissociation. The resulting disaggregation profiles were similar to the ones obtained for the high-concentration preparations at 35 μM αS and 1 mM ARA, as shown in Fig. 5.9e.

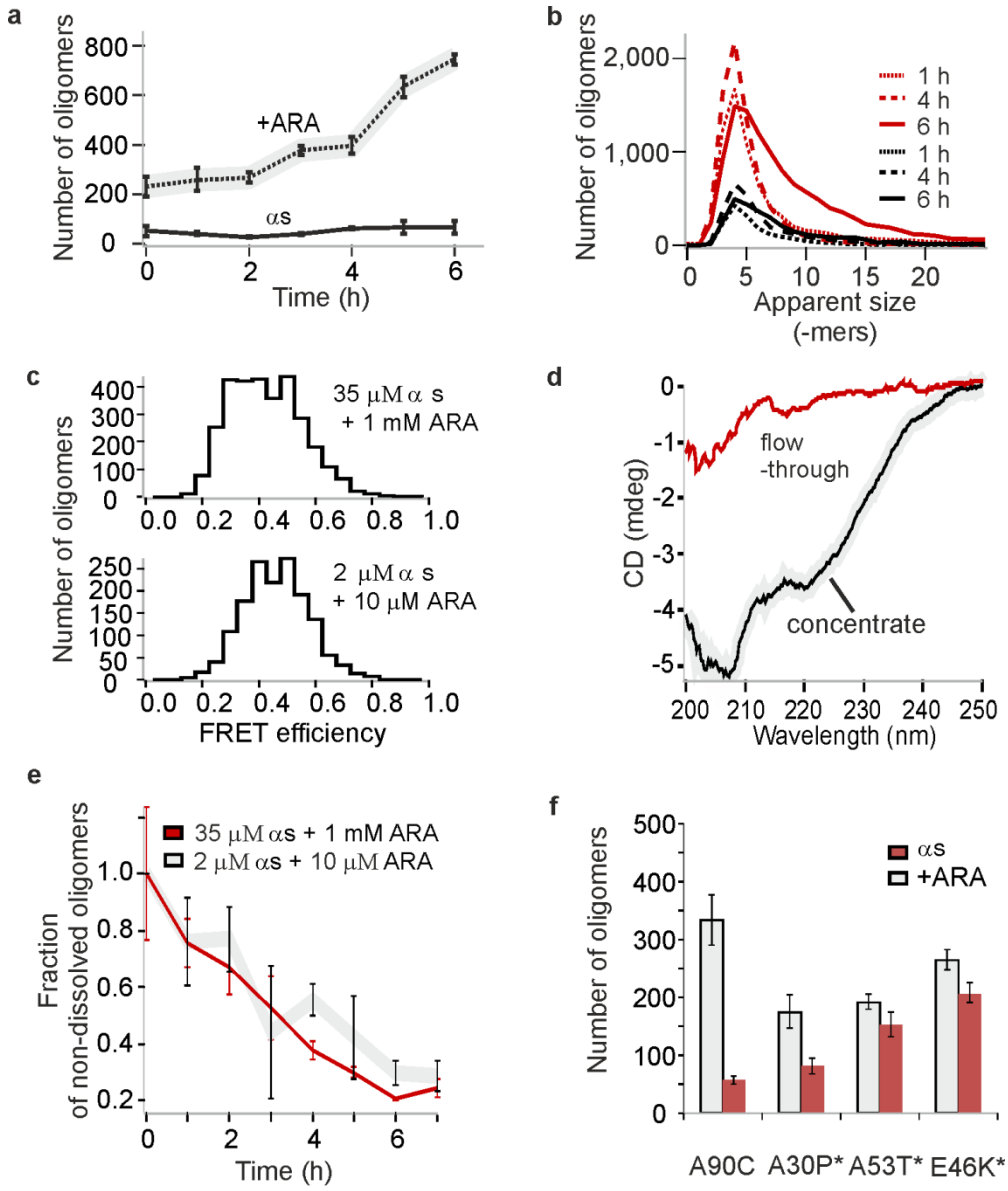

Figure 5.9. Experiments using physiological concentrations of αS and ARA. **a.** Kinetic profile of oligomer formation at 2 μM αS in the presence of 10 μM ARA (dashed line), and in the absence of ARA under the same conditions (black line) (n=3, std). **b.** Comparison of apparent size distributions at 35 μM αS with 1 mM ARA (red), or 2 μM αS with 10 μM ARA (black). **c.** Representative FRET efficiency histograms, resulting from sm-FRET analysis of the oligomers formed with either 35 μM αS with 1 mM ARA, or 2 μM αS with 10 μM ARA after 6 h. After this and later times, there was no difference in the appearance of the histograms, apart from lower total numbers detected in the lower-concentration samples, when the same protein concentration was used for the detection. **d.** CD spectra of the solutions of 2 μM αS with 10 μM ARA after 24 h and enrichment using 100 kDa spinfilter. (Raw data are shown because the protein concentration for the measurement was approximate, not allowing for an accurate conversion to mean residue ellipticity). **e.** Overlaid oligomer disaggregation profiles upon dilution into aqueous buffer to 280 pM of 35 μM αS samples with 1 mM ARA (red), and 2 μM αS with 10 μM ARA (grey) (n=3, std). **f.** Numbers of oligomers detected after >30 h using a range of αS isoforms, either A90C or pathological mutants, at 2 μM with 10 μM ARA (grey) or in the absence of ARA (red) (n=6, sem).

Lastly, in order to test whether disease-associated point mutations of αS could lead to the self-assembly upon the action of ARA, the samples were prepared using 2 μM αS as well as 2 μM A30P, A53T and E46K mutants of αS, with the addition of 10 μM ARA. As a result, the formation of oligomers was observed for αS, as before. In the case of the mutants, however, the samples contained more aggregates than the wt (A90C) protein in the absence of ARA, and the presence of ARA had less effect on the number of aggregates, as shown in Fig. 5.9f. Thus, at the chosen conditions, the effect of ARA to induce a higher number of oligomers (compared to the number generated in its absence) was comparable between wt αS and A30P mutant, and much less apparent for the pathological mutants A53T and E46K in comparison to the wt αS.

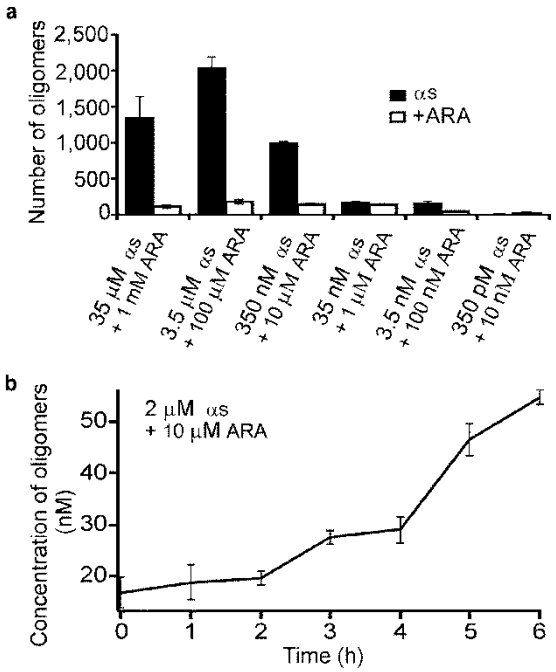

Figure 5.10. Extension to lower concentrations of αS and ARA. The same sample preparation protocol was used as for the preparation of ARA-induced oligomers in the previous experiments, but the total concentrations of both αS and ARA were gradually decreased. **a.** Keeping the same ratio of ARA:αS, the induction of oligomerisation was observed reproducibly starting from 10 μM of ARA (n=3, std). As control samples, αS in buffer solutions were incubated in the absence of ARA under the same conditions (n=3, std). **b.** Kinetic profile of oligomer formation at 2 μM αS with 10 μM ARA, converted to approximate oligomer concentrations.

5.4 Summary and conclusions

There is evidence of αS interplay with fatty acids (FAs) *in vivo*, and arachidonic acid (ARA) is one of the most abundant FAs in grey matter of human brain. In this chapter, alpha-helical multimers of αS were generated in the presence of ARA, and their differences compared to the toxic β-sheet-rich oligomers of αS were demonstrated. ARA-induced oligomers differed from the oligomers generated in the absence of ARA in both morphology and size, displayed lower stability towards the changes in buffer conditions and had a higher propensity to disassemble upon sample dilutions. In addition, they were more susceptible to enzymatic digestion and degradation by proteasome. Despite their apparent lower stability in comparison to the αS-only oligomers, these multimers could preserve their conformation upon the reduction of ARA concentration, which is particularly significant considering that ARA is highly transient *in vivo*[194].

The ARA-induced oligomers in these experiments were evidently distinct from the β-sheet-rich oligomers formed during the aberrant aggregation of αS. Moreover, they were resistant to fibril formation, as judged from TEM imaging, and required ARA for their stabilisation, as concluded from the ARA washing experiments. These species may therefore represent the products with an alternative conformation involving both αS and ARA, as is schematically illustrated in Fig. 5.11. Because their formation is fast and recruits monomeric αS, it can compete with the slow formation of high-FRET β-sheet-rich oligomers particularly when the total monomer concentration is low. It was previously shown that the high-FRET β-sheet-rich oligomers of αS were the most cytotoxic species[79]. Therefore, any competing mechanisms that inhibit their formation may be highly neuroprotective. This is consistent with the finding that disease-associated mutants of αS had a lower tendency to assemble into the FA-induced species compared to the wt αS, which leaves them in a free state and may ultimately lead to the generation of higher concentrations of toxic β-sheet-rich oligomers via the aberrant aggregation mechanism. It is interesting to note that the ARA-induced multimers described here bear similarities with previously reported oligomers of αS, prepared by the addition of a polyphenol epigallocatechin-3-gallate (EGCG)[213,214], which is a natural compound and a major constituent of green tea. Both ARA-induced oligomers and EGCG-induced oligomers are formed rapidly upon the addition of the corresponding inducer, are off-pathway aggregation products, have a tendency to agglomerate into higher-order assemblies and posess lower cytotoxicity compared to the on-pathway β-sheet-rich aggregates of αS. In contrast, however, the EGCG aggregates have more regular spherical shapes in comparison to ARA-induced species and do not acquire the alpha-helical secondary structure even upon prolonged sample incubations, as determined by CD measurements[214].

Considering the remarkable ease of formation of the ARA-induced multimers and their stability under physiologically relevant concentrations, it can be argued that the formation of closely-related

multimers may potentially occur *in vivo*. In line with this, multiple properties of the ARA-induced oligomers show close resemblance to the native alpha-helical multimers of αS extracted *ex vivo*[45,215] such as being small, below 10-mers in apparent size, alpha-helically-folded and aggregation-resistant. In the described experiments, these multimers were present in the excess of monomeric αS, which was concluded from the observation of an excess of monomeric bursts in addition to the multimers during sm-FRET measurements, and from the CD spectra of the flow-through after their enrichment (Fig. 5.9d). This may suggest that these species are in equilibrium with monomeric αS, similarly to what was proposed for the native multimers[216,217]. It should be noted, however, that the full-length N-terminally acetylated αS is the major form of αS in both PD and healthy brain tissue[161], and therefore the influence of this modification on the formation of the ARA-induced oligomers remains to be determined.

Clearly, although ARA has been used in the present study, numerous polyunsaturated FAs and their mixtures *in vivo* may play a similar role to facilitate the formation and stabilization of aggregation-resistant alpha-helical multimers of αS. This may contribute towards the reduction in cytotoxicity associated with these FAs[218,219] in the context of PD and related disorders. Given the strong biophysical evidence for the formation of alpha-helical multimers of αS in the presence of ARA in the described experiments, it can therefore be suggested that ARA and other polyunsaturated FAs may be the unidentified stabilising co-factors for the native multimers of αS, suggested previously[220]. Thus, polyunsaturated FAs may play a crucial role in αS homeostasis via the stabilization of native multimers and the prevention of aberrant aggregation of αS.

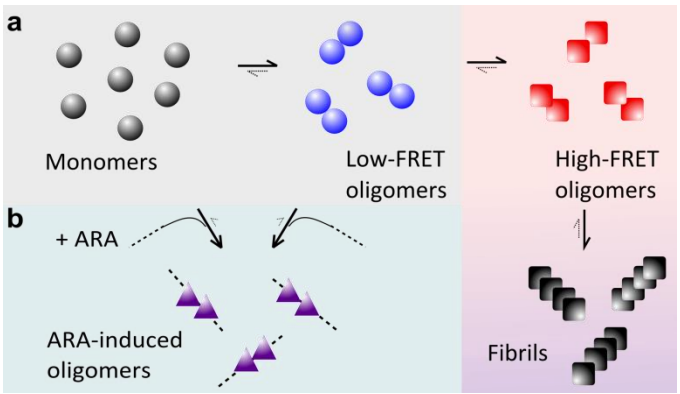

Figure 5.11. Schematic outline of the self-assembly mechanisms of αS in the absence and in the presence of ARA. **a.** Without ARA, monomeric protein assembles according to the aberrant aggregation mechanism. In this mechanism, αS forms disordered low-FRET oligomers, which convert to toxic and β-sheet-rich high-FRET oligomers, which in turn convert into fibrils. **b.** Upon the addition of ARA, the alpha-helical ARA-induced multimers are formed, comprising both αS and ARA. Equilibrium with monomer is consistent with the immediate ARA-induced oligomer formation, and equilibrium with low-FRET oligomers can account for the observed time-progression during first 6 h of the reaction.

Chapter 6
Mixed oligomerisations monitored by TCCD

In this chapter, steady-state populations of oligomers were measured at a range of low starting protein concentrations of αS, Aβ and tau k18 and their combinations using single-molecule TCCD technique. The low starting protein concentrations were chosen to mimic the physiological abundance of these proteins.

6.1 Introduction

6.1.1 Amyloid-beta peptide

Amyloid beta (Aβ) is a small (around 4.5 kDa) extracellular peptide that is a proteolytic cleavage product from a larger transmembrane amyloid precursor protein (APP)[221]. The peptide comprises 28 residues of the extracellular domain of APP and 11-15 residues of its transmembrane domain[222] (Fig. 6.1). Aβ is central in the so-called amyloid cascade hypothesis, which states that the aggregation and deposition of this peptide are the primary molecular events in AD, and later are followed by the phosphorylation and deposition of tau and widespread neuronal death[224].

Even though the physiological function of Aβ remains unknown, the peptide was proposed to act as an antioxidant due to its property to trap multivalent cations of metals such as copper, iron and zinc via direct binding, abolishing their involvement in redox reactions[225]. Recent studies have suggested a surprising role for Aβ as an antifungal and antibacterial agent in cell culture and animal models, and its oligomerisation and fibrillisation were presented as protective mechanisms against the pathogens[226].

The most common isoforms of Aβ are the peptides composed of 40 and 42 residues (Aβ40 and Aβ42)[227]. The Aβ42 isoform has an additional Ile-Ala dipeptide at its C terminus, making it more hydrophobic and more aggregation-prone than Aβ40[228,229]. Hence, while the relative ratio of the Aβ40 to Aβ42 in cerebrospinal fluid (CSF) is approximately 9:1, the concentration of Aβ42 is enriched relative to Aβ40 in deposits such as amyloid plaques[230,231]. Moreover, some early-onset versions of AD have been related to the overproduction of Aβ42 relative to Aβ40[232], and an increase in the ratio of Aβ42 to Aβ40 cleaved from APP has been correlated to increase in toxicity both *in vitro* and *in vivo*[233-238].

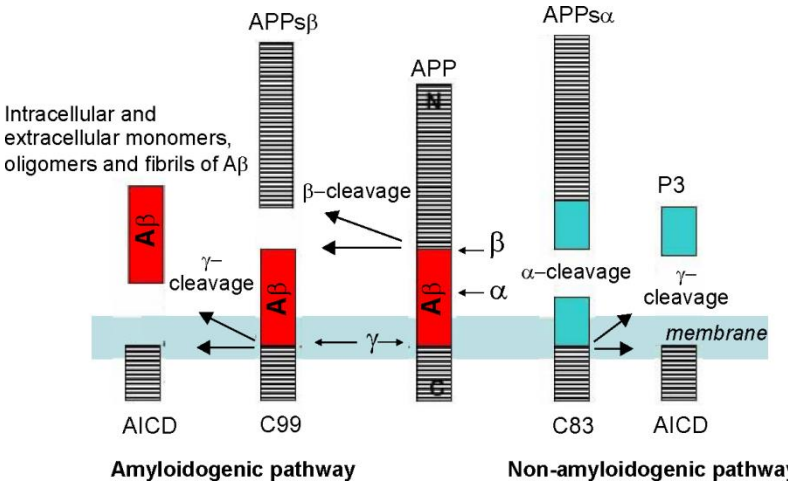

Figure 6.1. Schematic representation of the secretase cleavage of APP to the Aβ peptides. In the amyloidogenic pathway, APP is sequentially cleaved by β- and γ-secretases. This pathway competes with a non-amyloidogenic pathway where APP is cleaved by α-secretase within the Aβ domain. All three secretases have been characterised in detail[223] and the cleavage by β-secretase was determined to be the rate-limiting step during the generation of Aβ. (From Cole and Vassar, 2007)[223].

6.1.2 Evidence for co-oligomer formation between Aβ isoforms

Although solid fibrillar deposits of Aβ accumulate in AD brains, the major cytotoxic effects causing the earliest pathological events are associated with smaller aggregates, Aβ oligomers[239]. Such species are formed via the association of monomeric Aβ and ultimately polymerise into amyloid fibrils when the total protein concentration exceeds the critical aggregation concentration (CAC)[240]. Due to their transient presence and low abundance, the oligomers have been difficult to characterise using conventional experimental techniques[241], particularly in the systems containing multiple isoforms of Aβ. There have been multiple studies of the mixtures of Aβ isoforms, demonstrating that Aβ40 and Aβ42 co-interact during the aggregation reaction[242-246]. Furthermore, there is evidence that Aβ40 and Aβ42 can form co-oligomers *in vitro*[234,242], and on the surface of neurons[247]. A detailed study revealed that while Aβ40 and Aβ42 form separate fibrils in solution, the peptides co-interact in the early stages of Aβ aggregation, during primary nucleation[248].

Since most biophysical studies are typically performed at non-physiological high-micromolar concentrations of Aβ, it has not been possible to extrapolate the observations to very low total concentrations of Aβ peptide observed *in vivo*[249]. Because of the demonstrated strong and non-linear concentration dependence of Aβ aggregation[250-253], a meaningful extrapolation would require direct measurements of Aβ oligomer populations at sub-micromolar peptide concentrations, providing a strong motivation for the direct measurements of Aβ oligomerisation at nanomolar concentrations carried out in this chapter.

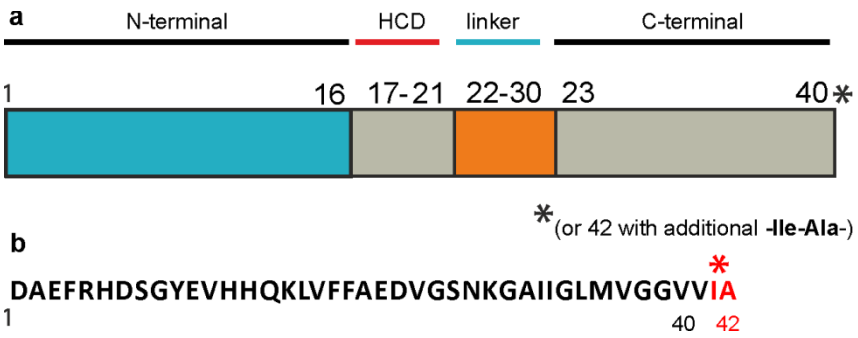

Figure 6.2. Schematic diagram of the primary sequence of the full-length Aβ peptide. **a.** Schematic diagram of the primary sequence showing the main regions. N-terminal domain comprising first 16 residues is believed to be disordered in solution. The hydrophobic central domain (HCD) and C-terminal domain have high propensity for the formation of β-sheet structure. The two domains are connected with a flexible hydrophilic linker comprising residues 22-30. The most common isoforms of the peptide, Aβ40 or 42, differ in either the presence or the absence of isoleucine and alanine residues at the end of the C-terminal domain. **b**. The primary sequence of Aβ40 and Aβ42. (Figure adapted from Hu *et. al.* 2012)[254].

6.1.3 Evidence for Aβ and αS co-interaction in human brain and in cell culture

The *in vivo* interaction of αS protein with Aβ dates back to the original discovery of αS in 1993, when a "non-amyloid component" or NAC region, composed of 35 residues that correspond to the residues 61-95 of the full-length αS protein was identified in AD brain amyloid[3]. NAC was the second component after Aβ that was identified in amyloid deposits purified from human AD brain, and this occurred prior to the discovery that αS was the major component of LBs in PD[64]. The localisation of αS to brain amyloid in AD strongly points towards a potential co-interaction of αS and Aβ.

More than half patients with AD were found to have LB inclusions, and their presence was associated with a faster disease progression (reviewed in Galpern and Lang, 2006[255]). For example, 56.8% of the examined brains of 145 patients with sporadic AD contained LB inclusions[256]. The co-occurrence of both proteins in the diseased human brain was further supported by their co-immunoprecipitation from the samples of human patients with AD and DLB[257]. It was reported that the levels of αS were increased in AD patients relative to healthy controls, and this increase was associated with decreased cognition[258]. Furthermore, AD-associated lesions such as plaques of Aβ were observed in the patients with PD and the majority of cases with DLB. Their presence was linked to a faster deterioration of cognition and neurodegeneration[259]. Interestingly, the spatial distribution of pathological lesions was different amongst different types of neurological conditions. For example, brains of patients with dementia suffering from AD with LB pathology displayed a distinctly different distribution of LB inclusions in comparison to the brains of PD patients, as has been demonstrated in a relatively recent

comprehensive study utilising cluster analysis[260]. Despite the established co-occurrence of αS and Aβ in neurological diseases, their mutual effects and the underlying molecular-level mechanisms of their co-interaction still remain to be understood, and some surprising discoveries of this interplay have already been made both *in vitro* and *in vivo*. For example, the injection of soluble αS into AD transgenic mice unexpectedly resulted in the inhibition of amyloid plaque formation and an increase in the levels of soluble Aβ in CSF, demonstrating that this cross-interaction may have direct consequences to the disease progression and thus requires an in-depth investigation[261].

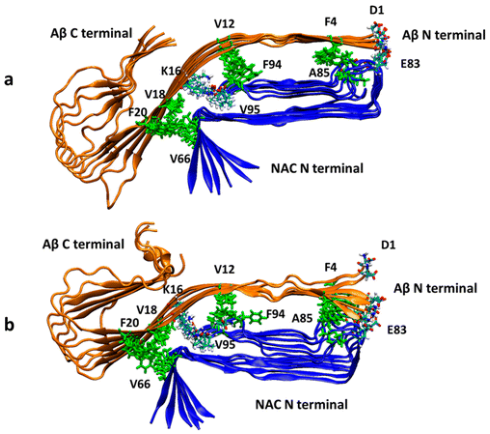

Figure 6.3. Co-oligomers between Aβ42 (orange) and the NAC region of αS (blue), modelled using molecular dynamics simulations. Figure from Atsmon-Raz *et. al*., 2016[262].

6.1.4 Aβ and αS co-interaction *in vitro*

Given the strong evidence for a co-interaction of αS and Aβ *in vivo*, research *in vitro* has been carried out in order to understand this process on a more fundamental level. The direct binding between αS and various isoforms of Aβ in solution was demonstrated as early as in 1995, and was shown to accelerate the aggregation of Aβ[263]. In that study, the binding regions were found to comprise the residues 25-35 in the N-terminal region of Aβ, and C-terminal part of αS. Subsequently, another *in vitro* study confirmed the binding between αS and Aβ40, and reported the epitope to be within residues 1-56 and 57-97 of αS[264]. In this study, recombinant biotinylated αS was also shown to bind to amyloid derived from AD brain. Furthermore, using multidimensional NMR spectroscopy, a direct binding between αS and either Aβ40 or Aβ42 was demonstrated[265].

The interplay between αS and Aβ *in vitro* during their aggregation has been investigated in numerous studies, with the outcomes dependent on the experimental conditions and the starting state of the proteins. For example, it was found that pre-formed sonicated fibrils and cross-linked oligomers of αS and Aβ (both 40 and 42 isoforms) could cross-seed each other's aggregation[266]. In addition, dopamine-induced off-pathway oligomers of αS were found to promote the formation of β-sheet-rich

oligomers of Aβ42, without any incorporation of αS in these aggregates[267]. The fibrillisation of Aβ40 in solution was found to be inhibited by soluble αS, and this effect was even more prominent in the presence of an engineered fibrillisation-incompetent soluble αS with a disulphide bond between residues 41-48[268].

The formation of cross-aggregates containing both αS and Aβ has been predicted and observed in several studies. Molecular dynamics simulations have revealed that the direct interaction between αS and Aβ42 could lead to the formation of stable ring-shaped hybrid oligomers in solution and on lipid membranes[257]. In another molecular dynamics simulation, the formation of hetero-dimers was predicted between αS(1-95) and Aβ42 in solution[269]. Even more recent molecular dynamics simulations have modelled combining pre-formed oligomers (hexamers) of αS61-95 with hexamers of Aβ42 to reveal their cross-interactions to form co-oligomers[262], as shown in Fig. 6.3. It was found that the resulting co-oligomers were heterogeneous in structure and that αS oligomers were able to promote the formation of new strands in Aβ42 oligomers during this co-interaction. Moreover, the formation of a dimeric complex between αS(1-15) and Aβ(1-16) upon their coordination to Cu^{2+} ions was observed experimentally[270].

6.1.5 Tau protein

Tau is a microtubule-binding protein found in neurons of vertebrates, that is proposed to stabilise microtubules and regulate microtubule networks, as well as to bind to filamentous actin, recruit signalling proteins, and to take part in the regulation of microtubule-mediated transport[271]. The protein molecule is broadly divided into two regions, a positively-charged carboxyl-terminal microtubule-binding domain that can be phosphorylated[272], and an amino-terminal projection domain. There are multiple naturally occurring isoforms of this protein, and six isoforms exist in human brain, with molecular weight ranging from 45 kDa to 65 kDa due to the variation in the length of the projection domain and the number of microtubule-binding repeats[273].

Tau is an IDP in solution, but can aggregate into solid fibrillar deposits, frequently referred to as "paired helical filaments" (PHFs) in AD and other tauopathies[274]. Characterisation of the PHFs purified from human brain showed that they comprised β-sheet structure surrounded by unstructured protein[275], and were thus amyloid in nature.

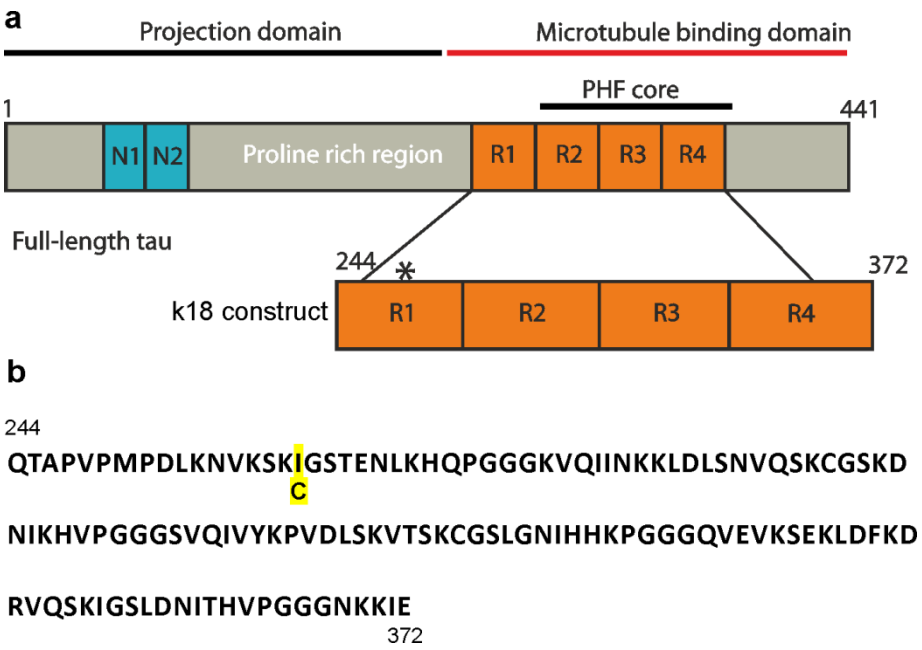

Figure 6.4. a. Schematic diagram of the primary sequence of tau protein. Two main parts are shown, the projection domain that does not bind to the microtubules, and the microtubule binding domain. Repeats R1-R4 consist of 31-32 residues each, and comprise the PHF core. The six isoforms found in human brain arise from the presence or the absence of two inserts near the N terminus (N1 and N2) and one in the carboxyl-terminal parts (R2). The k18 construct is shown, and a specific mutation, I260C, introduced for fluorophore incorporation is denoted by a black star. **b.** Primary sequence of tau k18. The residue 260 with a substitution from isoleucine to cysteine (for fluorophore incorporation) is shown in yellow. (Figure adapted from Shammas et. al. 2015[159]).

6.1.6 The aggregation of tau protein

The *in vitro* assembly of the full-length protein into structures resembling PHFs has been found to be inefficient, and various shorter constructs of this protein have been engineered. For example, constructs k19 and k18, which represent the central part of microtubule binding region, responsible for forming PHFs[276]. The difference between k19 and k18 is that they correspond to fetal and adult tau, respectively. At neutral pH, the full-length isoform htau40 and tau constructs k19 and k18 have the net positive charge of +2, +7 and +10 respectively[277].

The full-length protein and the shorter constructs show similar trends in their folding and aggregation behaviour that is overall governed by their high charge and very low hydrophobic content. It has been shown that the proteins remain monomeric in solution of varying pH and salt concentration even at micromolar concentrations of the proteins, and the aggregation reaction was triggered in the presence of polyanions such as heparin[277] or FAs[275]. It was proposed that polyanions favoured the aggregation reaction by neutralising the positive charges in the repeat region of tau. With heparin present in solution, the aggregation of tau and its repeats was found to be most efficient at pH values near its p*I*

values, indicating that the minimisation of net charge promoted this process[277]. In addition, the aggregation was found to be more favoured at low ionic strength, further supporting the ionic character of tau-heparin interactions driving the self-assembly. Interestingly, the increase in the hydrophobic content, monitored by ANS dye binding during the aggregation process, was found to be the same for full-length tau as for the repeats, suggesting that the hydrophobic regions are present mainly in these repeat domains of the protein[277]. Multiple post-translational modifications, such as phosphorylation, glycosylation or truncations by proteolytic cleavage, have been identified for tau and their effects on the aggregation of tau still require elucidation. For example, it has been shown that certain forms of hyperphosphorylated tau lead to the acceleration of aggregation, while others are inhibitory[278].

6.1.7 Evidence for tau and αS co-interaction in human brain and in cell culture

The co-occurrence of solid deposits of tau protein and of αS has been observed in a wide range of neurodegenerative conditions such as PD with dementia, DLB, LB variant of AD, Down's syndrome or Guam-Parkinson-ALS dementia[279]. Moreover, as it has already been stated in section 6.1.3., more than half patients with AD were found to have LB inclusions, and their presence was associated with faster disease progression[255]. In addition, the analysis of fractions from PD brains has identified the presence of elevated levels of phosphorylated tau[279].

Interestingly, numerous histopathological studies have identified the presence of both proteins within the same solid inclusions in human brain. For example, a detailed mass spectrometry study of cortical LBs has identified around 300 proteins as the components of these deposits, such as molecular chaperones and various cytoskeletal proteins including tau[281]. Using double-immunolabelling electron microscopy, it was observed that the two proteins formed separate homo-filaments within the same inclusions in the brains of patients with parkinsonism and DLB[282]. In addition to the observation of co-aggregates by double immunostaining, their morphological patterns have been characterised in great detail and classified into separate types depending on the shape of the lesions and the location of the overlapping areas[280]. Furthermore, using oligomer-specific antibodies that recognised either αS or tau, hybrid oligomers containing both proteins were found in the brain samples from the patients with PD and DLB[283]. In addition, experiments in hippocampal neuronal cells showed that pre-formed fibrils of αS could cross-seed the aggregation of tau[284]. The efficiency of this process depended on the conformations of the fibrils, or the type of "strain" as defined in the study, and was most efficient when using fibrils prepared by repetitive self-seeded fibrillisation of αS. The effect was identified

both in cultured neuronal cells and in mice models. Moreover, tau and αS were found to be closely associated in the resulting filaments, as determined by double-labelling immune electron microscopy.

Experiments in cell culture corroborated the *in vivo* finding that αS could be colocalised with tau[285,286]. For example, the colocalisation of αS with tau and phosphorylated tau was detected by FRET assays in human neuroglioma and mouse cortical neurons, co-transfected with αS and tau[287]. In this study, in addition to the identification of the co-localisation between the two proteins, the co-transfection was found to affect the aggregation pattern of αS in the cells, resulting in a higher number of smaller aggregates formed by αS, increase in the secretion of αS and an increase in the amount of insoluble αS. These changes, interestingly, were associated with an increase in αS cytotoxicity, and could potentially suggest the presence of direct interactions between αS and tau molecules during the aggregation process.

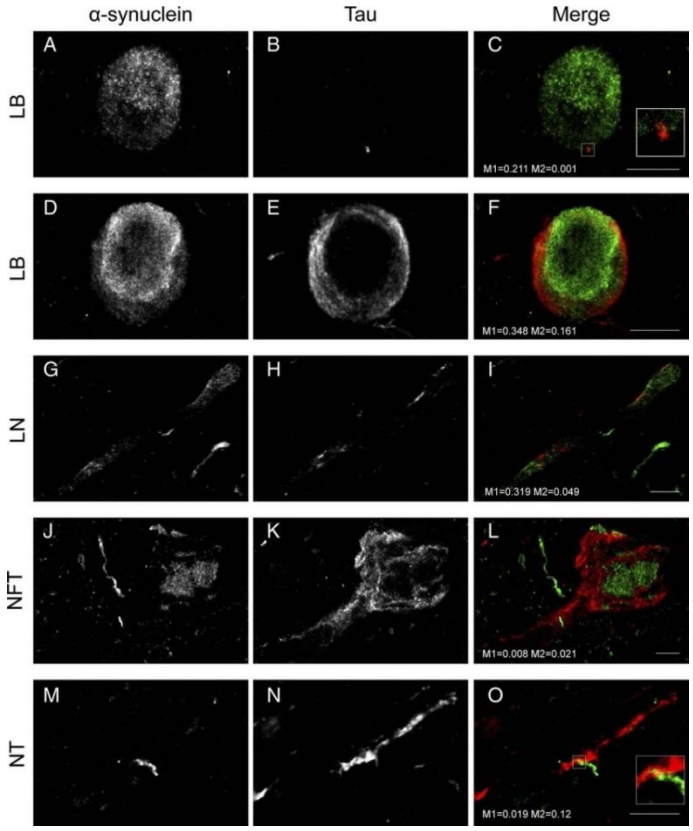

Figure 6.5. Co-aggregates of αS and tau, detected by double immunofluorescence in the brains of patients with DLB. αS is shown in green and tau is shown in red. A-F are tau-positive LBs, J-L are αS-positive NFTs, and M-O are neuropil threads. Scale bar is 10 μm. (Figure is reproduced from Colom-Cadena *et. al.*, 2013[280]).

6.1.8 Tau and αS co-interaction *in vitro*

In vitro, tau does not readily self-assemble into amyloid fibrils and requires the presence of charged polyanions such as heparin. However, it was found that its fibrillisation was promoted in the presence of αS, and that the two proteins accelerated the fibrillisation of each other[288], suggesting the presence of a direct interaction between the molecules of the two proteins in solution. In further support of this, some fibrils, formed in the presence of both proteins, were found to contain the segments of both αS and tau[288]. Furthermore, it was found that the molecules of αS and tau could directly interact. This was demonstrated by extracting tau protein from human brain lysates by αS affinity chromatography using αS-Sepharose beads[285]. Interestingly, exclusively tau was extracted by that approach, and not other cytoskeletal proteins such as tubulin, which were confirmed to be present in the analysed lystates, pointing towards a higher affinity of the binding between αS and tau than between αS and these other proteins. Further investigation of this binding was carried out in the same study using recombinant tau40, which is the longest isoform of tau consisting of 440 amino acids. It was identified that the binding epitopes comprised the NAC and C-terminal region of αS molecule (residues 55-140) and the microtubule-binding domain of tau, and that the binding was inhibited by tubulin due to its competition with αS for the binding the microtubule domain of tau (residues 192-383). The work revealed that the identified direct co-interaction between αS and tau was sensitive to the ionic strength and decreased with the increased ionic strength of buffer, and also could be inhibited upon the addition of charged polyanions such as heparin. These observations suggested the involvement of direct electrostatic interactions in this binding. In addition, in the same study, it was found that αS promoted the phosphorylation of tau[285]. Furthermore, αS pathological mutations A30P and A53T had no effect on the binding, although this result appeared contradictory since later studies reported either a decrease of the co-interaction of αS with tau due to A30P mutation[286], or an increase due to this and other disease-associated point mutations of αS[289], pointing towards the need for further studies to resolve the controversy. The point-mutation of tau found in frontotemporal dementia, P301L, was reported to prevent the tau and αS co-interaction[290]. An interesting single-molecule study, published in 2012, was carried out using fluorescently-labelled recombinant αS and tau and utilising single-molecule techniques, fluorescence correlation spectroscopy and scanning for intensely fluorescent targets[291]. In that study, mixed oligomers of tau and αS were prepared, by either combining monomeric proteins or pre-formed oligomers of tau with monomeric αS in the presence of aggregation inducers DMSO or metal ions such as Al^{3+} and Fe^{3+}. Under these conditions, the formation of mixed oligomers was observed within short time-period, over 90-100 min after mixing. Their formation was most prominent in the presence of Al^{3+} ions and absent without aggregation inducers within this time-period. These species had a broad size distribution of approximately 20-200

monomers, determined from fluorescence intensity distribution analysis, and varying proportions of both proteins depending on the added aggregation inducers[291].

6.1.9 Tau and Aβ co-interaction *in vitro*

Direct binding between tau and Aβ in solution was demonstrated for various isoforms of both proteins[292]. Even more recently, it has been shown that pre-formed fibrils of Aβ42 could cross-seed the aggregation of tau in solution, as well as in cultured cells and in mice transgenic for tau[293], suggesting that a direct co-interaction of Aβ and tau could occur.

6.2 Methods

6.2.1 Aβ peptide stock preparation

Monomeric solutions of HiLyteFluor 488 and HiLyteFluor 647-labelled Aβ40 and Aβ42 (Anaspec, Fremont) were prepared as described previously[110,294], by dissolving the lyophilised peptide in NaOH, pH 12, sonication over ice for 15 min (Bandelin Sonorex), and flash-freezing into aliquots and storage at -80°C. Initially, stock solutions were prepared by diluting the protein solutions into SSPE buffer (150 mM NaCl, 10 mM $Na_2H_2PO_4$ x H_2O, 10 mM Na_2EDTA, 0.01% NaN_3, pH 7.4) followed by serial dilutions with the same SSPE buffer, pH 7.4, to the desired aggregation reaction concentrations.

6.2.2 Aβ sample preparation for TEM imaging

Prior to the experiments, the ability of the labelled Aβ peptides to self-assemble into amyloid fibrils at pH 7.4 was confirmed by TEM imaging (Fig. 6.6), and was in agreement with the previous studies that used identical peptide preparations[110,111]. For imaging, 1:1 488:647 Hilyte Fluor Aβ40 or Aβ42 peptide solutions were prepared at 10 µM concentration and incubated for 3 d at 37°C with rotary shaking (200 rpm, New Brunswick Scientific Innova). Imaging was carried out according to the protocol described in General Methods, section 2.14. Representative results are shown in Fig. 6.6, and confirm the ability of the fluorescently-labelled peptides to assemble into amyloid fibrils.

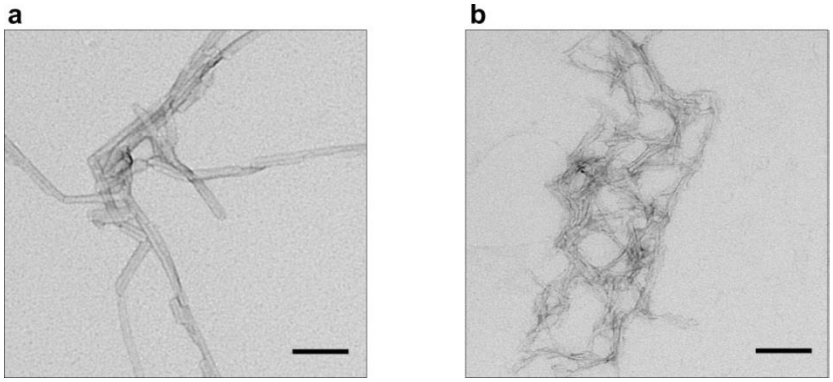

Figure 6.6. TEM images of amyloid fibrils formed by 1:1 488:647 Hilyte Fluor labelled Aβ40 (**a**.) and 1:1 488:647 Hilyte Fluor labelled Aβ42 (**b**.). Scale bar is 100 nm.

6.2.3 Aβ oligomer preparation

For the incubations, 1:1 molar ratios of 488 and 647-labelled samples were used, either 488:647 Aβ40 or 488:647 Aβ42 for the self-aggregations, or 488 Aβ40:647 Aβ42 for the mixed aggregations. Three separate samples for each concentration (0-250 nM of total Aβ) and protein combination were prepared. LoBind microcentrifuge test-tubes (Eppendorf, Hamburg, Germany) were used for all incubations to prevent surface absorption, as was found to be effective in previous studies[83,115,156,295]. Incubations were performed for 3 d at 37°C with rotary shaking (200 rpm, New Brunswick Scientific Innova), and the samples were subsequently analysed using single-molecule TCCD.

6.2.4 αS and tau k18 oligomer preparation

AF488 and AF594 labelled αS A90C was used, and AF488 and AF594 k18 construct of tau with a His_6-tag in N-terminus (kindly provided by Dr. Y. Ye). Samples were prepared and incubated according to the same protocols as described for Aβ.

6.2.5 Sample preparation for CAC measurements

For the critical aggregation concentration (CAC) measurements using fibril disaggregation of Aβ, fibrils were first prepared by 72 h incubation of 10 µM solutions of singly-labelled Aβ peptides, either 488 Aβ40, or 647 Aβ40, and 10 µM 488 Aβ42 or 647 Aβ42, pH-adjusted to 7.4 and incubated under the same conditions as above. Pelleting was carried out by centrifugation at 12,800 x g for 15 min, followed by two identical washing steps involving removal of the supernatant,

washing of the pellet and additional centrifugation for 5 min. Finally, the pellet was re-suspended in fresh pH 7.4 SSPE buffer, by adding 100 µL buffer to ensure the excess of fibrillar material. The resulting samples were incubated under quiescent conditions at 37°C for 3 d, and centrifuged for 15 min at 12,800 x g prior to measurements. For the confirmation of equilibrium past 3 d, identical samples were incubated for longer (7 d), yielding agreeable results.

Fibrils of αS were prepared by incubating 70 µM AF-488 labelled αS for 7 d with shaking (under the same conditions as for the sm-FRET experiments, as detailed in section 2.4). Pelleting and washing were performed similarly to Aβ samples. Fibrillar pellets were resuspended in fresh Tris buffer (100 µL) ensuring the excess of fibrillar material. The resulting samples were incubated under static conditions at 37°C for 3 d, and centrifuged for 15 min at 12,800 x g prior to measurements.

6.2.6 TCCD measurements of oligomers

TCCD with dual laser excitation in 488/633 nm mode was performed for the measurements of Aβ solutions, and in 488/594 nm mode for the measurements of αS or k18 solutions. For the measurements, dual-labelled protein samples were diluted in SSPE or Tris buffer (depending on which buffer was used for incubations) up to 100 pM concentration suitable for the single-molecule analysis and TCCD measurements were performed according to the procedure described in General Methods, section 2.11. For each solution, data were acquired for 600 s, with 100 µs bin-width, 100,000 bins per frame and a total of 60 frames. The analysis was carried out as described in General methods, section 2.12. The fraction of coincident events was estimated according to:

$$Q = \frac{C - E}{A + B - (C - E)} \tag{6.1}$$

where A is the number of fluorescent bursts in the blue channel above the 15 photons bin^{-1} threshold, B is the number of fluorescent bursts in the red channel, C is the number of coincident events, and E is the number of chance-coincident events. The approximate oligomer concentration was calculated as the fraction of coincident events (oligomers) multiplied by the starting total protein concentration.

6.2.7 Measurements of fluorescently labelled oligomers of Aβ in the presence of unlabelled Aβ protein

These experiments were carried out in order to determine whether the presence of unlabelled Aβ peptide had an effect on the formation of fluorescently dual-labelled oligomers. This was done by

preparing the samples according to the protocol used for the preparation of oligomeric Aβ samples in buffer, but with the addition of unlabelled Aβ prior to incubation. The initial concentration of the unlabelled Aβ stocks was determined using BCA protein assay kit (Thermo Fisher Scientific), following the manufacturer-provided protocol.

6.2.8 CAC measurements and analysis

These measurements were performed to determine the total concentration of soluble protein released from the fibrils into buffer solution upon prolonged incubations. This was done by relating the burst counts of the measured soluble supernatants to the burst counts from a DNA standard of precisely known concentration. Data were acquired using the same single-molecule setup as for the TCCD measurements. Single-colour illumination was used, either 488 nm for the measurement of 488-labelled samples, or 633 nm for the measurements of 647-labelled samples. In the case of a dual-labelled DNA standard, data were acquired by exciting with one colour, and subsequently with another colour in the next recording. The measurements were stationary, with solutions placed on a glass coverslide and focussing the laser beam 10 µm into the solution. Data were acquired for 200 s with 1 ms time-bins (chosen according to the expected residence time in the confocal volume at these conditions[114]), 8,000 bins per frame and a total of 25 frames.

Initially, a calibration curve was recorded using a dual-labelled 40 base pair DNA duplex, generated from double-HPLC purified complementary synthetic oligonucleotides (AtdBio) with the following sequence:

AF488-TAGTGTAACTTAAGCCTAGGATAAGAGCCAGTAATCGGTA
AF647-TACCGATTACTGGCTCTTATCCTAGGCTTAAGTTACACTA

The DNA duplex was formed by heating a 1:1 mixture of oligonucleotides (1 µM) to 95°C followed by slow cooling to room temperature, analogous to previously described protocol[114] (section 5.2.4). Calibration was made with the reference to a triplicated measurement of the DNA standard, diluted in SSPE buffer at a range of concentrations, which resulted in a linear increase in the numbers of fluorescence bursts above a chosen threshold (10 photons bin^{-1}) with sample detection concentration (0-250 pM). The resulting calibration curve is shown in Fig. 6.7.

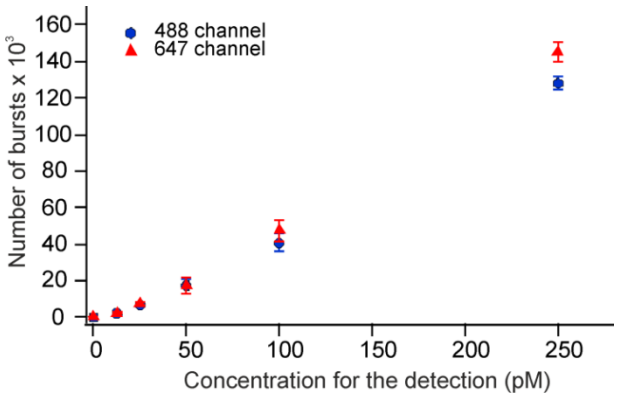

Figure 6.7. Calibration curve resulting from the measurements of 40 base pair DNA standard at a range of concentrations (n=3, std). It shows a linear increase in the number of bursts above a fixed threshold of 10 photons bin^{-1} with the increase in the concentration of the sample.

Subsequently, the supernatants collected from the fibrillar samples were diluted in SSPE (serial dilution) by a factor of 8×10^3 and measured as described. The number of bursts above the same threshold as for the standard (10 photons bin^{-1}) was counted and converted to the detection concentration, and subsequently to the bulk concentration using the dilution factor. The results are summarised in Table 6.1. in the Results section. Additionally, it was found in control measurements that comparable numbers of bursts were obtained from the samples after 3 and 7 d of incubation, confirming the equilibration past 3 d.

6.2.9 Additional CAC measurements, using HiLyte Fluor-labelled DNA oligonucleotide

Double-HPLC purified synthetic oligonucleotide was used (AtdBio) with the following sequence: HiLyte Fluor 488-TAGTGTAACTTAAGCCTAGGATAAGAGCCAGTAATCGGTA. Calibration curve in the 488 (donor) channel was recorded, by noting the manufacturer-provided initial concentration of the oligonucleotide. Calibration curve was generated from triplicated measurements of the oligonucleotide at a range of concentrations. Single-colour illumination was used, and solutions were excited with 488 nm laser beam. For each sample, data were acquired for 400 s under a constant flow of 1 cm s^{-1}, using 100 µs bin-width, 100,000 bins per frame and a total of 40 frames. For the burst selection in the blue channel, a threshold of 15 photons bin^{-1} was applied. It was verified that under these detection conditions, discrete bursts could be obtained for up to 30 pM concentration of the analysed 488-labelled solution, and increase as a function of the concentration, as shown in Fig. 6.8.

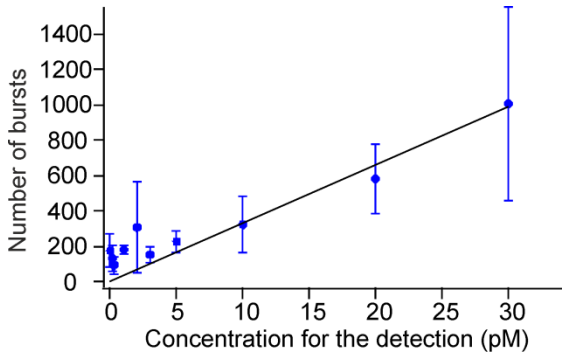

Figure 6.8. Calibration curve resulting from the measurements of HiLyte Fluor 488-labelled synthetic oligonucleotide under flow, using a threshold of 15 photons bin^{-1} for the selection of bursts (n=3, std). The results were fitted to a straight line giving $y = 0 + 76.95x$ (R^2=0.95).

Once the calibration plot was generated, supernatants of various 488-labelled protein samples were analysed with the reference to this plot. In all cases, the sample preparation was the same as for the static CAC measurements described in section 6.2.8. Multiple samples were analysed in analogous way as in the previous CAC experiments. Firstly, the numbers of collected bursts above the threshold of 15 photons bin^{-1} were converted to single-molecule concentrations using the straight-line equation derived from the calibration (Fig. 6.8). Secondly, the single-molecule concentrations were converted to the bulk concentrations by dividing by the known dilution factor, which was typically 1×10^{-4}, or in some cases 2×10^{-4}, which ensured burst separation. Representative intermediate results of this conversion are shown in Table 6.3 (Results), and final derived CAC values are listed in Table 6.4 (Results). Since the precision of the resulting CAC values in this approach depends on the quality of the generated calibration curve, the quality of this curve may be improved by recording more datapoints and increasing the number of repeats in order to decrease the error associated with these measurements.

6.2.10 TCCD chance coincidence controls using free dyes in solution

To confirm that the TCCD experiments were probing the specific interaction between protein molecules rather than a random association of the fluorescent dyes, control measurements were performed using pairs of free fluorescent dyes in solution.

The free unbound dyes were prepared according to a previously published protocol[134], by reacting 5 mM of AF488 NHS ester (Succinimidyl ester) or 5 mM of AF647 NHS ester with Tris.HCl (pH 7.2, 250 mM, 300 µL) at room temperature for 3 h. The solutions were then further diluted with Tris buffer, aliquoted and stored at –80°C.

For the experiments, 1:1 molar ratio of AF488 and AF647 were combined at a total concentration of either 2 μM or 0.5 μM, by diluting the concentrated dyes into Tris buffer with 1% NaN_3. Five separate samples were prepared per concentration. The samples were recorded immediately after the preparation, and then following a 72-h incubation at the same incubation conditions as for the protein samples. For the detection using TCCD, the samples were diluted into Tris buffer to 100 pM concentration, and recorded under flow using the same procedure and settings as for the detection of protein samples. As positive controls, the samples of dual-labelled αS were also recorded. The data were analysed in the same way as the data recorded using the fluorescently-labelled proteins (detailed in sections 2.12 and 6.2.6). Subsequently, two parameters were assessed, the coincidence coefficient (eq. 6.1) and the overall number of detected coincident events, and the results are in Table 6.5 (Results).

6.3 Results

6.3.1 TCCD measurements of self- and co-oligomers

To measure the steady-state populations of oligomers, equimolar ratios of monomeric Aβ, αS or tau fragment k18 singly labelled with a 488-fluorophore were combined with monomeric peptides singly labelled with a 647 (or 594)-fluorophore in aqueous buffer, using a range of low total protein concentrations which are close to the natural abundance of the proteins. The solutions were left for 72 h at 37°C until a steady-state population of oligomers and monomers was generated in each case. As the monomeric peptides self-associate to generate oligomers, they can be distinguished from the excess of monomers by the criteria of coincidence and quantified by TCCD (eq. 6.1), as described in Methods section and in the General Methods chapter, sections 2.11 and 2.12.

The resulting plots of oligomer populations versus the total starting protein concentrations are shown in Fig. 6.9 for the self-oligomerising systems. Even though the fluorescent dye pairs were varied (either 488/647 or 488/594) in these TCCD experiments, the relative comparison between the results is possible because in each case, the data were internally normalised to the corresponding monomeric burst rates. It is interesting to note that Aβ40 yielded the highest steady-state concentration of oligomers, followed by αS and Aβ42, whereas k18 formed only low amount of oligomers. This latter result is consistent with the established property of this protein to be aggregation-incompetent in aqueous buffer in the absence of aggregation inducers. In Fig. 6.10, the results of co-oligomerisation experiments are shown, where stoichiometric amounts of two different proteins bearing different fluorescent dyes were combined for the same experiment as in Fig. 6.9, and co-oligomers containing both types of proteins were detected. The result suggests that for all recorded protein combinations, the co-oligomeric species were formed in low abundance, below 10 nM in all cases. The control

experiments using free dyes in solution, shown in Fig. 6.10e, suggest that even though the total amount of the detected co-oligomers was low, it was nevertheless above the signal purely arising from free fluorescent probes, thus confirming the formation of these co-oligomeric species under the chosen incubation conditions.

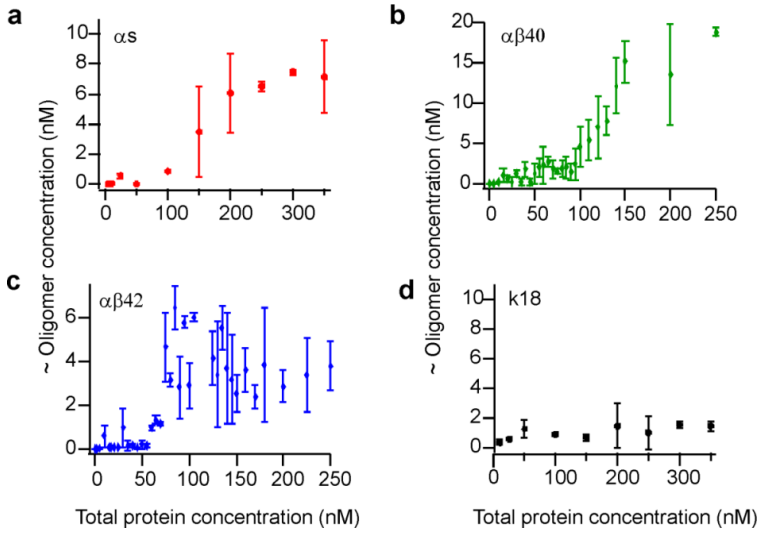

Figure 6.9. Self-oligomers of αS, Aβ40, Aβ42 and tau k18, recorded by TCCD after 3 d incubation at a range of total starting protein concentrations (n=3, std), with 600 s detection time per sample.

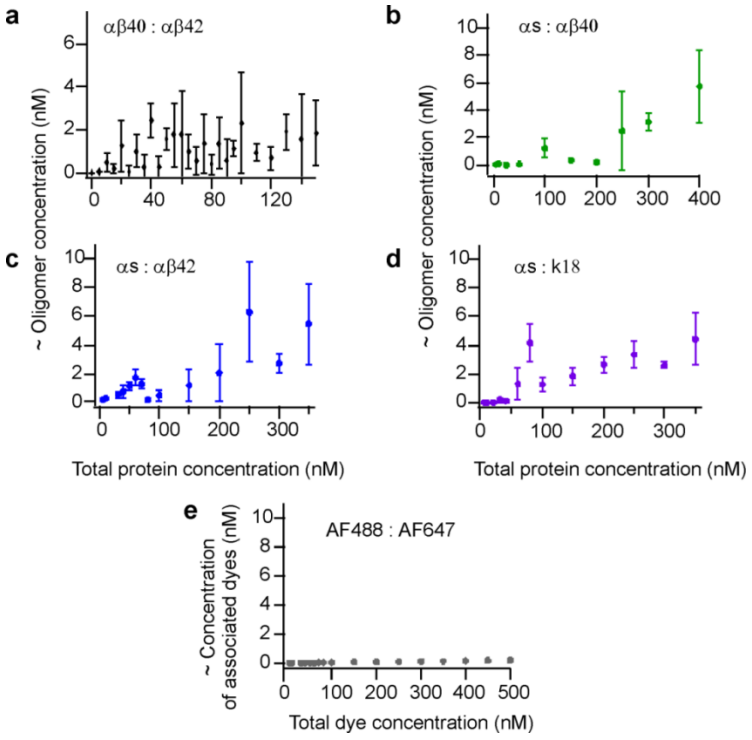

Figure 6.10. Co-oligomers of Aβ isoforms (**a.**) and co-oligomers of αS with Aβ40 (**b.**), Aβ42 (**c.**) and tau k18 (**d.**), recorded by TCCD after 3 d incubation at a range of total starting protein concentrations (n=3, std), with 600 s detection time per sample. In addition, TCCD control results are shown (**e.**) In these controls, the signal from free dyes in solution was monitored following sample incubations at the same incubation conditions as for the protein samples, and the same analysis was performed.

6.3.2 Control measurements for the confirmation of steady state in the Aβ oligomeric samples

In the TCCD analysis of the populations of self- and mixed oligomers, the protein samples were measured after 3 d incubation with agitation, as has been described in Methods. In order to verify that this time period was sufficient for the attainment of steady-state, control measurements were carried out after longer incubation time, past 7 d. The resulting Q values and the numbers of coincident events were compared to the results from the same samples after 3 d, and found to be in agreement. The representative results for Aβ isoforms are shown in Table 6.1.

Table 6.1. Results of control TCCD measurements of Aβ oligomeric samples after incubation over 3 d and 7 d, at the starting protein concentrations of 10 nM and 100 nM.

Sample type	Average %Q (n=4)	std %Q	Number of events (n=4)	std
Aβ 40, 10 nM, 3 d	1.78	0.18	279	88
Aβ 40, 100 nM, 3 d	3.05	0.42	1025	660
Aβ 40 : Aβ 42, 10 nM, 3 d	8.54	4.59	5097	3346
Aβ 40 : Aβ 42, 100 nM, 3 d	5.84	0.70	1484	246
Aβ 42, 10 nM, 3 d	0.95	0.13	259	120
Aβ 42, 100 nM, 3 d	0.34	0.32	128	86
Aβ 40, 10 nM, 7 d	0.53	0.16	107	45
Aβ 40, 100 nM, 7 d	4.48	0.35	1662	686
Aβ 40 : Aβ 42, 10 nM, 7 d	4.95	0.17	1622	507
Aβ 40 : Aβ 42, 100 nM, 7 d	3.21	0.58	855	97
Aβ 42, 10 nM, 7 d	1.06	0.02	151	9
Aβ 42, 100 nM, 7 d	0.28	0.08	69	37

6.3.3 Measurements of fluorescently labelled oligomers of Aβ in the presence of unlabelled Aβ peptide

These experiments were carried out in order to determine whether the presence of unlabelled Aβ40 peptide had an effect on the formation of fluorescently dual-labelled oligomers. The result, shown in Fig. 6.11., suggests that more oligomers could be detected in the presence of unlabelled peptide. This can be either due to higher stability of the labelled species in the presence of unlabelled peptide, or because more oligomers were formed under these conditions.

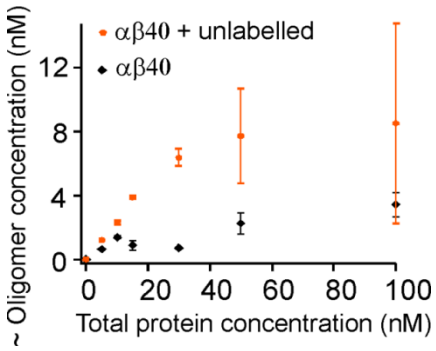

Figure 6.11. TCCD measurements of Aβ40 oligomers after the incubation in the presence or in the absence of unlabelled monomeric Aβ40 at 5 μM (n=3, std).

6.3.4 Measurements of fluorescently labelled oligomers and co-oligomers in the presence of either labelled or unlabelled fibrils

In these experiments, oligomer measurements were carried out by TCCD in the presence of various combinations of either labelled or pre-formed unlabelled fibrils of αS, or Aβ isoforms in order to check whether co-oligomers could be formed under these conditions as well as upon combining monomeric proteins in solution. The results are summarised in Fig. 6.12 and confirm co-oligomer formation under these conditions. Note that the results are presented as Q (eq. 6.1) and not converted into approximate oligomer concentrations due to unknown concentration of the total soluble protein in the experiment, which would need to account for the unknown concentration of monomer released from fibrils in the presence of another soluble protein. Nevertheless, this result demonstrates that co-oligomers can be formed and detected upon incubation of soluble protein with pre-formed fibrils of another isoform. This is interesting because the solid aggregates of either protein are found in the disease and monomeric protein is naturally present, suggesting that similar stable co-oligomeric species could also be formed.

6.3.5 Results of CAC measurements

Experiments were performed in order to estimate the concentration of soluble Aβ or αS released from pre-formed fibrils of either protein into aqueous buffer following prolonged incubation. This concentration corresponded to the critical aggregation concentration (CAC) of the proteins. When the monomer concentration is below the CAC, most of the protein molecules are expected to be monomeric, whereas above the CAC, most molecules are expected to be within aggregates. Thus, CAC is the minimum protein concentration in solution that is required for the fibrillisation to occur.

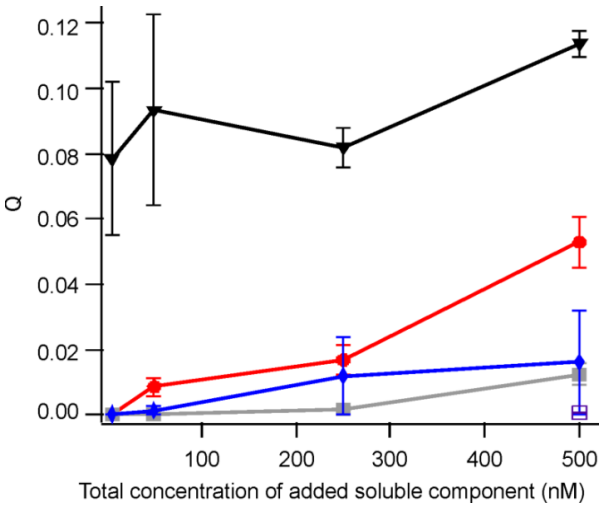

Figure 6.12. Association coefficients (Q), measured after combining pellets of either Aβ or αS with monomeric proteins, followed by an incubation under static conditions for 3 d. Black triangles: 488- and 594-labelled αS fibrils + unlabelled Aβ42. Red circles: 488-Aβ42 fibrils + 594-αS monomer. Grey squares: 488-Aβ42 monomer + 594-αS fibrils. Blue diamonds: 488-Aβ40 + 594-αS monomer (n=3, std). As controls, fluorescent dyes were measured after incubation at a 1:1 stoichiometric ratio and the total concentration of 500 nM for 3 d.

The experimental approach is fully described in Methods (sections 6.2.5-6.2.8), and the resulting CAC values are summarised in Table 6.2. CAC for Aβ isoforms was measured to be 94 ± 37 nM for Aβ40, and 28 ± 4 nM for Aβ42 at pH 7.4. The value for Aβ40 is in good agreement with the previously reported result of 100 nM at pH 7.4[296], and the value for Aβ42 is lower than a previously reported value of 0.2 µM at pH 8[297], consistent with a reported decrease in CAC with lowering the pH[296]. This gives values of the free energy for fibril formation as $\Delta G^{\circ(fib)}_{42,42}$ = -44.8 ± 0.4 kJ mol^{-1} for Aβ42 and $\Delta G^{\circ(fib)}_{40,40}$ = -41.7 ± 1.1 kJ mol^{-1} for Aβ40. The result for Aβ40 is within the range of previously reported values for the unlabelled peptide[298,299], which were -37.7 kJ mol^{-1} and -46.7 kJ mol^{-1}, indicating that the presence of the fluorophore labels at the N-terminus does not substantially alter the free energy of fibril formation. Lower CAC values measured for Aβ42 isoform relative to Aβ40 isoform suggest that Aβ42 fibrils disaggregate to a lesser extent than fibrils of Aβ40. This observation implies that the Aβ42 fibrils are more stable than their Aβ40 counterparts, correlating well with previous reports of Aβ disassembly and stability[300,301]. The resulting CAC for αS was 0.7±0.2 µM, which is lower than an earlier reported value, 28 µM, measured using quantitative amino acid analysis[104]. It is closer to a more recently reported value of ca. 2.7 µM, which was obtained from absorption measurements of the concentrations of denatured supernatants and subsequent extrapolation to the situation exploring the absence of denaturant[105].

To note, CAC values are expected to vary depending on the conditions at which the protein is incubated such as, for example, the presence or the absence of lipid membranes, pH and ionic strengths, therefore any absolute CAC values derived in these experiments are expected to be specific to the chosen incubation conditions.

Table 6.2. Results of the measured concentrations of supernatants above fibrillar pellets. Calibration to AF488 and 647 dual-labelled 40 base pair DNA duplex.

Protein	Average number of bursts (n=6)	std (n=6)	[SM] (pM)	std ([SM])	[Bulk] (nM)	std ([Bulk])
Aβ40-488	2370	1316	12.7	7.1	102	57
Aβ40-647	2198	1189	10.6	5.7	85	46
Aβ42-488	689	127	3.65	0.6	29.2	4.8
Aβ42-647	673	181	3.25	0.85	26	6.8
αS-488	1349	351	7.3	1.8	730	200

6.3.6 Results of additional CAC measurements using HiLyte Fluor-labelled oligonucleotide

The above CAC measurements were carried out using dual-labelled DNA standard bearing AF fluorescent dyes. While the samples of αS were labelled with AF fluorophores, Aβ peptides used for the preparation of fibrillar samples were labelled with Hilyte Fluor dyes. Therefore, it was set out to check whether the differences in the fluorescent tags affected the outcome of these experiments. In addition, previous CAC measurements were stationary, whereas the confocal setup in principle allows the detection under laminar flow, by utilising microfluidics[114]. In order to check whether these factors significantly affected the resulting values, additional control CAC measurements were carried out, where a DNA single strand labelled with HiLyte Fluor 488 was used as a standard, and the detection under flow was implemented for both the generation of the calibration curve as well as the measurements of the supernatants collected after the incubation of 488-labelled protein fibrils in buffer.

The new calibration curve was generated as described in Methods, section 6.2.9, and the protein samples were re-measured and re-analysed to derive CAC values. The results are summarised in Tables 6.3 and 6.4.

Table 6.3. Results of the conversion to derive bulk CAC values using the calibration to HiLyte 488 oligonucleotide.

Protein	Average number of bursts (n=3)	std (n=3)	[SM] (pM)	std ([SM])	[Bulk] (nM)	std ([Bulk])
Aβ40-488, 3 d	859	389	11.16	5.055	111.6	50.55
Aβ40-488, 7 d	1268	429	16.478	5.575	167.8	55.75
αS-488, 3 d	5665	418	73.619	5.43	736.2	54.3
αS-488, 7 d	6942	2070	90.2	26.9	902	269

Table 6.4. Summary of the resulting average CAC values derived from the measurements of the supernatants above fibrillar pellets under flow, with the calibration to HiLyte 488 oligonucleotide.

Protein	[Bulk] (n=6) (nM)	std (nM)
Aβ40-488, 3 d	93	26
Aβ40-488 + 300 nM unlabelled Nb3, 3 d	517	402
αS-488, 3 d	652	62
Aβ40-488, 7 d	318	271
αS-488, 7 d	1792	238
Aβ42-488, 7 d	162	25
αS-488 + 300 nM unlabelled Aβ42 , 3 d	557	28

From the results in Table 6.4, the CAC value for Aβ40-488 after 3-d incubation is in good agreement with the corresponding value from the stationary measurement, 93±26 nM and 102±57 nM, respectively. Similarly, there is consistency between the previously measured value of 700±200 nM and the currently obtained 652±62 nM for αS-488 after 3-d incubation. Therefore, it can be concluded that in these experiments, there was no substantial difference in the results depending on whether AF or HiLyte Fluor fluorescent probes were used to tag the standard used for calibration, and whether the data were acquired using a stationary measurement or under continuous flow. The main requirements for this approach to measure CACs were to achieve conditions which would allow the acquisition of discrete fluorescence bursts, and to ensure that the relative comparisons were made between the datasets acquired and analysed using identical settings. Overall, the resulting consistency in the CAC values derived using two independent sets of experiments validates the measured CAC values under the chosen incubation conditions. In addition to the results obtained after 3-d incubation, Table 6.4 includes the results following the incubation for one week. From these results, the derived CAC values after this longer time period are higher, however, still within the sub-micromolar (or low-micromolar for αS) range.

Furthermore, it was attempted to incubate fibrils in the presence of an unlabelled antibody in order to check whether this lead to any noticeable differences in the resulting CAC values. The addition of 300 nM of unlabelled nanobody specific to Aβ40, Nb3 (provided by Dr. E. De Genst), to the labelled fibrils of the peptide resulted in a much higher variation in the obtained CAC values (Table 6.4). This variability can be either due to a possible involvement of this Nb in the disassembly of fibrils, or, alternatively, due to the increased sample sticking during the detection. Because Nb3 is known not to bind fibrils of Aβ, the latter explanation is likely to be dominant, particularly because it has been observed that the addition of unlabelled Nbs in these experiments generally resulted in higher stickiness of the labelled samples, thus making the results less reproducible. The addition of 300 nM of unlabelled Aβ42 peptide to the labelled fibrils of αS did not lead to any effect on the measured CAC values, suggesting that the presence of the peptide in this case did not affect the disassembly of αS fibrils.

6.3.7 TCCD chance coincidence controls using free dyes in solution

Control TCCD measurements were carried out to quantify the association resulting from free dyes in solution, as detailed in Methods, section 6.2.10. From the results summarised in Table 6.5, the %Q values (Q derived using eq. 6.1 x 100) and the numbers of coincident events for the free dyes in solution were low and constant over time. To note, for the samples of αS, both the %Q values and the numbers of coincident events were low at the start of the incubation, indicating the presence of only a small number of aggregates, and increased after the incubation due to the formation of more aggregates. Therefore, it can be concluded that the low and constant %Q and the number of coincident events obtained from the free dyes in buffer indicated that these dyes did not assemble during the incubation reaction.

Table 6.5. Results of the TCCD chance coincidence control experiments.

Sample type	Average %Q	std %Q (n=5)	Number of events	std (n=5)
buffer	0	0	0	0
Dyes, 0.5 µM, 0 h	0.035	0.012	7	3
Dyes, 0.5 µM, 72 h	0.052	0.056	8	7
Dyes, 2 µM, 0 h	0.0357	0.034	9	9
Dyes, 2 µM, 72 h	0.017	0.0099	3	2
αS, 0.5 µM, 0 h	0.311	0.375	24	20
αS, 0.5 µM, 72 h	1.76	0.267	225	111
αS, 2 µM, 72 h	0.917	0.291	146	97

6.3.8 Apparent oligomer size distributions from TCCD

In the TCCD experiments, the apparent sizes of the recorded oligomers were estimated from fluorescence intensities according to the following relation:

$$Apparent\ \ size = \left(\frac{I_{blue}}{I_{blue monomer}} + \frac{I_{red}}{I_{red\,monomer}} \right) \tag{6.2}$$

where I_{blue} is the oligomer fluorescence intensity in the 488- channel, $I_{blue\ monomer}$ is the average monomer intensity in the same channel, I_{red} is the oligomer fluorescence intensity in the 647- (or 594-) channel, $I_{red\ monomer}$ is the average monomer intensity in the 647 (or 594) channel.

Similarly to the apparent sizes derived from sm-FRET experiments, the apparent size distributions in this case are termed 'apparent' and are likely to be not discrete and broadened, owing to the differences in the paths that the detected aggregates can take through the confocal volume, the inhomogeneous laser excitation of the sample, the stochastic nature of fluorescence emission as well as FRET between the dye pairs, and fluorescence quenching in higher-order oligomers. However, fluorescence quenching was previously demonstrated not to be significant for the oligomers of Aβ up to 20-mers[160].

In principle, because only dual-coloured aggregates are detected in the TCCD experiment, whereas singly-coloured species can also be formed, a binomial correction could be introduced after the analysis in eq. 6.2. In this case, the number population of each apparent size group would be multiplied by a correction factor from the Pascal's triangle, as has been done for the apparent size distributions in the earlier single-molecule studies[110,111]. However, more recently a detailed theoretical study was carried out in this laboratory, which further confirmed that the size estimation based on fluorescence intensities in the confocal experiments indeed does not allow discrete estimation of oligomer sizes[158], reinforcing the originally introduced term 'apparent'. Therefore, because of the limitations in resolving individually sized oligomer sub-populations using this method, the binomial correction of the apparent size histograms in this work was not introduced, and only the distributions derived using eq. 6.2 were presented.

Despite the fact that the TCCD-derived apparent size distributions do not represent the precise physical sizes of the studied oligomers due to the above mentioned limitations, they do contain useful qualitative information about the changes in the sizes of oligomers. For example, the size evolution of the analysed species can be observed through the broadening of the apparent size distributions, as has been illustrated for the apparent size distributions at different timepoints during the time course of the aggregation reaction of αS, as was shown in Fig. 3.11. In addition, the apparent size histograms

resulting from different protein samples can be compared to determine whether the overall shapes and the mean values of these distributions are different. Representative histograms, derived from TCCD experiment for Aβ, αS and dual-labelled DNA samples are shown in Fig. 6.13.

In Fig. 6.13, the apparent size distributions of Aβ oligomers are similar to the apparent size distributions derived from the samples of αS, and are in all cases mostly below 5-mers. Fig. 6.13b shows the resulting apparent size distribution for a model system, consisting of dual-labelled DNA molecules in the excess of a 1:1 molar ratio of free fluorescent dyes to mimic the presence of dimers in the excess of monomeric protein. The distribution is peaking at dimers and trimers rather than only at dimers, which is due to the previously mentioned expected broadening of the fluorescence signal used to derive these distributions.

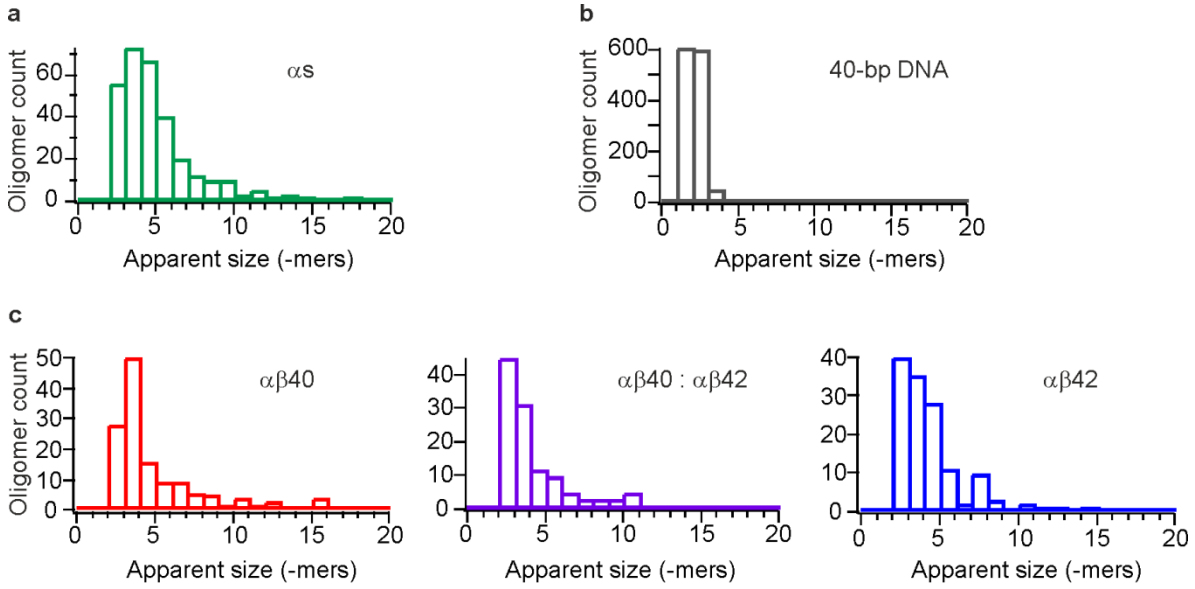

Figure 6.13. Apparent size distributions derived from TCCD experiment, using eq. 6.2. **a.** αS sample at 500 nM concentration after 72 h of incubation with agitation. **b.** Dual-labelled 40 base pair DNA duplex, diluted into 1:1 mixture of AF488 and AF647 fluorescent dyes in order to mimic a dimer in the excess of monomer. **c.** Aβ samples at 20 nM concentration after 72 h of incubation with agitation.

6.3.9 Apparent oligomer size distributions from TIRFM imaging

TIRFM imaging experiments were performed using Aβ samples in order to confirm that the apparent size populations using this method were similar to the ones derived from the confocal TCCD experiments, as was previously found for the oligomers of αS (Fig. 3.13). To achieve this comparison, samples containing 1:1 molar ratio of 488-labelled Aβ40 and 647-labelled Aβ42 were prepared at the total concentration of 20 nM, which is expected to be below the CAC for either peptide, and incubated under the same conditions as for the TCCD measurements. TIRFM imaging and data analysis were

carried out according to the same experimental protocols as what was described in section 3.2 for the samples of αS. The resulting apparent size populations of these species are shown in Fig. 6.14, together with the results from TCCD experiments. Once the histograms of the apparent size populations derived by either method were presented as probability densities, they overlapped (Fig. 6.14b), demonstrating good agreement between the two employed methods. These results are consistent with the previously reported experimental results from this laboratory, using the same methods and the oligomers of Aβ40[111]. The sizes in both TIRFM and TCCD experiments are termed apparent and serve only as estimates. It was additionally attempted to derive more precise size populations by TIRFM, using photobleaching with fluorescence step-counting, by imaging 1:1 AF488 and AF647-labelled oligomer samples. In these preliminary trials, up to 3 bleaching steps in either fluorescence channel could be clearly observed, indicating that this method is able to detect oligomers of up to 6-mers. These preliminary attempts can be extended in the future.

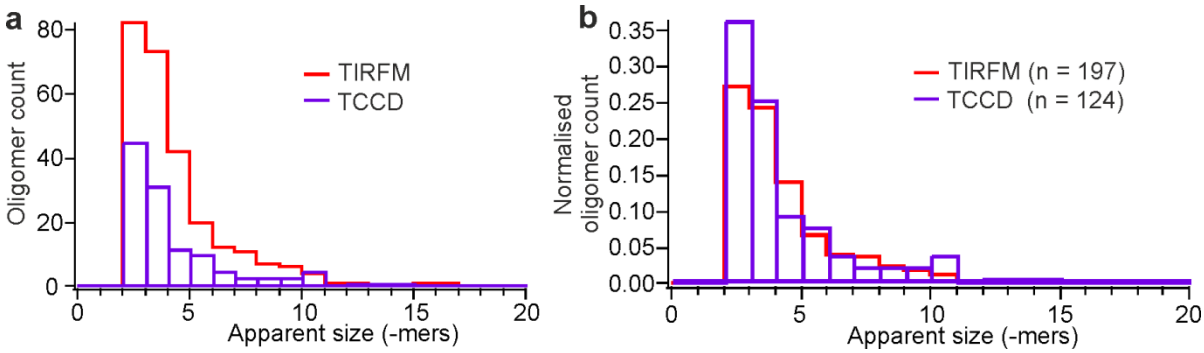

Figure 6.14. Comparison of the apparent size distributions of Aβ40 : Aβ42 co-oligomers, formed over 72 h of incubation with agitation. **a.** Overlaid raw apparent size histograms. **b.** The histograms are normalised to the total oligomer counts to highlight the similarity of the results derived by either method.

6.3.10 Results of theoretical modelling of self- and co-oligomer datasets of Aβ isoforms to determine and compare the free energies of oligomer formation

Since the recorded datasets of self- and co-oligomer formation, presented in section 6.3.1, were the most comprehensive for Aβ peptides, these data were used for theoretical analysis. The statistical mechanical model for the self- and co-oligomer formation at equilibrium was developed and implemented by Dr. G. Garcia and A. Dear, and has been detailed in Iljina *et. al.*, 2016[302]. The main assumptions of the model and the key results following its application to the datasets of steady-state oligomer populations will be described below.

In the theoretical model, the key parameter describing the oligomerisation process was the Gibbs free energy, $\Delta G°$, released upon adding two monomers together to form a new intermolecular interaction. The oligomers were treated as simple non-interacting one-dimensional chain structures with nearest-neighbour interactions independent of the chain length, as is schematically illustrated in Fig. 6.15a. The assumption of one-dimensional chain structures was considered to be valid since both self- and co-oligomers formed under the chosen experimental conditions were inferred to be mostly dimeric, and therefore the contribution from larger oligomers was not expected to strongly perturb this analysis. The directly measured size distributions of the oligomers, shown in Figs. 6.13 and 6.14, confirmed that the formed species were mostly small. However, the fluorescence-derived size distributions are likely to be broadened and do not allow the determination of discrete physical sizes of oligomers, as has been previously discussed.

In the model, for an aggregation process, the following relationship was identified: $e^{\Delta G°/(kT)} = c/c_0$ with a CAC c for a standard concentration c_0 of 1 M. The nature of the aggregates present at equilibrium was expected to depend strongly on the initial concentration of the monomeric peptides. When the monomer concentration was below the CAC, the majority of the peptides in the system were expected to be present in monomeric states and only a few aggregates to be formed consisting of a small number of monomers. In contrast, above the CAC, most molecules were expected to be present as aggregates. These aggregates could be either oligomers or fibrils. Because these species are known to differ in morphology and structure, two separate $\Delta G°$ values were allowed in order to separately describe both the oligomeric and fibrillar states, $\Delta G°^{(oligo)}$ and $\Delta G°^{(fib)}$. At low concentrations, below the CAC, the formation of large aggregates was expected to be suppressed, and the majority of aggregates to be oligomeric. At the total concentration reaching the CAC, the majority of monomers would be sequestered into fibrillar forms, and the concentration of oligomers would be expected not to increase even upon increasing the total peptide concentration. Therefore, based on the developed model, it was expected to observe an initial increase in the concentrations of oligomers with the increase in the total starting protein concentration, controlled by the free energy of oligomer formation $\Delta G°^{(oligo)}$. Once the total peptide concentration reaches the CAC, $c_0 e^{\Delta G°^{(fib)}/(kT)}$, it was expected to observe a plateau in the concentration of oligomers, controlled by the free energy of fibril formation $\Delta G°^{(fib)}$. The total protein concentration at which the oligomer concentration reaches a plateau was expected to correspond to the fibril CAC.

Once established, the model was fitted to Aβ oligomer datasets, and the fitted results are shown in Fig. 6.15b. From these results, the similarity in the slopes of the growth regions below the CAC of the Aβ40 and Aβ42 self-oligomerising systems suggests that there is no large difference in the mean free energy of oligomerisation in both cases. By fitting the model to the self-oligomerising systems, the

free energy of oligomerisation for Aβ40, $\Delta G^{\circ(oligo)}_{40,40}$, was determined to be -36.3 ± 3.0 kJ mol^{-1}, and similarly $\Delta G^{\circ(oligo)}_{42,42}$ for Aβ42 was -36.3 ± 3.2 kJ mol^{-1}. The CAC for Aβ40 was estimated as 222 ± 10 nM by the same fitting procedure, and the CAC for Aβ42 was estimated as 86 ± 10 nM. These values allow independent estimation of $\Delta G^{\circ(fib)}_{40,40}$ as -39.5 ± 0.1 kJ mol^{-1} and $\Delta G^{\circ(fib)}_{42,42}$ as -42.0 ± 0.3 kJ mol^{-1}, demonstrating broad consistency with the direct measurements, described in sections 6.3.5 and 6.3.6 (Fig. 6.15c). The value of $\Delta G^{\circ(oligo)}_{40,42}$ was estimated to be -32.6 ± 2.6 kJ mol^{-1}, and the absence of apparent plateau in the co-oligomer plot was consistent with both isoforms being present below their CAC values. Crucially, according to this analysis the resulting free energies of oligomerisation were large and negative, suggesting that both self- and co-oligomers could be formed with comparable free energy penalty.

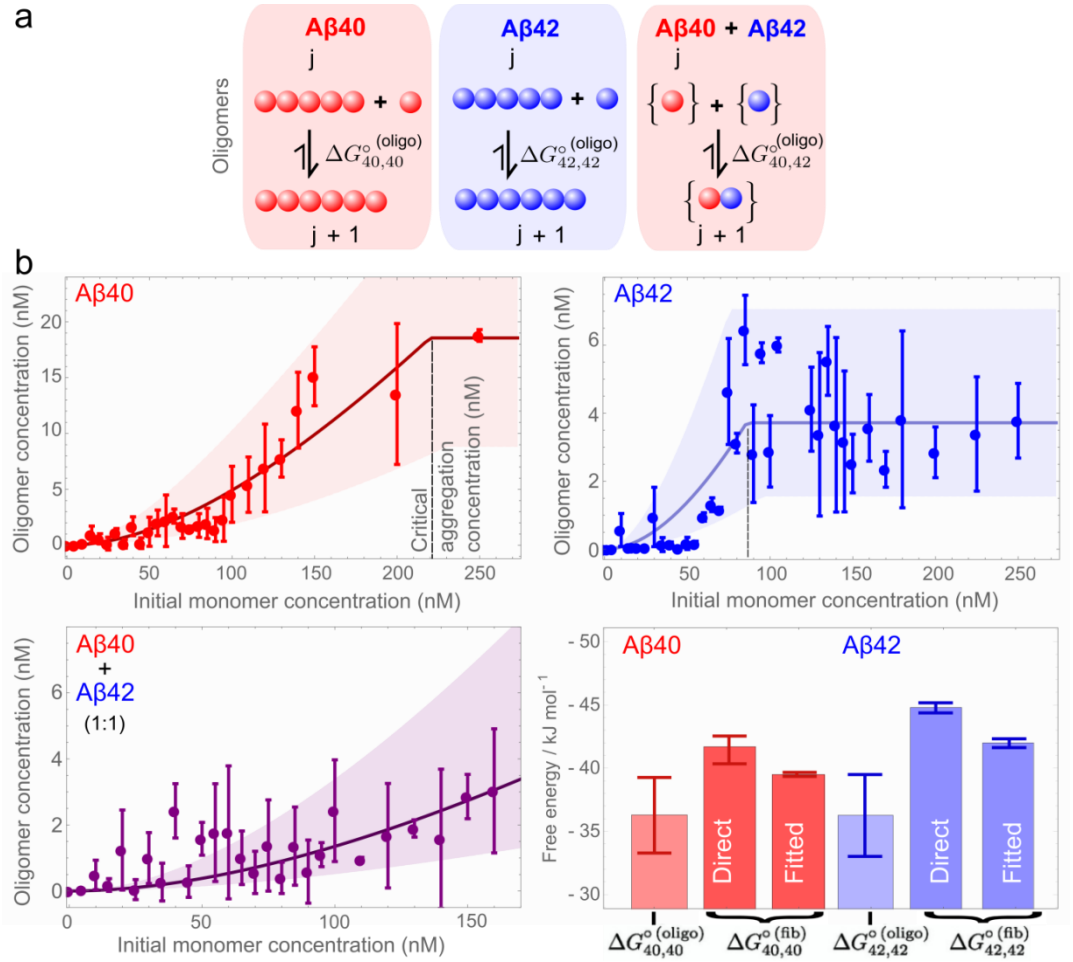

Figure 6.15. a. Schematic of the statistical mechanical model used to estimate Aβ oligomer numbers and relative composition. **b.** Equilibrium oligomer concentrations as a function of the total initial monomer concentration in the aggregation reaction, fitted to the statistical mechanical model in order to extract the free energies of oligomerisation and estimate the CAC for Aβ40 and Aβ42 (fitted curves shown overlaid). The fitted free energies of oligomerisation are also shown in comparison to the free energies of fibril formation obtained by direct measurement of the CAC ("Direct"), and also the free energies of fibril formation obtained from the fitted estimation of the CAC ("Fitted").

6.4 Summary and conclusions

Sensitive TCCD measurements of oligomer and co-oligomer formation at a range of low starting concentrations of Aβ, αS and k18 were carried out. The formation of self-oligomers, as well as the formation of co-oligomers containing monomers of two protein types was observed. The populations of the detected co-oligomers were low, but nevertheless significant as was confirmed in control experiments by analysing non-interacting fluorescent dyes in solution. Additionally, the incubation conditions were varied, and oligomer formation was measured in the presence of unlabelled protein or in the presence of pre-formed fibrils, demonstrating the ease of formation of these species under a range of starting conditions. Furthermore, the critical aggregation concentrations of Aβ isoforms and αS were measured in two independent single-molecule experiments, and sub-micromolar values were obtained. The apparent size distributions of the oligomers were compared, and similar results were obtained from TCCD experiments and TIRFM imaging, showing that the majority of the species were below 5-mers.

Since the formation of both self-oligomers and co-oligomers of the studied proteins was observed for all protein combinations that were analysed in this chapter, and the energetics of co-oligomer formation and self-oligomer formation were found comparable, these co-oligomeric species may be a common type of protein aggregates under the conditions where several types of proteins co-exist.

Even though the described experiments were carried out at the steady-state, it may be very interesting to extend the investigation of co-oligomers in order to determine the role of these aggregates in the kinetics of protein aggregation.

Concluding remarks and future directions

Overall, this dissertation summarises the results of an in-depth investigation of αS aggregation *in vitro* at a broad range of starting conditions. Since this study has been carried out using a powerful set of single-molecule techniques, it reveals unique information on the earliest stages of the aggregation of this protein that cannot be comprehensively characterised using bulk experimental approaches. Specifically, it enables the quantification and characterisation of oligomeric species that are formed prior to the formation of fibrillar aggregates.

In this thesis, the recorded kinetic profiles of oligomer formation and monomer depletion during the aggregation of αS over a 280-fold range of starting αS monomer concentrations enabled a comprehensive quantitative analysis of its aggregation mechanism. The developed explicit kinetic model could fit the experimental results over the entire concentration range, revealing that the aggregation reaction involved two major unimolecular structural conversion steps. The complete set of the rate constants of these key microscopic steps allowed making predictions of the seeding behaviour of αS. The major outcome of this analysis was the identification of high requirements for its templated seeding. It was determined that the number of pre-formed aggregates that would be required to double the aggregation rate of αS in a cell-like volume would be in the order of 10^4, a number that is unlikely to be frequently encountered *in vivo*. Given the well-established proneness of αS to spread in disease, as well as high cytotoxicity of its aggregated forms, particularly oligomers, it was hypothesised that the spreading of this protein was almost likely to be a cell-driven process. Within this picture, the proposed primary role of an aggregate of αS upon entering a cell would be not to template the aggregation of endogenous monomeric protein, as is believed to occur during the spreading of prions, but instead to exert cellular stress. This would result in a change in the local cellular environment and the production of specific aggregation-triggering agents, ultimately leading to the aggregation of monomeric αS as a downstream process. This would be followed by exocytosis of the resulting αS aggregates and their entry into neighbouring cells containing monomeric αS to repeat the process, thus resulting in spreading.

Clearly, even though the primary role of the aggregates of αS as cell stressors has been proposed in this analysis, it remains to be established which stressors might be the best at promoting the subsequent pathogenic aggregation. It may be therefore interesting to further test this, which could be potentially done in a multitude of ways. The first tests could involve straightforward aggregation experiments *in vitro*. Firstly, aggregations using monomeric αS under well-controlled quiescent conditions could be performed. In these experiments, various plausible cell stressors could be added at physiologically-relevant concentrations in order to find out which of them could result in the most

efficient triggering of the aggregation of monomeric αS. Among the potential cell stressors, reactive oxygen species could be investigated, as well as biologically-relevant metal ions, numerous cytokines and stress proteins, as well as their combinations. In the experiments utilising monomeric αS, the screening of additives could help to identify the biologically-relevant components that are most effective at triggering the aggregation reaction. Subsequently, the same could be repeated using a seeded aggregation system that would involve monomeric αS with the concomitant addition of pre-formed αS aggregates and the tested stressors. Since the predictions suggest fibrils as the best seeds, it would be very interesting to carry out aggregation experiments using well-established preparations of pre-formed fibrillar seeds. Indeed, sonicated fibrils may be promising candidates, since well-established reported procedures for their preparation are available. These tests could help to identify the stressors that most effectively promote the seeding. A combination of the stressors that are most effective at both triggering the aggregation reaction and promoting the effect of seeding would be the best candidates for enabling the spreading of αS under cellular environment according to the proposed model, and hence the ones whose concentration should be decreased *in vivo* as a potential therapeutic strategy. This could be subsequently tested by designing experiments aiming to deplete the identified most active stressors *in vivo* in the systems that are expected to exhibit αS aggregation.

Apart from investigating the aggregation mechanism at a range of starting protein concentrations, the effect of two αS-specific Nbs on the aggregation and oligomerisation of αS has been tested. The results were consistent with a selective impact of the Nbs on the conformation conversion between oligomers preceding fibril formation. The investigation indicated that the Nbs effectively inhibited the formation of the most compact high-FRET oligomers. Because high-FRET oligomers have been established to be the most cytotoxic aggregates of αS, this finding may be of potential therapeutic value, provided that further experiments are performed. For example, this result may serve as a basis for experiments examining the effects of Nb-bound oligomers on cells and the effects of Nbs on the aggregation of αS *in vivo*, in order to determine whether the presence of Nbs can lead to a significant and prolonged reduction in cytotoxicity, and whether the concentrations of Nbs needed to observe this effect are within the range of concentrations that could be delivered and maintained under more complex conditions of cellular environment.

In addition, the impact of a biologically-relevant fatty acid ARA on the aggregation of αS has been studied. Interestingly, the oligomers formed upon the action of ARA were found to be distinctly different from the oligomers formed in its absence. To point out, the presented comparative experiments would be very challenging to perform using more conventional experimental approaches. For example, the comparison of such properties as oligomer stability at varying salt concentrations, oligomer disaggregation or the comparison between oligomers formed at varying starting concentrations would be very challenging to perform using more conventional methods. The resulting

strong effect of ARA on the properties of the formed oligomers is an interesting demonstration of the fact that biologically-relevant components can dramatically affect the aggregation of αS as well as the nature of the generated species. It may be interesting to extend this study in order to investigate whether the alpha-helical oligomers of αS can be formed upon the action of other biologically relevant fatty acids or lipids in order to identify the most active inducers of the formation of these types of aggregates. As it has already been mentioned in the corresponding chapter, the role of these multimers both in the mechanism of aggregation and in effecting cells also remains to be investigated further. Because these aggregates so clearly differ from the oligomers formed during the aggregation of αS in aqueous buffer, they may be off-pathway to fibril formation. Thus, it still remains to be established whether their formation can be protective, or equally damaging despite the identified structural differences.

Finally, the co-oligomerisation of αS with other major amyloidogenic proteins, Aβ and tau, has been studied, as well as the oligomerisation of Aβ isoforms. The main conclusion from these experiments was that stable co-oligomers could be formed between the investigated proteins. Their stability was indicated by the ability to detect these species upon their dilutions to very low concentrations used for the single-molecule measurements. Because their formation was observed under a wide range of conditions, either upon combining low concentrations of monomeric proteins in solutions, mixing monomeric proteins with pre-formed fibrils of another protein, or in the presence of excess of unlabelled protein, it can be argued that their formation can generally readily occur under the conditions when multiple proteins are combined. This can suggest that co-oligomers may be as common type of aggregates as the self-oligomers of amyloidogenic proteins. Therefore, their properties and their comparison to the self-oligomers may be further investigated, such as, for example, the comparison of their relative hydrophobicity and toxicity. Furthermore, tests for their formation in cultured cells might be insightful, as well as their identification *in vivo*. It is interesting to note that experiments aiming to identify the presence of co-oligomers in human CSF are currently carried out in this laboratory, with positive results. In addition, the role of these co-oligomers during the aggregation reaction remains to be established. The presumption that they are off-pathway species and act to inhibit the formation of self-fibrils can be unequivocally proven or disproven by performing co-aggregation kinetic experiments. As a promising extension of these potential experiments, it may also be of interest to determine whether these species have any impact on the self- or cross- seeding. Given the permanent co-existence of multiple proteins under more complex cellular environment, the quantitative seeding predictions based on the kinetic datasets for mixed systems containing multiple proteins may be a very interesting as well as highly biologically relevant extension of the seeding predictions derived for αS in this study.

To conclude, the research described in this thesis represents an effort to unravel the molecular mechanism of αS aggregation by *in vitro* experiments carried out using a rare set of tools, and provides unique quantitative information on the processes of αS aggregation, spreading and interactions with other proteins and biologically-relevant components, adding to the knowledge of its aggregation behaviour under a range of presented starting conditions. Furthermore, the described approaches can be applied in order to study various other amyloidogenic proteins and their combinations, to learn about the earliest stages in their aggregation pathways and to predict their aggregation and seeding behaviour, thus providing multiple avenues for future investigations.

Appendix 1

Representative time of flight mass spectra of AF-labelled αS, following the labelling protocol described in section 2.3 (spectra courtesy of Dr. M. Horrocks). In both spectra, the peak at c.a. 14,460 Da, representing unlabelled A90C, is undetectable, and only AF-labelled A90C is present.

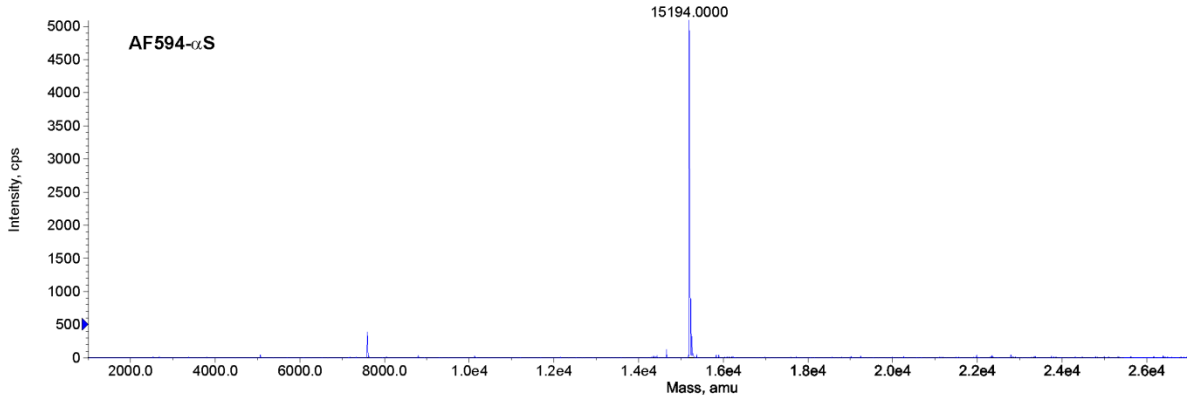

	Mass (avg.)	Mass (mono.)	Apex Mass	Area
1	15381.8341		15381.6914	68340.1740
2	15399.1514		15399.3750	12944.5753
3	15423.9993		15423.8847	7198.0316
4	16208.6809		16207.3319	4233.7586
5	15412.2609		15412.4098	4128.8893

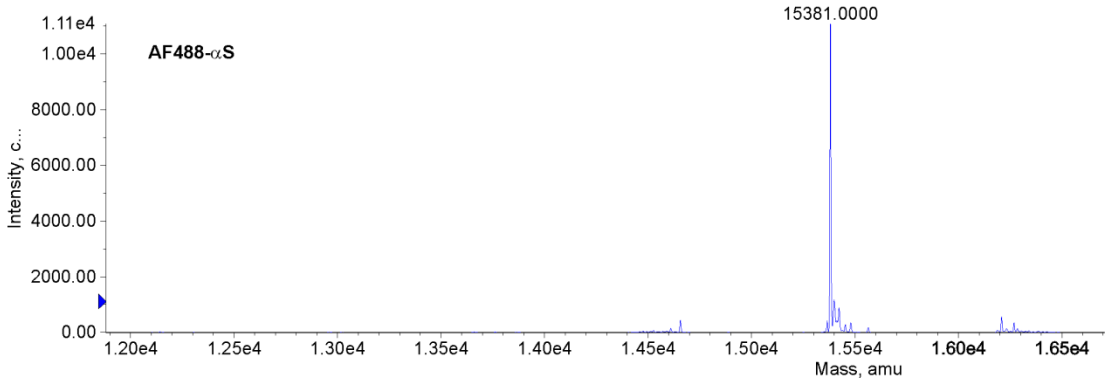

	Mass (avg.)	Mass (mono.)	Apex Mass	Area
1	15381.8341		15381.6914	68340.1740
2	15399.1514		15399.3750	12944.5753
3	15423.9993		15423.8847	7198.0316
4	16208.6809		16207.3319	4233.7586
5	15412.2609		15412.4098	4128.8893

Appendix 2

Derivation of equation 4.1:

$$[aS]_{bound} = \frac{1}{2}\left([aS] + [Nb] + K_d - \sqrt{([aS] + [Nb] + K_d)^2 - 4[aS][Nb]}\right) \quad (4.1)$$

where $[aS]_{bound}$ is the concentration of bound αS, $[aS]$ and $[Nb]$ are the starting concentrations of αS and Nb, 70 μM and 140 μM, respectively, and K_d is the corresponding dissociation constant[172]

Equation 4.1 is a solution of a quadratic equation that results from the definition of the dissociation constant, K_d, based on the law of mass action[175]. The derivation of this equation is included below.

For the reaction

$$[aS]_{free} + [Nb]_{free} \leftrightarrow [complex]$$

According to the law of mass action, the equilibrium dissociation constant is defined as

$$K_d = \frac{[aS]_{free}\ [Nb]_{free}}{[complex]}$$

The concentrations of the unbound components can be expressed simply as the difference between their total starting concentrations and the concentation of the bound complex:

$$[Nb]_{free} = [Nb]_{tot} - [complex]$$

$$[aS]_{free} = [aS]_{tot} - [complex]$$

Can substitute these into the expression for K_d:

$$K_d = \frac{[aS]_{free}\ [Nb]_{free}}{[complex]} = \frac{([aS]_{tot} - [complex]) \times ([Nb]_{tot} - [complex])}{[complex]}$$

By expanding the brackets in the numerator, multiplying both sides by $[complex]$ and re-arranging, obtain

$$[complex]^2 - [complex] \times ([aS]_{tot} + [Nb]_{tot} + K_d) + [aS]_{tot} \times [Nb]_{tot} = 0$$

which is a quadratic equation of the form $ax^2 + bx + c = 0$

where $x = [complex]$; $a = 1$; $b = -([aS]_{tot} + [Nb]_{tot} + K_d)$; and $c = [aS]_{tot} \times [Nb]_{tot}$

Its solution, $x = \frac{-b \pm \sqrt{b^2 - 4as}}{2a}$ results in the equation 4.1, by assuming that $[complex] = [aS]_{bound}$

(owing to the experimentally determined 1:1 binding stoichiometry[172]); and that $[aS]_{bound} \leq [aS]_{total}$.

Appendix 3

Peer-reviewed articles from this work

Iljina, M., Garcia G. A., *et al.* Kinetic model of the aggregation of alpha-synuclein provides insights into prion-like spreading. *Proceedings of the National Academy of Sciences of the United States of America*, vol. 113 no. 9 E1206–E1215 doi:10.1073/pnas.1524128113 (2016).

Iljina M., Garcia G.A., Dear A.J., Flint J., *et. al.* Quantitative analysis of co-oligomer formation by amyloid-beta peptide isoforms. *Scientific Reports*, doi:10.1038/srep28658 (2016).

Iljina M., *et. al.* Arachidonic acid mediates the formation of abundant alpha-helical multimers of alpha-synuclein. Just accepted in *Scientific Reports* (2016).

References

1 George, J. The synucleins. *Genome Biology* **3** (2002).

2 Maroteaux, L., Campanelli, J. & Scheller, R. Synuclein - a neuron-specific protein localized to the nucleus and presynaptic nerve-terminal. *Journal of Neuroscience* **8**, 2804-2815 (1988).

3 Ueda, K. *et al.* Molecular cloning of cDNA - encoding an unrecognized component of amyloid in Alzheimer disease. *Proceedings of the National Academy of Sciences of the United States of America* **90**, 11282-11286, doi:10.1073/pnas.90.23.11282 (1993).

4 Lavedan, C. The synuclein family. *Genome Research* **8**, 871-880 (1998).

5 Deleersnijder, A., Gerard, M., Debyser, Z. & Baekelandt, V. The remarkable conformational plasticity of alpha-synuclein: blessing or curse? *Trends Mol Med*, doi:10.1016/j.molmed.2013.04.002 (2013).

6 Bisaglia, M., Mammi, S. & Bubacco, L. Structural insights on physiological functions and pathological effects of alpha-synuclein. *Faseb Journal* **23**, 329-340, doi:10.1096/fj.08-119784 (2009).

7 Bodner, C., Dobson, C. & Bax, A. Multiple tight phospholipid-binding modes of alpha-synuclein revealed by solution NMR spectroscopy. *Journal of Molecular Biology* **390**, 775-790, doi:10.1016/j.jmb.2009.05.066 (2009).

8 Davidson, W., Jonas, A., Clayton, D. & George, J. Stabilization of alpha-synuclein secondary structure upon binding to synthetic membranes. *Journal of Biological Chemistry* **273**, 9443-9449, doi:10.1074/jbc.273.16.9443 (1998).

9 Segrest, J. *et al.* The amphipathic helix in the exchangeable apolipoproteins - a review of secondary structure and function. *Journal of Lipid Research* **33**, 141-166 (1992).

10 Eliezer, D., Kutluay, E., Bussell, R. & Browne, G. Conformational properties of alpha-synuclein in its free and lipid-associated states. *Journal of Molecular Biology* **307**, 1061-1073, doi:10.1006/jmbi.2001.4538 (2001).

11 Necula, M., Chirita, C. & Kuret, J. Rapid anionic micelle-mediated alpha-synuclein fibrillization in vitro. *Journal of Biological Chemistry* **278**, 46674-46680, doi:10.1074/jbc.M308231200 (2003).

12 Westphal, C. & Chandra, S. Monomeric synucleins generate membrane curvature. *Journal of Biological Chemistry* **288**, 1829-1840, doi:10.1074/jbc.M112.418871 (2013).

13 Varkey, J. *et al.* Membrane curvature induction and tubulation are common features of synucleins and apolipoproteins. *Journal of Biological Chemistry* **285**, 32486-32493, doi:10.1074/jbc.M110.139576 (2010).

14 Middleton, E. & Rhoades, E. Effects of curvature and composition on alpha-synuclein binding to lipid vesicles. *Biophysical Journal* **99**, 2279-2288, doi:10.1016/j.bpj.2010.07.056 (2010).

15 Beyer, K. Mechanistic aspects of Parkinson's disease: alpha-synuclein and the biomembrane. *Cell Biochemistry and Biophysics* **47**, 285-299, doi:10.1007/s12013-007-0014-9 (2007).

16 Venda, L., Cragg, S., Buchman, V. & Wade-Martins, R. Alpha-synuclein and dopamine at the crossroads of Parkinson's disease. *Trends in Neurosciences* **33**, 559-568, doi:10.1016/j.tins.2010.09.004 (2010).

17 Appel-Cresswell, S. *et al.* Alpha-synuclein PH50Q, a novel pathogenic mutation for Parkinson's disease. *Mov Disord*, doi:10.1002/mds.25421 (2013).

18 Kiely, A. *et al.* Synucleinopathy with a G51D a-synuclein mutation: a neuropathological and genetic study. *Neuropathology and Applied Neurobiology* **39**, 39-40 (2013).

19 Kessler, J., Rochet, J. & Lansbury, P. The N-terminal repeat domain of alpha-synuclein inhibits beta-sheet and amyloid fibril formation. *Biochemistry* **42**, 672-678, doi:10.1021/bi020429y (2003).

20 Koo, H., Lee, H. & Im, H. Sequence determinants regulating fibrillation of human alpha-synuclein. *Biochemical and Biophysical Research Communications* **368**, 772-778, doi:10.1016/j.bbrc.2008.01.140 (2008).

21 El-Agnaf, O. & Irvine, G. Aggregation and neurotoxicity of alpha-synuclein and related peptides. *Biochemical Society Transactions* **30**, 559-565 (2002).
22 Serpell, L., Berriman, J., Jakes, R., Goedert, M. & Crowther, R. Fiber diffraction of synthetic alpha-synuclein filaments shows amyloid-like cross-beta conformation. *Proceedings of the National Academy of Sciences of the United States of America* **97**, 4897-4902, doi:10.1073/pnas.97.9.4897 (2000).
23 Miake, H., Mizusawa, H., Iwatsubo, T. & Hasegawa, M. Biochemical characterization of the core structure of alpha-synuclein filaments. *Journal of Biological Chemistry* **277**, 19213-19219, doi:10.1074/jbc.M110551200 (2002).
24 Der-Sarkissian, A., Jao, C., Chen, J. & Langen, R. Structural organization of alpha-synuclein fibrils studied by site-directed spin labeling. *Journal of Biological Chemistry* **278**, 37530-37535, doi:10.1074/jbc.M305266200 (2003).
25 Del Mar, C., Greenbaum, E., Mayne, L., Englander, S. & Woods, V. Structure and properties of alpha-synuclein and other amyloids determined at the amino acid level. *Proceedings of the National Academy of Sciences of the United States of America* **102**, 15477-15482, doi:10.1073/pnas.0507405102 (2005).
26 Heise, H. *et al.* Molecular-level secondary structure, polymorphism, and dynamics of full-length alpha-synuclein fibrils studied by solid-state NMR. *Proceedings of the National Academy of Sciences of the United States of America* **102**, 15871-15876, doi:10.1073/pnas.0506109102 (2005).
27 Giasson, B., Murray, I., Trojanowski, J. & Lee, V. A hydrophobic stretch of 12 amino acid residues in the middle of alpha-synuclein is essential for filament assembly. *Journal of Biological Chemistry* **276**, 2380-2386, doi:10.1074/jbc.M008919200 (2001).
28 Du, H. *et al.* A peptide motif consisting of glycine, alanine, and valine is required for the fibrillization and cytotoxicity of human alpha-synuclein. *Biochemistry* **42**, 8870-8878, doi:10.1021/bi034028+ (2003).
29 Koo, H., Choi, M. & Im, H. Aggregation-defective alpha-synuclein mutants inhibit the fibrillation of Parkinson's disease-linked alpha-synuclein variants. *Biochemical and Biophysical Research Communications* **386**, 165-169, doi:10.1016/j.bbrc.2009.06.002 (2009).
30 Park, S. *et al.* Stress-induced aggregation profiles of GST-alpha-synuclein fusion proteins: role of the C-terminal acidic tail of alpha-synuclein in protein thermosolubility and stability. *Biochemistry* **41**, 4137-4146, doi:10.1021/bi015961k (2002).
31 Hong, D., Xiong, W., Chang, J. & Jiang, C. The role of the C-terminus of human alpha-synuclein: Intra-disulfide bonds between the C-terminus and other regions stabilize non-fibrillar monomeric isomers. *Febs Letters* **585**, 561-566, doi:10.1016/j.febslet.2011.01.009 (2011).
32 Qin, Z., Hu, D., Han, S., Hong, D. & Fink, A. Role of different regions of alpha-synuclein in the assembly of fibrils. *Biochemistry* **46**, 13322-13330, doi:10.1021/bi7014053 (2007).
33 Meuvis, J., Gerard, M., Desender, L., Baekelandt, V. & Engelborghs, Y. The conformation and the aggregation kinetics of alpha-synuclein depend on the proline residues in its C-terminal region. *Biochemistry* **49**, 9345-9352, doi:10.1021/bi1010927 (2010).
34 Hoyer, W., Cherny, D., Subramaniam, V. & Jovin, T. Impact of the acidic C-terminal region comprising amino acids 109-140 on alpha-synuclein aggregation in vitro. *Biochemistry* **43**, 16233-16242, doi:10.1021/bi048453u (2004).
35 Uversky, V. Intrinsically disordered proteins from A to Z. *International Journal of Biochemistry & Cell Biology* **43**, 1090-1103, doi:10.1016/j.biocel.2011.04.001 (2011).
36 Weinreb, P., Zhen, W., Poon, A., Conway, K. & Lansbury, P. NACP, a protein implicated in Alzheimer's disease and learning, is natively unfolded. *Biochemistry* **35**, 13709-13715, doi:10.1021/bi961799n (1996).
37 Wright, P. & Dyson, H. Intrinsically unstructured proteins: re-assessing the protein structure-function paradigm. *Journal of Molecular Biology* **293**, 321-331, doi:10.1006/jmbi.1999.3110 (1999).

38 Uversky, V., Gillespie, J. & Fink, A. Why are "natively unfolded" proteins unstructured under physiologic conditions? *Proteins-Structure Function and Genetics* **41**, 415-427, doi:10.1002/1097-0134(20001115)41:3<415:AID-PROT130>3.0.CO;2-7 (2000).
39 Bonini, N. M. & Giasson, B. I. Snaring the function of alpha-synuclein. *Cell* **123**, 359-361, doi:10.1016/j.cell.2005.10.017 (2005).
40 Irizarry, M. *et al.* Characterization of the precursor protein of the non-a-beta component of senile plaques (NACP) in the human central nervous system. *Journal of Neuropathology and Experimental Neurology* **55**, 889-895 (1996).
41 Liu, G. *et al.* Alpha-synuclein is differentially expressed in mitochondria from different rat brain regions and dose-dependently down-regulates complex I activity. *Neurosci Lett* **454**, 187-192, doi:10.1016/j.neulet.2009.02.056 (2009).
42 Iwai, A. *et al.* The precursor protein of non-abeta component of Alzheimers disease amyloid is a presynaptic protein of the central nervous system. *Neuron* **14**, 467-475, doi:10.1016/0896-6273(95)90302-X (1995).
43 Shibayama-Imazu, T. *et al.* Cell and tissue distribution and developmental change of neuron specific 14 kDa protein (phosphoneuroprotein 14). *Brain Res* **622**, 17-25 (1993).
44 Jakes, R., Spillantini, M. G. & Goedert, M. Identification of two distinct synucleins from human brain. *FEBS Lett* **345**, 27-32 (1994).
45 Bartels, T., Choi, J. G. & Selkoe, D. J. Alpha-synuclein occurs physiologically as a helically folded tetramer that resists aggregation. *Nature* **477**, 107-110, doi:10.1038/nature10324 (2011).
46 Clayton, D. & George, J. Synucleins in synaptic plasticity and neurodegenerative disorders. *Journal of Neuroscience Research* **58**, 120-129, doi:10.1002/(SICI)1097-4547(19991001)58:1, (1999).
47 Bellani, S. *et al.* The regulation of synaptic function by alpha-synuclein. *Commun Integr Biol* **3**, 106-109 (2010).
48 Perlmutter, J., Braun, A. & Sachs, J. Curvature dynamics of alpha-synuclein familial Parkinson disease mutants. Molecular simulations of the micelle- and bilayer-bound forms. *Journal of Biological Chemistry* **284**, 7177-7189, doi:10.1074/jbc.M808895200 (2009).
49 Davies, P., Moualla, D. & Brown, D. Alpha-synuclein is a cellular ferrireductase. *Plos One* **6**, doi:10.1371/journal.pone.0015814 (2011).
50 Quilty, M. *et al.* Alpha-synuclein is upregulated in neurones in response to chronic oxidative stress and is associated with neuroprotection. *Experimental Neurology* **199**, 249-256, doi:10.1016/j.expneurol.2005.10.018 (2006).
51 Breydo, L., Wu, J. W. & Uversky, V. N. Alpha-synuclein misfolding and Parkinson's disease. *Biochim Biophys Acta* **1822**, 261-285, doi:10.1016/j.bbadis.2011.10.002 (2012).
52 Abeliovich, A. *et al.* Mice lacking alpha-synuclein display functional deficits in the nigrostriatal dopamine system. *Neuron* **25**, 239-252 (2000).
53 Chandra, S. *et al.* Double-knockout mice for alpha- and beta-synucleins: effect on synaptic functions. *Proceedings of the National Academy of Sciences of the United States of America* **101**, 14966-14971, doi:10.1073/pnas.0406283101 (2004).
54 Burre, J. *et al.* Alpha-synuclein promotes SNARE-complex assembly in vivo and in vitro. *Science* **329**, 1663-1667, doi:10.1126/science.1195227 (2010).
55 Olanow, C. & Brundin, P. Parkinson's disease and alpha synuclein: is Parkinson's disease a prion-like disorder? *Movement Disorders* **28**, 31-40, doi:10.1002/mds.25373 (2013).
56 Lees, A. Unresolved issues relating to the shaking palsy on the celebration of James Parkinson's 250th birthday. *Movement Disorders* **22**, S327-S334, doi:10.1002/mds.21684 (2007).
57 de Lau, L. M. & Breteler, M. M. Epidemiology of Parkinson's disease. *Lancet Neurol* **5**, 525-535, doi:10.1016/S1474-4422(06)70471-9 (2006).
58 Samii, A., Nutt, J. G. & Ransom, B. R. Parkinson's disease. *Lancet* **363**, 1783-1793, doi:10.1016/S0140-6736(04)16305-8 (2004).
59 Hoehn, M. & Yahr, M. Parkinsonism: onset, progression, and mortality (reprinted from Neurology, vol 17, pg 427-442, 1967). *Neurology* **50**, B1-B16 (1998).

60 Jankovic, J. Parkinson's disease: clinical features and diagnosis. *Journal of Neurology Neurosurgery and Psychiatry* **79**, 368-376, doi:10.1136/jnnp.2007.131045 (2008).
61 Forno, L. Neuropathology of Parkinson's disease. *Journal of Neuropathology and Experimental Neurology* **55**, 259-272, doi:10.1097/00005072-199603000-00001 (1996).
62 Schulz-Schaeffer, W. The synaptic pathology of alpha-synuclein aggregation in dementia with Lewy bodies, Parkinson's disease and Parkinson's disease dementia. *Acta Neuropathologica* **120**, 131-143, doi:10.1007/s00401-010-0711-0 (2010).
63 FH, L. in *ed. Handbuch de Neurologie* (ed Lewandowsky M):920–933. (Springer, Berlin, 1912).
64 Spillantini, M. G. *et al.* Alpha-synuclein in Lewy bodies. *Nature* **388**, 839-840, doi:10.1038/42166 (1997).
65 Uryu, K. *et al.* Convergence of heat shock protein 90 with ubiquitin in filamentous alpha-synuclein inclusions of alpha-synucleinopathies. *Am J Pathol* **168**, 947-961 (2006).
66 Halliday, G. M., Del Tredici, K. & Braak, H. Critical appraisal of brain pathology staging related to presymptomatic and symptomatic cases of sporadic Parkinson's disease. *J Neural Transm Suppl*, 99-103 (2006).
67 Fujiwara, H. *et al.* Alpha-synuclein is phosphorylated in synucleinopathy lesions. *Nat Cell Biol* **4**, 160-164, doi:10.1038/ncb748 (2002).
68 Uversky, V. N. Neuropathology, biochemistry, and biophysics of alpha-synuclein aggregation. *J Neurochem* **103**, 17-37, doi:10.1111/j.1471-4159.2007.04764.x (2007).
69 Lee, V. & Trojanowski, J. Mechanisms of Parkinson's disease linked to pathological alpha-synuclein: new targets for drug discovery. *Neuron* **52**, 33-38, doi:10.1016/j.neuron.2006.09.026 (2006).
70 Masliah, E. *et al.* Dopaminergic loss and inclusion body formation in alpha-synuclein mice: implications for neurodegenerative disorders. *Science* **287**, 1265-1269, doi:10.1126/science.287.5456.1265 (2000).
71 Feany, M. & Bender, W. A Drosophila model of Parkinson's disease. *Nature* **404**, 394-398, doi:10.1038/35006074 (2000).
72 Kirik, D. *et al.* Nigrostriatal alpha-synucleinopathy induced by viral vector-mediated overexpression of human alpha-synuclein: a new primate model of Parkinson's disease. *Proceedings of the National Academy of Sciences of the United States of America* **100**, 2884-2889, doi:10.1073/pnas.0536383100|10.1073/pnas.053683100 (2003).
73 Greffard, S. *et al.* A stable proportion of Lewy body bearing neurons in the substantia nigra suggests a model in which the Lewy body causes neuronal death. *Neurobiology of Aging* **31**, 99-103, doi:10.1016/j.neurobiolaging.2008.03.015 (2010).
74 Markopoulou, K. *et al.* Genetic Evidence for a Dual and Opposing Effect of alpha-Synuclein Expression in Preclinical Versus Clinical Parkinson's Disease (IN2-1.003) (New Insights into Molecular Mechanisms in Parkinson's Disease Posters, 2013).
75 Chiti, F. & Dobson, C. M. Protein misfolding, functional amyloid, and human disease. *Annu Rev Biochem* **75**, 333-366, doi:10.1146/annurev.biochem.75.101304.123901 (2006).
76 Conway, K. *et al.* Acceleration of oligomerization, not fibrillization, is a shared property of both alpha-synuclein mutations linked to early-onset Parkinson's disease: implications for pathogenesis and therapy. *Proceedings of the National Academy of Sciences of the United States of America* **97**, 571-576, doi:10.1073/pnas.97.2.571 (2000).
77 Kalia, L. V., Kalia, S. K., McLean, P. J., Lozano, A. M. & Lang, A. E. Alpha-synuclein oligomers and clinical implications for Parkinson disease. *Ann Neurol* **73**, 155-169, doi:10.1002/ana.23746 (2013).
78 Volles, M. J. *et al.* Vesicle permeabilization by protofibrillar alpha-synuclein: implications for the pathogenesis and treatment of Parkinson's disease. *Biochemistry* **40**, 7812-7819 (2001).
79 Cremades, N. *et al.* Direct observation of the interconversion of normal and toxic forms of alpha-synuclein. *Cell* **149**, 1048-1059, doi:10.1016/j.cell.2012.03.037 (2012).
80 Conway, K. A., Rochet, J. C., Bieganski, R. M. & Lansbury, P. T. Kinetic stabilization of the alpha-synuclein protofibril by a dopamine-alpha-synuclein adduct. *Science* **294**, 1346-1349, doi:10.1126/science.1063522 (2001).

81 Winner, B. *et al.* In vivo demonstration that alpha-synuclein oligomers are toxic. *Proceedings of the National Academy of Sciences of the United States of America* **108**, 4194-4199, doi:10.1073/pnas.1100976108 (2011).
82 Roberts, R. F., Wade-Martins, R. & Alegre-Abarrategui, J. Direct visualization of alpha-synuclein oligomers reveals previously undetected pathology in Parkinson's disease brain. *Brain* **138**, 1642-1657, doi:10.1093/brain/awv040 (2015).
83 Iljina, M. *et al.* Kinetic model of the aggregation of alpha-synuclein provides insights into prion-like spreading. *Proceedings of the National Academy of Sciences of the United States of America*, doi:10.1073/pnas.1524128113 (2016).
84 Chen, S. W. *et al.* Structural characterization of toxic oligomers that are kinetically trapped during alpha-synuclein fibril formation. *Proceedings of the National Academy of Sciences of the United States of America, U S A* **112**, E1994-2003, doi:10.1073/pnas.1421204112 (2015).
85 Kim, H. Y. *et al.* Structural properties of pore-forming oligomers of alpha-synuclein. *J Am Chem Soc* **131**, 17482-17489, doi:10.1021/ja9077599 (2009).
86 Pieri, L., Madiona, K. & Melki, R. Structural and functional properties of prefibrillar alpha-synuclein oligomers. *Sci Rep* **6**, 24526, doi:10.1038/srep24526 (2016).
87 Conway, K. A., Harper, J. D. & Lansbury, P. T. Fibrils formed in vitro from alpha-synuclein and two mutant forms linked to Parkinson's disease are typical amyloid. *Biochemistry* **39**, 2552-2563 (2000).
88 Lashuel, H. A. *et al.* Alpha-synuclein, especially the Parkinson's disease-associated mutants, forms pore-like annular and tubular protofibrils. *J Mol Biol* **322**, 1089-1102 (2002).
89 Lorenzen, N. *et al.* The role of stable alpha-synuclein oligomers in the molecular events underlying amyloid formation. *J Am Chem Soc* **136**, 3859-3868, doi:10.1021/ja411577t (2014).
90 Paslawski, W. *et al.* High stability and cooperative unfolding of alpha-synuclein oligomers. *Biochemistry* **53**, 6252-6263, doi:10.1021/bi5007833 (2014).
91 Andreasen, M., Lorenzen, N. & Otzen, D. Interactions between misfolded protein oligomers and membranes: a central topic in neurodegenerative diseases? *Biochim Biophys Acta* **1848**, 1897-1907, doi:10.1016/j.bbamem.2015.01.018 (2015).
92 Bolognesi, B. *et al.* ANS binding reveals common features of cytotoxic amyloid species. *ACS Chem Biol* **5**, 735-740, doi:10.1021/cb1001203 (2010).
93 Bongiovanni, M. N. *et al.* Multi-dimensional super-resolution imaging enables surface hydrophobicity mapping. *Nat Commun* **7**, 13544, doi:10.1038/ncomms13544 (2016).
94 Zijlstra, N., Blum, C., Segers-Nolten, I. M., Claessens, M. M. & Subramaniam, V. Molecular composition of sub-stoichiometrically labeled alpha-synuclein oligomers determined by single-molecule photobleaching. *Angew Chem Int Ed Engl* **51**, 8821-8824, doi:10.1002/anie.201200813 (2012).
95 Lippa, C. F., Schmidt, M. L., Lee, V. M. & Trojanowski, J. Q. Antibodies to alpha-synuclein detect Lewy bodies in many Down's syndrome brains with Alzheimer's disease. *Ann Neurol* **45**, 353-357 (1999).
96 Arawaka, S., Saito, Y., Murayama, S. & Mori, H. Lewy body in neurodegeneration with brain iron accumulation type 1 is immunoreactive for alpha-synuclein. *Neurology* **51**, 887-889 (1998).
97 Newell, K. L. *et al.* Alpha-synuclein immunoreactivity is present in axonal swellings in neuroaxonal dystrophy and acute traumatic brain injury. *J Neuropathol Exp Neurol* **58**, 1263-1268 (1999).
98 Serpell, L. C., Berriman, J., Jakes, R., Goedert, M. & Crowther, R. A. Fiber diffraction of synthetic alpha-synuclein filaments shows amyloid-like cross-beta conformation. *Proceedings of the National Academy of Sciences of the United States of America* **97**, 4897-4902 (2000).
99 Paik, S., Shin, H., Lee, J., Chang, C. & Kim, J. Copper(II)-induced self-oligomerization of alpha-synuclein. *Biochemical Journal* **340**, 821-828, doi:10.1042/0264-6021:3400821 (1999).
100 Nielsen, M., Vorum, H., Lindersson, E. & Jensen, P. Ca2+ binding to alpha-synuclein regulates ligand binding and oligomerization. *Journal of Biological Chemistry* **276**, 22680-22684, doi:10.1074/jbc.M101181200 (2001).

101 Giasson, B. I., Uryu, K., Trojanowski, J. Q. & Lee, V. M. Mutant and wild type human alpha-synucleins assemble into elongated filaments with distinct morphologies in vitro. *J Biol Chem* **274**, 7619-7622 (1999).
102 Uversky, V. N., Li, J. & Fink, A. L. Evidence for a partially folded intermediate in alpha-synuclein fibril formation. *J Biol Chem* **276**, 10737-10744, doi:10.1074/jbc.M010907200 (2001).
103 Jarrett, J. T. & Lansbury, P. T. Amyloid fibril formation requires a chemically discriminating nucleation event: studies of an amyloidogenic sequence from the bacterial protein OsmB. *Biochemistry* **31**, 12345-12352 (1992).
104 Wood, S. J. *et al.* Alpha-synuclein fibrillogenesis is nucleation-dependent. Implications for the pathogenesis of Parkinson's disease. *J Biol Chem* **274**, 19509-19512 (1999).
105 Baldwin, A. J. *et al.* Metastability of native proteins and the phenomenon of amyloid formation. *J Am Chem Soc* **133**, 14160-14163, doi:10.1021/ja2017703 (2011).
106 Knowles, T. *et al.* An analytical solution to the kinetics of breakable filament assembly. *Science* **326**, 1533-1537, doi:10.1126/science.1178250 (2009).
107 Cohen, S. I., Vendruscolo, M., Dobson, C. M. & Knowles, T. P. From macroscopic measurements to microscopic mechanisms of protein aggregation. *J Mol Biol* **421**, 160-171, doi:10.1016/j.jmb.2012.02.031 (2012).
108 Walter, N. G., Huang, C. Y., Manzo, A. J. & Sobhy, M. A. Do-it-yourself guide: how to use the modern single-molecule toolkit. *Nat Methods* **5**, 475-489, doi:10.1038/nmeth.1215 (2008).
109 Orte, A. *et al.* Direct characterization of amyloidogenic oligomers by single-molecule fluorescence. *Proceedings of the National Academy of Sciences of the United States of America* **105**, 14424-14429, doi:10.1073/pnas.0803086105 (2008).
110 Narayan, P. *et al.* The extracellular chaperone clusterin sequesters oligomeric forms of the amyloid-β(1-40) peptide. *Nat Struct Mol Biol* **19**, 79-83, doi:10.1038/nsmb.2191 (2012).
111 Narayan, P. *et al.* Single molecule characterization of the interactions between amyloid-β peptides and the membranes of hippocampal cells. *J Am Chem Soc* **135**, 1491-1498, doi:10.1021/ja3103567 (2013).
112 Orte, A., Clarke, R. W. & Klenerman, D. Single-molecule fluorescence coincidence spectroscopy and its application to resonance energy transfer. *Chemphyschem* **12**, 491-499, doi:10.1002/cphc.201000636 (2011).
113 Deniz, A. A. *et al.* Single-pair fluorescence resonance energy transfer on freely diffusing molecules: observation of Förster distance dependence and subpopulations. *Proceedings of the National Academy of Sciences of the United States of America* **96**, 3670-3675 (1999).
114 Horrocks, M. H. *et al.* Single molecule fluorescence under conditions of fast flow. *Anal Chem* **84**, 179-185, doi:10.1021/ac202313d (2012).
115 Horrocks, M. H. *et al.* Fast flow microfluidics and single-molecule fluorescence for the rapid characterization of alpha-synuclein oligomers. *Anal Chem* **87**, 8818-8826, doi:10.1021/acs.analchem.5b01811 (2015).
116 Hoyer, W. *et al.* Dependence of alpha-synuclein aggregate morphology on solution conditions. *Journal of Molecular Biology* **322**, 383-393, doi:10.1016/S0022-2836(02)00775-1 (2002).
117 Clarke, R., Orte, A. & Klenerman, D. Optimized threshold selection for single-molecule two-color fluorescence coincidence spectroscopy. *Analytical Chemistry* **79**, 2771-2777, doi:10.1021/ac062188w (2007).
118 Ying, L., Wallace, M., Balasubramanian, S. & Klenerman, D. Ratiometric analysis of single-molecule fluorescence resonance energy transfer using logical combinations of threshold criteria: a study of 12-mer DNA. *Journal of Physical Chemistry B* **104**, 5171-5178, doi:10.1021/jp993914k (2000).
119 McKeith, I. G. *et al.* Consensus guidelines for the clinical and pathologic diagnosis of dementia with Lewy bodies (DLB): report of the consortium on DLB international workshop. *Neurology* **47**, 1113-1124 (1996).
120 Braak, H. *et al.* Staging of brain pathology related to sporadic Parkinson's disease. *Neurobiology of Aging* **24**, 197-211, doi:10.1016/S0197-4580(02)00065-9.

121 Bloch, A., Probst, A., Bissig, H., Adams, H. & Tolnay, M. Alpha-synuclein pathology of the spinal and peripheral autonomic nervous system in neurologically unimpaired elderly subjects. *Neuropathol Appl Neurobiol* **32**, 284-295, doi:10.1111/j.1365-2990.2006.00727.x (2006).
122 Kalaitzakis, M. E., Graeber, M. B., Gentleman, S. M. & Pearce, R. K. Controversies over the staging of alpha-synuclein pathology in Parkinson's disease. *Acta Neuropathol* **116**, 125-128; author reply 129-131, doi:10.1007/s00401-008-0381-3 (2008).
123 Doty, R. L., Deems, D. A., Frye, R. E., Pelberg, R. & Shapiro, A. Olfactory sensitivity, nasal resistance, and autonomic function in patients with multiple chemical sensitivities. *Arch Otolaryngol Head Neck Surg* **114**, 1422-1427 (1988).
124 Dickson, D. W. *et al.* Evidence that incidental Lewy body disease is pre-symptomatic Parkinson's disease. *Acta Neuropathol* **115**, 437-444, doi:10.1007/s00401-008-0345-7 (2008).
125 Mamais, A. *et al.* Divergent alpha-synuclein solubility and aggregation properties in G2019S LRRK2 Parkinson's disease brains with Lewy Body pathology compared to idiopathic cases. *Neurobiol Dis* **58**, 183-190, doi:10.1016/j.nbd.2013.05.017 (2013).
126 Li, J. Y. *et al.* Lewy bodies in grafted neurons in subjects with Parkinson's disease suggest host-to-graft disease propagation. *Nat Med* **14**, 501-503, doi:10.1038/nm1746 (2008).
127 Brundin, P., Li, J. Y., Holton, J. L., Lindvall, O. & Revesz, T. Research in motion: the enigma of Parkinson's disease pathology spread. *Nat Rev Neurosci* **9**, 741-745, doi:10.1038/nrn2477 (2008).
128 Prusiner, S. B. Novel proteinaceous infectious particles cause scrapie. *Science* **216**, 136-144 (1982).
129 Prusiner, S. B. Cell biology. A unifying role for prions in neurodegenerative diseases. *Science* **336**, 1511-1513, doi:10.1126/science.1222951 (2012).
130 Hardy, J. Expression of normal sequence pathogenic proteins for neurodegenerative disease contributes to disease risk: 'permissive templating' as a general mechanism underlying neurodegeneration. *Biochem Soc Trans* **33**, 578-581, doi:10.1042/BST0330578 (2005).
131 Golde, T. E., Borchelt, D. R., Giasson, B. I. & Lewis, J. Thinking laterally about neurodegenerative proteinopathies. *J Clin Invest* **123**, 1847-1855, doi:10.1172/JCI66029 (2013).
132 Chu, Y. & Kordower, J. H. The prion hypothesis of Parkinson's disease. *Curr Neurol Neurosci Rep* **15**, 28, doi:10.1007/s11910-015-0549-x (2015).
133 Chauhan, A. & Jeans, A. F. Is Parkinson's disease truly a prion-like disorder? An appraisal of current evidence. *Neurol Res Int* **2015**, 345285, doi:10.1155/2015/345285 (2015).
134 Rey, N. L., Petit, G. H., Bousset, L., Melki, R. & Brundin, P. Transfer of human alpha-synuclein from the olfactory bulb to interconnected brain regions in mice. *Acta Neuropathol* **126**, 555-573, doi:10.1007/s00401-013-1160-3 (2013).
135 Desplats, P. *et al.* Inclusion formation and neuronal cell death through neuron-to-neuron transmission of alpha-synuclein. *Proceedings of the National Academy of Sciences of the United States of America* **106**, 13010-13015, doi:10.1073/pnas.0903691106 (2009).
136 Danzer, K. M., Krebs, S. K., Wolff, M., Birk, G. & Hengerer, B. Seeding induced by alpha-synuclein oligomers provides evidence for spreading of alpha-synuclein pathology. *J Neurochem* **111**, 192-203, doi:10.1111/j.1471-4159.2009.06324.x (2009).
137 Hansen, C. *et al.* Alpha-synuclein propagates from mouse brain to grafted dopaminergic neurons and seeds aggregation in cultured human cells. *J Clin Invest* **121**, 715-725, doi:10.1172/JCI43366 (2011).
138 Luk, K. C. *et al.* Intracerebral inoculation of pathological alpha-synuclein initiates a rapidly progressive neurodegenerative alpha-synucleinopathy in mice. *J Exp Med* **209**, 975-986, doi:10.1084/jem.20112457 (2012).
139 Luk, K. C. *et al.* Pathological alpha-synuclein transmission initiates Parkinson-like neurodegeneration in nontransgenic mice. *Science* **338**, 949-953, doi:10.1126/science.1227157 (2012).
140 Masuda-Suzukake, M. *et al.* Prion-like spreading of pathological alpha-synuclein in brain. *Brain* **136**, 1128-1138, doi:10.1093/brain/awt037 (2013).

141 Recasens, A. *et al.* Lewy body extracts from Parkinson disease brains trigger alpha-synuclein pathology and neurodegeneration in mice and monkeys. *Ann Neurol* **75**, 351-362, doi:10.1002/ana.24066 (2014).
142 Reyes, J. F. *et al.* Alpha-synuclein transfers from neurons to oligodendrocytes. *Glia* **62**, 387-398, doi:10.1002/glia.22611 (2014).
143 Solano, S. M., Miller, D. W., Augood, S. J., Young, A. B. & Penney, J. B. Expression of alpha-synuclein, parkin, and ubiquitin carboxy-terminal hydrolase L1 mRNA in human brain: genes associated with familial Parkinson's disease. *Ann Neurol* **47**, 201-210 (2000).
144 Tu, P. H. *et al.* Glial cytoplasmic inclusions in white matter oligodendrocytes of multiple system atrophy brains contain insoluble alpha-synuclein. *Ann Neurol* **44**, 415-422, doi:10.1002/ana.410440324 (1998).
145 Arai, T. *et al.* Argyrophilic glial inclusions in the midbrain of patients with Parkinson's disease and diffuse Lewy body disease are immunopositive for NACP/alpha-synuclein. *Neurosci Lett* **259**, 83-86 (1999).
146 Miller, D. W. *et al.* Absence of alpha-synuclein mRNA expression in normal and multiple system atrophy oligodendroglia. *J Neural Transm* **112**, 1613-1624, doi:10.1007/s00702-005-0378-1 (2005).
147 Sacino, A. N. *et al.* Intramuscular injection of alpha-synuclein induces CNS alpha-synuclein pathology and a rapid-onset motor phenotype in transgenic mice. *Proceedings of the National Academy of Sciences of the United States of America* **111**, 10732-10737, doi:10.1073/pnas.1321785111 (2014).
148 Osterberg, V. R. *et al.* Progressive aggregation of alpha-synuclein and selective degeneration of Lewy inclusion-bearing neurons in a mouse model of parkinsonism. *Cell Rep* **10**, 1252-1260, doi:10.1016/j.celrep.2015.01.060 (2015).
149 Wu, K. P., Weinstock, D. S., Narayanan, C., Levy, R. M. & Baum, J. Structural reorganization of alpha-synuclein at low pH observed by NMR and REMD simulations. *J Mol Biol* **391**, 784-796, doi:10.1016/j.jmb.2009.06.063 (2009).
150 Crowther, R. A., Daniel, S. E. & Goedert, M. Characterisation of isolated alpha-synuclein filaments from substantia nigra of Parkinson's disease brain. *Neurosci Lett* **292**, 128-130 (2000).
151 Yonetani, M. *et al.* Conversion of wild-type alpha-synuclein into mutant-type fibrils and its propagation in the presence of A30P mutant. *J Biol Chem* **284**, 7940-7950, doi:10.1074/jbc.M807482200 (2009).
152 Buell, A. K. *et al.* Solution conditions determine the relative importance of nucleation and growth processes in alpha-synuclein aggregation. *Proceedings of the National Academy of Sciences of the United States of America* **111**, 7671-7676, doi:10.1073/pnas.1315346111 (2014).
153 Jönsson, P. *et al.* Hydrodynamic trapping of molecules in lipid bilayers. *Proc Natl Acad Sci U S A* **109**, 10328-10333, doi:10.1073/pnas.1202858109 (2012).
154 Edelstein, A., Amodaj, N., Hoover, K., Vale, R. & Stuurman, N. Computer control of microscopes using Micromanager. *Curr Protoc Mol Biol,* **Chapter 14**, Unit14.20, doi:10.1002/0471142727.mb1420s92 (2010).
155 Weimann, L. *et al.* A quantitative comparison of single-dye tracking analysis tools using Monte Carlo simulations. *Plos One* **8**, 9, doi:10.1371/journal.pone.0064287 (2013).
156 Tosatto, L. *et al.* Single-molecule FRET studies on alpha-synuclein oligomerization of Parkinson's disease genetically related mutants. *Sci Rep* **5**, 16696, doi:10.1038/srep16696 (2015).
157 Khalaf, O. *et al.* The H50Q mutation enhances alpha-synuclein aggregation, secretion, and toxicity. *J Biol Chem* **289**, 21856-21876, doi:10.1074/jbc.M114.553297 (2014).
158 Murphy, R. R., Danezis, G., Horrocks, M. H., Jackson, S. E. & Klenerman, D. Bayesian inference of accurate population sizes and FRET efficiencies from single diffusing biomolecules. *Anal Chem* **86**, 8603-8612, doi:10.1021/ac501188r (2014).
159 Shammas, S. L. *et al.* A mechanistic model of tau amyloid aggregation based on direct observation of oligomers. *Nat Commun* **6**, 7025, doi:10.1038/ncomms8025 (2015).

160 Ding, H., Wong, P. T., Lee, E. L., Gafni, A. & Steel, D. G. Determination of the oligomer size of amyloidogenic protein beta-amyloid(1-40) by single-molecule spectroscopy. *Biophys J* **97**, 912-921, doi:10.1016/j.bpj.2009.05.035 (2009).
161 Kellie, J. F. *et al.* Quantitative measurement of intact alpha-synuclein proteoforms from post-mortem control and Parkinson's disease brain tissue by intact protein mass spectrometry. *Sci Rep* **4**, 5797, doi:10.1038/srep05797 (2014).
162 Mollenhauer, B. *et al.* Alpha-synuclein and tau concentrations in cerebrospinal fluid of patients presenting with parkinsonism: a cohort study. *Lancet Neurol* **10**, 230-240, doi:10.1016/S1474-4422(11)70014-X (2011).
163 Bellucci, A., Navarria, L., Zaltieri, M., Missale, C. & Spano, P. Alpha-synuclein synaptic pathology and its implications in the development of novel therapeutic approaches to cure Parkinson's disease. *Brain Res* **1432**, 95-113, doi:10.1016/j.brainres.2011.11.031 (2012).
164 George, S. & Brundin, P. Immunotherapy in Parkinson's disease: micromanaging alpha-synuclein aggregation. *J Parkinsons Dis* **5**, 413-424, doi:10.3233/JPD-150630 (2015).
165 Chothia, C., Gelfand, I. & Kister, A. Structural determinants in the sequences of immunoglobulin variable domain. *J Mol Biol* **278**, 457-479, doi:10.1006/jmbi.1998.1653 (1998).
166 Hamers-Casterman, C. *et al.* Naturally occurring antibodies devoid of light chains. *Nature* **363**, 446-448, doi:10.1038/363446a0 (1993).
167 Muyldermans, S. Single-domain camel antibodies: current status. *J Biotechnol* **74**, 277-302 (2001).
168 Pain, C., Dumont, J. & Dumoulin, M. Camelid single-domain antibody fragments: uses and prospects to investigate protein misfolding and aggregation, and to treat diseases associated with these phenomena. *Biochimie* **111**, 82-106, doi:10.1016/j.biochi.2015.01.012 (2015).
169 Kirchhofer, A. *et al.* Modulation of protein properties in living cells using nanobodies. *Nat Struct Mol Biol* **17**, 133-138, doi:10.1038/nsmb.1727 (2010).
170 Jones, D. R., Taylor, W. A., Bate, C., David, M. & Tayebi, M. A camelid anti-PrP antibody abrogates PrP replication in prion-permissive neuroblastoma cell lines. *PLoS One* **5**, e9804, doi:10.1371/journal.pone.0009804 (2010).
171 De Genst, E. J. *et al.* Structure and properties of a complex of alpha-synuclein and a single-domain camelid antibody. *J Mol Biol* **402**, 326-343, doi:10.1016/j.jmb.2010.07.001 (2010).
172 Guilliams, T. *et al.* Nanobodies raised against monomeric alpha-synuclein distinguish between fibrils at different maturation stages. *J Mol Biol* **425**, 2397-2411, doi:10.1016/j.jmb.2013.01.040 (2013).
173 El-Turk, F. *et al.* Structural effects of two camelid nanobodies directed to distinct C-terminal epitopes on alpha-synuclein. *Biochemistry*, doi:10.1021/acs.biochem.6b00149 (2016).
174 Mysling, S., Betzer, C., Jensen, P. H. & Jorgensen, T. J. Characterizing the dynamics of alpha-synuclein oligomers using hydrogen/deuterium exchange monitored by mass spectrometry. *Biochemistry* **52**, 9097-9103, doi:10.1021/bi4009193 (2013).
175 Reverberi, R. & Reverberi, L. Factors affecting the antigen-antibody reaction. *Blood Transfus* **5**, 227-240, doi:10.2450/2007.0047-07 (2007).
176 den Hartog Jager, W. A. Sphingomyelin in Lewy inclusion bodies in Parkinson's disease. *Archives of Neurology* **21**, 615-619, doi:10.1001/archneur.1969.00480180071006 (1969).
177 Gai, W. P. *et al.* In situ and in vitro study of colocalization and segregation of alpha-synuclein, ubiquitin, and lipids in Lewy bodies. *Experimental Neurology* **166**, 324-333, doi:10.1006/exnr.2000.7527 (2000).
178 Wenk, M. R. & De Camilli, P. Protein-lipid interactions and phosphoinositide metabolism in membrane traffic: insights from vesicle recycling in nerve terminals. *Proceedings of the National Academy of Sciences of the United States of America* **101**, 8262-8269, doi:10.1073/pnas.0401874101 (2004).
179 Rigoni, M. *et al.* Equivalent effects of snake PLA2 neurotoxins and lysophospholipid-fatty acid mixtures. *Science* **310**, 1678-1680, doi:10.1126/science.1120640 (2005).

180 Lang, T., Halemani, N. D. & Rammner, B. Interplay between lipids and the proteinaceous membrane fusion machinery. *Progress in Lipid Research* **47**, 461-469, doi:10.1016/j.plipres.2008.08.002 (2008).
181 Bader, M.-F. & Vitale, N. Phospholipase D in calcium-regulated exocytosis: lessons from chromaffin cells. *Biochimica Et Biophysica Acta-Molecular and Cell Biology of Lipids* **1791**, 936-941, doi:10.1016/j.bbalip.2009.02.016 (2009).
182 Sharon, R., Goldberg, M. S., Bar-Joseph, I., Shen, J. & Selkoe, D. J. Alpha-synuclein occurs in lipid-rich high molecular weight complexes, binds fatty acids and shows homology to the fatty acid binding proteins. *Society for Neuroscience Abstracts* **27**, 608 (2001).
183 Sharon, R. *et al.* The formation of highly soluble oligomers of alpha-synuclein is regulated by fatty acids and enhanced in Parkinson's disease. *Neuron* **37**, 583-595, doi:10.1016/s0896-6273(03)00024-2 (2003).
184 Kitajka, K. *et al.* The role of n-3 polyunsaturated fatty acids in brain: modulation of rat brain gene expression by dietary n-3 fatty acids. *Proceedings of the National Academy of Sciences of the United States of America* **99**, 2619-2624, doi:10.1073/pnas.042698699 (2002).
185 Kitajka, K. *et al.* Effects of dietary omega-3 polyunsaturated fatty acids on brain gene expression. *Proceedings of the National Academy of Sciences of the United States of America* **101**, 10931-10936, doi:10.1073/pnas.0402342101 (2004).
186 Yakunin, E. *et al.* Alpha-synuclein neuropathology is controlled by nuclear hormone receptors and enhanced by docosahexaenoic acid in a mouse model for Parkinson's disease. *Brain Pathology* **22**, 280-294, doi:10.1111/j.1750-3639.2011.00530.x (2012).
187 Sharon, R., Bar-Joseph, I. & Selkoe, D. J. Polyunsaturated fatty acid composition is altered in human brains with alpha-synucleinopathies and dopaminergic neurons expressing alpha-synuclein; implications on membrane fluidity. *Society for Neuroscience Abstract Viewer and Itinerary Planner* **2003**, Abstract No. 558.551 (2003).
188 Crawford, M. A. & Sinclair, A. J. Nutritional influences in the evolution of mammalian brain. In: lipids, malnutrition & the developing brain. *Ciba Foundation symposium*, 267-292 (1971).
189 Rossetto, O., Morbiato, L., Caccin, P., Rigoni, M. & Montecucco, C. Presynaptic enzymatic neurotoxins. *Journal of Neurochemistry* **97**, 1534-1545, doi:10.1111/j.1471-4159.2006.03965.x (2006).
190 Lewis, R. A. & Austen, K. F. Mediation of local homeostasis and inflammation by leukotrienes and other mast cell-dependent compounds. *Nature* **293**, 103-108, doi:10.1038/293103a0 (1981).
191 Crews, F. T. *et al.* IgE-mediated histamine release in rat basophilic leukemia - cell receptor activation, phospholipid methylation, Ca2+ flux, and release of arachidonic acid. *Archives of Biochemistry and Biophysics* **212**, 561-571, doi:10.1016/0003-9861(81)90399-4 (1981).
192 Takeuchi, Y., Morii, H., Tamura, M., Hayaishi, O. & Watanabe, Y. A possible mechanism of mitochondrial dysfunction during cerebral ischemia: inhibition of mitochondrial respiration activity by arachidonic acid. *Arch Biochem Biophys* **289**, 33-38 (1991).
193 Lipton, P. Ischemic cell death in brain neurons. *Physiol Rev* **79**, 1431-1568 (1999).
194 Brash, A. R. Arachidonic acid as a bioactive molecule. *Journal of Clinical Investigation* **107**, 1339-1345, doi:10.1172/jci13210 (2001).
195 Fang, K. M., Chang, W. L., Wang, S. M., Su, M. J. & Wu, M. L. Arachidonic acid induces both Na+ and Ca2+ entry resulting in apoptosis. *J Neurochem* **104**, 1177-1189, doi:10.1111/j.1471-4159.2007.05022.x (2008).
196 Meves, H. Arachidonic acid and ion channels: an update. *Br J Pharmacol* **155**, 4-16, doi:10.1038/bjp.2008.216 (2008).
197 Darios, F. & Davletov, B. Omega-3 and omega-6 fatty acids stimulate cell membrane expansion by acting on syntaxin 3. *Nature* **440**, 813-817, doi:10.1038/nature04598 (2006).
198 Connell, E. *et al.* Mechanism of arachidonic acid action on syntaxin-Munc18. *EMBO Rep* **8**, 414-419, doi:10.1038/sj.embor.7400935 (2007).
199 Lynch, M. A., Clements, M. P., Voss, K. L., Bramham, C. R. & Bliss, T. V. Is arachidonic acid a retrograde messenger in long-term potentiation? *Biochem Soc Trans* **19**, 391-396 (1991).

200 O'Dell, T. J., Hawkins, R. D., Kandel, E. R. & Arancio, O. Tests of the roles of two diffusible substances in long-term potentiation: evidence for nitric oxide as a possible early retrograde messenger. *Proc Natl Acad Sci U S A* **88**, 11285-11289 (1991).
201 Carta, M. *et al.* Membrane lipids tune synaptic transmission by direct modulation of presynaptic potassium channels. *Neuron* **81**, 787-799, doi:10.1016/j.neuron.2013.12.028 (2014).
202 Perrin, R. J., Woods, W. S., Clayton, D. F. & George, J. M. Exposure to long chain polyunsaturated fatty acids triggers rapid multimerization of synucleins. *Journal of Biological Chemistry* **276**, 41958-41962, doi:10.1074/jbc.M105022200 (2001).
203 Broersen, K., van den Brink, D., Fraser, G., Goedert, M. & Davletov, B. Alpha-synuclein adopts an alpha-helical conformation in the presence of polyunsaturated fatty acids to hinder micelle formation. *Biochemistry* **45**, 15610-15616, doi:10.1021/bi061743l (2006).
204 Serth, J., Lautwein, A., Frech, M., Wittinghofer, A. & Pingoud, A. The inhibition of the GTPase activating protein-Ha-ras interaction by acidic lipids is due to physical association of the C-terminal domain of the GTPase activating protein with micellar structures. *EMBO J* **10**, 1325-1330 (1991).
205 Paleologou, K. E., Irvine, G. B. & El-Agnaf, O. M. Alpha-synuclein aggregation in neurodegenerative diseases and its inhibition as a potential therapeutic strategy. *Biochem Soc Trans* **33**, 1106-1110, doi:10.1042/BST20051106 (2005).
206 Guerrero, C., Tagwerker, C., Kaiser, P. & Huang, L. An integrated mass spectrometry-based proteomic approach: quantitative analysis of tandem affinity-purified in vivo cross-linked protein complexes (QTAX) to decipher the 26 S proteasome-interacting network. *Mol Cell Proteomics* **5**, 366-378, doi:10.1074/mcp.M500303-MCP200 (2006).
207 Wang, X. *et al.* Mass spectrometric characterization of the affinity-purified human 26S proteasome complex. *Biochemistry* **46**, 3553-3565, doi:10.1021/bi061994u (2007).
208 De Franceschi, G. *et al.* Structural and morphological characterization of aggregated species of alpha-synuclein induced by docosahexaenoic acid. *J Biol Chem* **286**, 22262-22274, doi:10.1074/jbc.M110.202937 (2011).
209 Bennett, M. C. *et al.* Degradation of alpha-synuclein by proteasome. *J Biol Chem* **274**, 33855-33858 (1999).
210 Snyder, H. *et al.* Aggregated and monomeric alpha-synuclein bind to the S6' proteasomal protein and inhibit proteasomal function. *J Biol Chem* **278**, 11753-11759, doi:10.1074/jbc.M208641200 (2003).
211 Hellstrand, E., Nowacka, A., Topgaard, D., Linse, S. & Sparr, E. Membrane lipid co-aggregation with alpha-synuclein fibrils. *PLoS One* **8**, e77235, doi:10.1371/journal.pone.0077235 (2013).
212 Westphal, C. H. & Chandra, S. S. Monomeric synucleins generate membrane curvature. *J Biol Chem* **288**, 1829-1840, doi:10.1074/jbc.M112.418871 (2013).
213 Masuda, M. *et al.* Small molecule inhibitors of alpha-synuclein filament assembly. *Biochemistry* **45**, 6085-6094, doi:10.1021/bi0600749 (2006).
214 Ehrnhoefer, D. E. *et al.* EGCG redirects amyloidogenic polypeptides into unstructured, off-pathway oligomers. *Nat Struct Mol Biol* **15**, 558-566, doi:10.1038/nsmb.1437 (2008).
215 Dettmer, U., Newman, A. J., Luth, E. S., Bartels, T. & Selkoe, D. In vivo cross-linking reveals principally oligomeric forms of alpha-synuclein and beta-synuclein in neurons and non-neural cells. *J Biol Chem* **288**, 6371-6385, doi:10.1074/jbc.M112.403311 (2013).
216 Gurry, T. *et al.* The dynamic structure of alpha-synuclein multimers. *J Am Chem Soc* **135**, 3865-3872, doi:10.1021/ja310518p (2013).
217 Dettmer, U. *et al.* Parkinson-causing alpha-synuclein missense mutations shift native tetramers to monomers as a mechanism for disease initiation. *Nat Commun* **6**, 7314, doi:10.1038/ncomms8314 (2015).
218 Bousquet, M. *et al.* Beneficial effects of dietary omega-3 polyunsaturated fatty acid on toxin-induced neuronal degeneration in an animal model of Parkinson's disease. *FASEB J* **22**, 1213-1225, doi:10.1096/fj.07-9677com (2008).

219 Bousquet, M., Calon, F. & Cicchetti, F. Impact of ω-3 fatty acids in Parkinson's disease. *Ageing Res Rev* **10**, 453-463, doi:10.1016/j.arr.2011.03.001 (2011).
220 Luth, E. S., Bartels, T., Dettmer, U., Kim, N. C. & Selkoe, D. J. Purification of alpha-synuclein from human brain reveals an instability of endogenous multimers as the protein approaches purity. *Biochemistry* **54**, 279-292, doi:10.1021/bi501188a (2015).
221 Kang, J. *et al.* The precursor of Alzheimer's disease amyloid A4 protein resembles a cell-surface receptor. *Nature* **325**, 733-736, doi:10.1038/325733a0 (1987).
222 Sisodia, S. S. Beta-amyloid precursor protein cleavage by a membrane-bound protease. *Proceedings of the National Academy of Sciences of the United States of America* **89**, 6075-6079 (1992).
223 Cole, S. L. & Vassar, R. The Alzheimer's disease beta-secretase enzyme, BACE1. *Mol Neurodegener* **2**, 22, doi:10.1186/1750-1326-2-22 (2007).
224 Hardy, J. & Allsop, D. Amyloid deposition as the central event in the aetiology of Alzheimer's disease. *Trends Pharmacol Sci* **12**, 383-388 (1991).
225 Atwood, C. S. *et al.* Amyloid-beta: a chameleon walking in two worlds: a review of the trophic and toxic properties of amyloid-beta. *Brain Res Brain Res Rev* **43**, 1-16 (2003).
226 Kumar, D. K. *et al.* Amyloid-beta peptide protects against microbial infection in mouse and worm models of Alzheimer's disease. *Sci Transl Med* **8**, 340ra372, doi:10.1126/scitranslmed.aaf1059 (2016).
227 Haass, C. Take five-BACE and the gamma-secretase quartet conduct Alzheimer's amyloid beta-peptide generation. *EMBO J* **23**, 483-488, doi:10.1038/sj.emboj.7600061 (2004).
228 Meisl, G. *et al.* Differences in nucleation behavior underlie the contrasting aggregation kinetics of the Aβ40 and Aβ42 peptides. *Proceedings of the National Academy of Sciences of the United States of America* **111**, 9384-9389, doi:10.1073/pnas.1401564111 (2014).
229 Jarrett, J. T., Berger, E. P. & Lansbury, P. T. The carboxy terminus of the beta-amyloid protein is critical for the seeding of amyloid formation: implications for the pathogenesis of Alzheimer's disease. *Biochemistry* **32**, 4693-4697 (1993).
230 Gravina, S. A. *et al.* Amyloid-beta protein in Alzheimer's disease brain. Biochemical and immunocytochemical analysis with antibodies specific for forms ending at Aβ40 or Aβ42(43). *J Biol Chem* **270**, 7013-7016 (1995).
231 Iwatsubo, T. *et al.* Visualization of Aβ42(43) and Aβ40 in senile plaques with end-specific amyloid-beta monoclonals: evidence that an initially deposited species is Aβ42(43). *Neuron* **13**, 45-53 (1994).
232 Scheuner, D. *et al.* Secreted amyloid-beta - protein similar to that in the senile plaques of Alzheimer's disease is increased in vivo by the presenilin 1 and 2 and APP mutations linked to familial Alzheimer's disease. *Nat Med* **2**, 864-870 (1996).
233 Dahlgren, K. N. *et al.* Oligomeric and fibrillar species of amyloid-beta peptides differentially affect neuronal viability. *J Biol Chem* **277**, 32046-32053, doi:10.1074/jbc.M201750200 (2002).
234 Pauwels, K. *et al.* Structural basis for increased toxicity of pathological A-beta(42):A-beta(40) ratios in Alzheimer disease. *Journal of Biological Chemistry* **287**, 5650-5660, doi:10.1074/jbc.M111.264473 (2012).
235 Kuperstein, I. *et al.* Neurotoxicity of Alzheimer's disease amyloid-beta peptides is induced by small changes in the Aβ42 to Aβ40 ratio. *Embo Journal* **29**, 3408-3420, doi:10.1038/emboj.2010.211 (2010).
236 Duff, K. *et al.* Increased amyloid-beta 42(43) in brains of mice expressing mutant presenilin 1. *Nature* **383**, 710-713, doi:10.1038/383710a0 (1996).
237 Citron, M. *et al.* Mutant presenilins of Alzheimer's disease increase production of 42-residue amyloid beta-protein in both transfected cells and transgenic mice. *Nature Medicine* **3**, 67-72, doi:10.1038/nm0197-67 (1997).
238 Hellstrom-Lindahl, E., Viitanen, M. & Marutle, A. Comparison of amyloid-beta levels in the brain of familial and sporadic Alzheimer's disease. *Neurochemistry International* **55**, 243-252, doi:10.1016/j.neuint.2009.03.007 (2009).

239 Haass, C. & Selkoe, D. J. Soluble protein oligomers in neurodegeneration: lessons from the Alzheimer's amyloid-beta peptide. *Nat Rev Mol Cell Biol* **8**, 101-112, doi:10.1038/nrm2101 (2007).
240 Garcia, G. A., Cohen, S. I. A., Dobson, C. M. & Knowles, T. P. J. Nucleation-conversion-polymerization reactions of biological macromolecules with prenucleation clusters. *Physical Review E* **89**, 6, doi:10.1103/PhysRevE.89.032712 (2014).
241 Bitan, G., Fradinger, E. A., Spring, S. M. & Teplow, D. B. Neurotoxic protein oligomers-what you see is not always what you get. *Amyloid* **12**, 88-95, doi:10.1080/13506120500106958 (2005).
242 Frost, D., Gorman, P. M., Yip, C. M. & Chakrabartty, A. Co-incorporation of Aβ40 and Aβ42 to form mixed pre-fibrillar aggregates. *Eur J Biochem* **270**, 654-663 (2003).
243 Hasegawa, K., Yamaguchi, I., Omata, S., Gejyo, F. & Naiki, H. Interaction between Aβ(1-42) and Aβ(1-40) in Alzheimer's beta-amyloid fibril formation in vitro. *Biochemistry* **38**, 15514-15521, doi:10.1021/bi991161m (1999).
244 Kim, J. *et al.* Aβ40 inhibits amyloid deposition in vivo. *Journal of Neuroscience* **27**, 627-633, doi:10.1523/jneurosci.4849-06.2007 (2007).
245 Murray, M. M. *et al.* Amyloid-beta protein: Aβ40 inhibits Aβ42 oligomerization. *Journal of the American Chemical Society* **131**, 6316-+, doi:10.1021/ja8092604 (2009).
246 Yoshiike, Y., Chui, D. H., Akagi, T., Tanaka, N. & Takashima, A. Specific compositions of amyloid-beta peptides as the determinant of toxic beta-aggregation. *Journal of Biological Chemistry* **278**, 23648-23655, doi:10.1074/jbc.M212785200 (2003).
247 Johnson, R. D. *et al.* Single-molecule imaging reveals Aβ42:Aβ40 ratio-dependent oligomer growth on neuronal processes. *Biophys J* **104**, 894-903, doi:10.1016/j.bpj.2012.12.051 (2013).
248 Cukalevski, R. *et al.* The Aβ40 and Aβ42 peptides self-assemble into separate homomolecular fibrils in binary mixtures but cross-react during primary nucleation. *Chem. Sci.* **6**, 4215-4233 (2015).
249 Mehta, P. D. *et al.* Plasma and cerebrospinal fluid levels of amyloid-beta proteins 1-40 and 1-42 in Alzheimer disease. *Arch Neurol* **57**, 100-105 (2000).
250 Brender, J. R. *et al.* Probing the sources of the apparent irreproducibility of amyloid formation: drastic changes in kinetics and a switch in mechanism due to micelle-like oligomer formation at critical concentrations of IAPP. *J Phys Chem B* **119**, 2886-2896, doi:10.1021/jp511758w (2015).
251 Ladiwala, A. R. *et al.* Conformational differences between two amyloid-beta oligomers of similar size and dissimilar toxicity. *J Biol Chem* **287**, 24765-24773, doi:10.1074/jbc.M111.329763 (2012).
252 Sabaté, R. & Estelrich, J. Evidence of the existence of micelles in the fibrillogenesis of beta-amyloid peptide. *J Phys Chem B* **109**, 11027-11032, doi:10.1021/jp050716m (2005).
253 Soreghan, B., Kosmoski, J. & Glabe, C. Surfactant properties of Alzheimer's Aβ peptides and the mechanism of amyloid aggregation. *J Biol Chem* **269**, 28551-28554 (1994).
254 Hu, Y., Su, B., Zheng, H. & Kim, J. R. A peptide probe for detection of various beta-amyloid oligomers. *Mol Biosyst* **8**, 2741-2752, doi:10.1039/c2mb25148e (2012).
255 Galpern, W. R. & Lang, A. E. Interface between tauopathies and synucleinopathies: a tale of two proteins. *Ann Neurol* **59**, 449-458, doi:10.1002/ana.20819 (2006).
256 Hamilton, R. L. Lewy bodies in Alzheimer's disease: a neuropathological review of 145 cases using alpha-synuclein immunohistochemistry. *Brain Pathol* **10**, 378-384 (2000).
257 Tsigelny, I. F. *et al.* Mechanisms of hybrid oligomer formation in the pathogenesis of combined Alzheimer's and Parkinson's diseases. *PLoS One* **3**, e3135, doi:10.1371/journal.pone.0003135 (2008).
258 Korff, A. *et al.* Alpha-Synuclein in cerebrospinal fluid of Alzheimer's disease and mild cognitive impairment. *J Alzheimers Dis* **36**, 679-688, doi:10.3233/JAD-130458 (2013).
259 Jellinger, K. A. & Attems, J. Prevalence and impact of vascular and Alzheimer pathologies in Lewy body disease. *Acta Neuropathol* **115**, 427-436, doi:10.1007/s00401-008-0347-5 (2008).

260 Toledo, J. B. *et al.* Pathological alpha-synuclein distribution in subjects with coincident Alzheimer's and Lewy body pathology. *Acta Neuropathol* **131**, 393-409, doi:10.1007/s00401-015-1526-9 (2016).
261 Bachhuber, T. *et al.* Inhibition of amyloid-beta plaque formation by alpha-synuclein. *Nat Med* **21**, 802-807, doi:10.1038/nm.3885 (2015).
262 Atsmon-Raz, Y. & Miller, Y. Non-Amyloid-beta component of human alpha-synuclein oligomers induces formation of new Aβ oligomers: insight into the mechanisms that link Parkinson's and Alzheimer's diseases. *ACS Chem Neurosci* **7**, 46-55, doi:10.1021/acschemneuro.5b00204 (2016).
263 Yoshimoto, M. *et al.* NACP, the precursor protein of the non-amyloid beta/A4 protein component of Alzheimer disease amyloid, binds amyloid-beta and stimulates amyloid-beta aggregation. *Proceedings of the National Academy of Sciences of the United States of America* **92**, 9141-9145 (1995).
264 Jensen, P. H. *et al.* Binding of amyloid-beta to alpha- and beta-synucleins: identification of segments in alpha-synuclein/NAC precursor that bind amyloid-beta and NAC. *Biochem J* **323 (Pt 2)**, 539-546 (1997).
265 Mandal, P. K., Pettegrew, J. W., Masliah, E., Hamilton, R. L. & Mandal, R. Interaction between amyloid-beta peptide and alpha-synuclein: molecular mechanisms in overlapping pathology of Alzheimer's and Parkinson's in dementia with Lewy body disease. *Neurochem Res* **31**, 1153-1162, doi:10.1007/s11064-006-9140-9 (2006).
266 Ono, K., Takahashi, R., Ikeda, T. & Yamada, M. Cross-seeding effects of amyloid-beta protein and alpha-synuclein. *J Neurochem* **122**, 883-890, doi:10.1111/j.1471-4159.2012.07847.x (2012).
267 Planchard, M. S., Exley, S. E., Morgan, S. E. & Rangachari, V. Dopamine-induced alpha-synuclein oligomers show self- and cross-propagation properties. *Protein Sci*, doi:10.1002/pro.2521 (2014).
268 Shaykhalishahi, H. *et al.* Contact between the β1 and β2 Segments of alpha-synuclein that inhibits amyloid formation. *Angew Chem Int Ed Engl* **54**, 8837-8840, doi:10.1002/anie.201503018 (2015).
269 Jose, J. C., Chatterjee, P. & Sengupta, N. Cross dimerization of amyloid-beta and alpha-synuclein proteins in aqueous environment: a molecular dynamics simulations study. *PLoS One* **9**, e106883, doi:10.1371/journal.pone.0106883 (2014).
270 De Ricco, R. *et al.* Copper(I/II), alpha/beta-synuclein and amyloid-beta: menage à trois? *Chembiochem* **16**, 2319-2328, doi:10.1002/cbic.201500425 (2015).
271 Dehmelt, L. & Halpain, S. The MAP2/tau family of microtubule-associated proteins. *Genome Biol* **6**, 204, doi:10.1186/gb-2004-6-1-204 (2005).
272 Billingsley, M. L. & Kincaid, R. L. Regulated phosphorylation and dephosphorylation of tau protein: effects on microtubule interaction, intracellular trafficking and neurodegeneration. *Biochem J* **323 (Pt 3)**, 577-591 (1997).
273 Himmler, A., Drechsel, D., Kirschner, M. W. & Martin, D. W. Tau consists of a set of proteins with repeated C-terminal microtubule-binding domains and variable N-terminal domains. *Mol Cell Biol* **9**, 1381-1388 (1989).
274 Mandelkow, E., von Bergen, M., Biernat, J. & Mandelkow, E. M. Structural principles of tau and the paired helical filaments of Alzheimer's disease. *Brain Pathol* **17**, 83-90, doi:10.1111/j.1750-3639.2007.00053.x (2007).
275 Barghorn, S., Davies, P. & Mandelkow, E. Tau paired helical filaments from Alzheimer's disease brain and assembled in vitro are based on beta-structure in the core domain. *Biochemistry* **43**, 1694-1703, doi:10.1021/bi0357006 (2004).
276 Barghorn, S., Biernat, J. & Mandelkow, E. Purification of recombinant tau protein and preparation of Alzheimer-paired helical filaments in vitro. *Methods Mol Biol* **299**, 35-51 (2005).
277 Jeganathan, S., von Bergen, M., Mandelkow, E. M. & Mandelkow, E. The natively unfolded character of tau and its aggregation to Alzheimer-like paired helical filaments. *Biochemistry* **47**, 10526-10539, doi:10.1021/bi800783d (2008).

278 Mandelkow, E. M. & Mandelkow, E. Biochemistry and cell biology of tau protein in neurofibrillary degeneration. *Cold Spring Harb Perspect Med* **2**, a006247, doi:10.1101/cshperspect.a006247 (2012).
279 Moussaud, S. *et al.* Alpha-synuclein and tau: teammates in neurodegeneration? *Mol Neurodegener* **9**, 43, doi:10.1186/1750-1326-9-43 (2014).
280 Colom-Cadena, M. *et al.* Confluence of alpha-synuclein, tau, and beta-amyloid pathologies in dementia with Lewy bodies. *J Neuropathol Exp Neurol* **72**, 1203-1212, doi:10.1097/NEN.0000000000000018 (2013).
281 Leverenz, J. B. *et al.* Proteomic identification of novel proteins in cortical lewy bodies. *Brain Pathol* **17**, 139-145, doi:10.1111/j.1750-3639.2007.00048.x (2007).
282 Arima, K. *et al.* NACP/alpha-synuclein and tau constitute two distinctive subsets of filaments in the same neuronal inclusions in brains from a family of parkinsonism and dementia with Lewy bodies: double-immunolabeling fluorescence and electron microscopic studies. *Acta Neuropathol* **100**, 115-121 (2000).
283 Sengupta, U. *et al.* Pathological interface between oligomeric alpha-synuclein and tau in synucleinopathies. *Biol Psychiatry* **78**, 672-683, doi:10.1016/j.biopsych.2014.12.019 (2015).
284 Guo, J. L. *et al.* Distinct alpha-synuclein strains differentially promote tau inclusions in neurons. *Cell* **154**, 103-117, doi:10.1016/j.cell.2013.05.057 (2013).
285 Jensen, P. H. *et al.* Alpha-synuclein binds to tau and stimulates the protein kinase A-catalyzed tau phosphorylation of serine residues 262 and 356. *J Biol Chem* **274**, 25481-25489 (1999).
286 Esposito, A., Dohm, C. P., Kermer, P., Bähr, M. & Wouters, F. S. Alpha-synuclein and its disease-related mutants interact differentially with the microtubule protein tau and associate with the actin cytoskeleton. *Neurobiol Dis* **26**, 521-531, doi:10.1016/j.nbd.2007.01.014 (2007).
287 Badiola, N. *et al.* Tau enhances alpha-synuclein aggregation and toxicity in cellular models of synucleinopathy. *PLoS One* **6**, e26609, doi:10.1371/journal.pone.0026609 (2011).
288 Giasson, B. I. *et al.* Initiation and synergistic fibrillization of tau and alpha-synuclein. *Science* **300**, 636-640, doi:10.1126/science.1082324 (2003).
289 Qureshi, H. Y. & Paudel, H. K. Parkinsonian neurotoxin 1-methyl-4-phenyl-1,2,3,6-tetrahydropyridine (MPTP) and alpha-synuclein mutations promote tau protein phosphorylation at Ser262 and destabilize microtubule cytoskeleton in vitro. *J Biol Chem* **286**, 5055-5068, doi:10.1074/jbc.M110.178905 (2011).
290 Benussi, L. *et al.* Interaction between tau and alpha-synuclein proteins is impaired in the presence of P301L tau mutation. *Exp Cell Res* **308**, 78-84, doi:10.1016/j.yexcr.2005.04.021 (2005).
291 Nübling, G. *et al.* Synergistic influence of phosphorylation and metal ions on tau oligomer formation and coaggregation with alpha-synuclein at the single-molecule level. *Mol Neurodegener* **7**, 35, doi:10.1186/1750-1326-7-35 (2012).
292 Guo, J. P., Arai, T., Miklossy, J. & McGeer, P. L. Amyloid-beta and tau form soluble complexes that may promote self aggregation of both into the insoluble forms observed in Alzheimer's disease. *Proceedings of the National Academy of Sciences of the United States of America* **103**, 1953-1958, doi:10.1073/pnas.0509386103 (2006).
293 Vasconcelos, B. *et al.* Heterotypic seeding of tau fibrillization by pre-aggregated amyloid-beta provides potent seeds for prion-like seeding and propagation of tau-pathology in vivo. *Acta Neuropathol* **131**, 549-569, doi:10.1007/s00401-015-1525-x (2016).
294 Teplow, D. B. Preparation of amyloid-beta protein for structural and functional studies. *Methods Enzymol* **413**, 20-33, doi:10.1016/S0076-6879(06)13002-5 (2006).
295 Horrocks, M. H. *et al.* Single-molecule imaging of individual amyloid protein aggregates in human biofluids. *ACS Chem Neurosci*, doi:10.1021/acschemneuro.5b00324 (2016).
296 Brännström, K. *et al.* The N-terminal region of amyloid-beta controls the aggregation rate and fibril stability at low pH through a gain of function mechanism. *J Am Chem Soc* **136**, 10956-10964, doi:10.1021/ja503535m (2014).

297 Hellstrand, E., Boland, B., Walsh, D. M. & Linse, S. Amyloid-beta protein aggregation produces highly reproducible kinetic data and occurs by a two-phase process. *ACS Chem Neurosci* **1**, 13-18, doi:10.1021/cn900015v (2010).
298 O'Nuallain, B., Shivaprasad, S., Kheterpal, I. & Wetzel, R. Thermodynamics of Aβ40 amyloid fibril elongation. *Biochemistry* **44**, 12709-12718, doi:10.1021/bi050927h (2005).
299 Williams, A. D., Shivaprasad, S. & Wetzel, R. Alanine scanning mutagenesis of Aβ40 amyloid fibril stability. *J Mol Biol* **357**, 1283-1294, doi:10.1016/j.jmb.2006.01.041 (2006).
300 Sánchez, L. *et al.* Aβ40 and Aβ42 amyloid fibrils exhibit distinct molecular recycling properties. *J Am Chem Soc* **133**, 6505-6508, doi:10.1021/ja1117123 (2011).
301 Brorsson, A. C. *et al.* Intrinsic determinants of neurotoxic aggregate formation by the amyloid-beta peptide. *Biophys J* **98**, 1677-1684, doi:10.1016/j.bpj.2009.12.4320 (2010).
302 Iljina, M. *et al.* Quantitative analysis of co-oligomer formation by amyloid-beta peptide isoforms. *Sci Rep* **6**, 28658, doi:10.1038/srep28658 (2016).